INFORMATION TO USERS

This manuscript has been reproduced from the microfilm master. UMI films the text directly from the original or copy submitted. Thus, some thesis and dissertation copies are in typewriter face, while others may be from any type of computer printer.

The quality of this reproduction is dependent upon the quality of the copy submitted. Broken or indistinct print, colored or poor quality illustrations and photographs, print bleedthrough, substandard margins, and improper alignment can adversely affect reproduction.

In the unlikely event that the author did not send UMI a complete manuscript and there are missing pages, these will be noted. Also, if unauthorized copyright material had to be removed, a note will indicate the deletion.

Oversize materials (e.g., maps, drawings, charts) are reproduced by sectioning the original, beginning at the upper left-hand corner and continuing from left to right in equal sections with small overlaps. Each original is also photographed in one exposure and is included in reduced form at the back of the book.

Photographs included in the original manuscript have been reproduced xerographically in this copy. Higher quality 6" x 9" black and white photographic prints are available for any photographs or illustrations appearing in this copy for an additional charge. Contact UMI directly to order.

U·M·I

University Microfilms International
A Bell & Howell Information Company
300 North Zeeb Road, Ann Arbor, MI 48106-1346 USA
313/761-4700 800/521-0600

Order Number 9220702

Application of numerical techniques to faulting and flexure of the lithosphere

Wallace, Michelle Hall, Ph.D.

The University of Arizona, 1992

U·M·I
300 N. Zeeb Rd.
Ann Arbor, MI 48106

APPLICATION OF NUMERICAL TECHNIQUES TO FAULTING AND FLEXURE OF THE LITHOSPHERE

by

Michelle Hall Wallace

A Dissertation Submitted to the Faculty of the

DEPARTMENT OF GEOSCIENCES

In Partial Fulfillment of the Requirements
For the Degree of

DOCTOR OF PHILOSOPHY

In the Graduate College

THE UNIVERSITY OF ARIZONA

1992

THE UNIVERSITY OF ARIZONA
GRADUATE COLLEGE

As members of the Final Examination Committee, we certify that we have read the dissertation prepared by Michelle Hall Wallace

entitled Application of Numerical Techniques to Faulting and Flexure of the Lithosphere

and recommend that it be accepted as fulfilling the dissertation requirement for the Degree of Doctor of Philosophy

Clement G. Chase	12/19/91 Date
H. Jay Melosh	12/19/91 Date
Roy A. Johnson	12/19/91 Date
Peter J. Coney	12/19/91 Date
Robert F. Butler	12/19/91 Date

Final approval and acceptance of this dissertation is contingent upon the candidate's submission of the final copy of the dissertation to the Graduate College.

I hereby certify that I have read this dissertation prepared under my direction and recommend that it be accepted as fulfilling the dissertation requirement.

Dissertation Director
Clement G. Chase

10 Jan '92
Date

STATEMENT BY AUTHOR

This dissertation has been submitted in partial fulfillment of requirements for an advanced degree at The University of Arizona and is deposited in the University Library to be made available to borrowers under rules of the Library.

Brief quotations from this dissertation are allowable without special permission, provided that accurate acknowledgement of source is made. Requests for permission for extended quotation from or reproduction of this manuscript in whole or in part may be granted by the head of the major department or the Dean of the Graduate College when in his or her judgement the proposed use of the material is in the interests of scholarship. In all other instances, however, permission must be obtained from the author.

SIGNED: Michelle Lee Wallace

ACKNOWLEDGMENTS

The last several years of study have been improved by the presence of many wonderful people in my life, the most important being my son David and my husband, Terry. Without their encouragement and support I would not have endured so well. Eleanour Snow and Susan Beck have also been invaluable for comradeship and encouragement. Charles Williams played an important role in the initial stages of my understanding of finite elements and continues to be a source of help and ideas. A special thank you goes to Steve Sorenson, a man with monumental patience in spite of my blunders. I greatly appreciate the education I received from my co-authors John Kemeny, Jay Melosh and Terry Wallace. Jay Melosh was particularly ingenious in presenting a human experience of buckling under stress; thankfully, the human spirit is extremely elastic. Bob Butler and Peter Coney stand out when I reminisce about the last few years; both are wonderful listeners and great teachers. Roy Johnson and Clem Chase have also provided help with ideas and suggestions for improving this work.

I would like to dedicate this work to David and Terry. You two are the best thing that ever happened to me.

TABLE OF CONTENTS

Page

LIST OF ILLUSTRATIONS

Page

Page

LIST OF TABLES

Table **Page**

ABSTRACT

This research investigates problems of faulting and flexure of the lithosphere using the finite element technique. I examined two aspects of faulting, the nucleation and growth of dip slip faults in a stable craton in Chapter 2, and the rupture of the Loma Prieta earthquake in Chapter 3. Linear elastic fracture mechanics and the shear fracture energy criteria are used in conjunction with the finite element method to evaluate the stability of fault rupture. I investigated fault nucleation and growth under conditions of variable dip and shear fracture energy. Strain required for fault growth varied with respect to shear fracture energy gradient and rupture direction but not with dip. Rupture upward required more than twice the initial strain to cause fault growth, as compared to rupture downward, and would result in very large earthquakes. Rupture downward in models associated with the higher G_C gradient resulted in stable growth of the fault. I suggest that fault nucleation and growth is a stable process which would preferentially occur by rupturing downward under stable conditions.

In Chapter 3, I model the rupture of the Loma Prieta Fault, a moderately dipping reverse fault which is subparallel to the San Andreas Fault. Rupture initiated at 18 km and propagated updip in an oblique slip motion to 8-5 km depth. A similar technique as outlined above is used to investigate controls on the rupture propagation and the genetic relationship of the Loma Prieta and San Andreas faults. Low stress in the upper crust caused by a low strength material or the presence of other faults is responsible for stopping rupture. An evaluation of the stress at the intersection of the two faults indicates that the Loma Prieta Fault in the upper crust is still closer to the point of failure than the San Andreas Fault. Thus, rupture of the Loma Prieta did not significantly increase the seismic hazard of the San Andreas in that region.

In Chapter 4, I analyze the problem of buckling a faulted elastic plate. I studied the effect of changes in fault depth, spacing and dip on the buckling stress, wavelength and effective Young's modulus. Modeling results show that as the fault depth increases both the buckling stress and wavelength decrease. Similarly, the effective Young's modulus is a decreasing function of depth. As fault spacing was increased, the effect of the faults on the buckling stress and wavelength was minimized. Fault dip appears to have no significant effect on buckling response. The buckling response of a thick, faulted lithosphere is not equivalent to that of a thinner elastic plate. Faults lower the stress necessary for buckling, shorten the buckling wavelength and result in a lower effective Young's modulus.

CHAPTER 1

INTRODUCTION

Two of the most important dynamic processes for crustal deformation are faulting and flexure. Faulting at all scales is ubiquitous throughout the lithosphere. On a microscopic scale, faulting accounts for shortening in rock fabric; on a crustal scale, faults such as the San Andreas accommodate hundreds of kilometers of displacement over time lengths of millions of years [Hill and Dibblee, 1953; Atwater, 1970; Butler et al., 1989]. At an intermediate scale, differential topography is often related to vertical slip on faults.

Flexure, the folding and bending of the lithospheric shell, accommodates both vertical and horizontal loads at all scales as well. Flexure is an important process in many tectonic environments including development of deep sedimentary basins [Jordan, 1983; Lambeck, 1983; Cloeting et al., 1985], uplift of mountain ranges [Coney, 1969; Zandt and Owens, 1980; Hall and Chase, 1989] and in the deformation of the oceanic lithosphere [Walcott, 1970; Melosh, 1978; McNutt and Menard, 1982; McAdoo and Sandwell, 1985]. Thermal and temporal tectonic histories can be constrained with flexural studies. The flexural rebound resulting from unloading of ice sheets from the craton provides information for studies of mantle rheology; the volcanic pile associated with Hawaii generates a flexural response with a measurable amplitude and wavelength which provides constraints on flexural rigidity [Walcott, 1970; Turcotte and Schubert, 1982]. Buckling, the catastrophic failure of an elastic plate under horizontal compression, is an important end member of the flexural process. In the Central Indian Ocean, long wavelength sinusoidal topography has been attributed to anelastic buckling of the oceanic lithosphere under horizontal compression [McAdoo and Sandwell, 1985].

A substantial body of literature is devoted to modeling faulting and flexure to explain various geologic observations. The methodology of this modeling varies from first order analytical approximations to finite element modeling with boundary conditions imposed by the physics of the flexural and faulting problem. Vening Meinesz [1950] first modeled faulting and subsequent flexural uplift associated with half graben development at rift margins. Zandt and Owens [1980] applied a similar analysis to the Wasatch Fault, Utah. Comer [1983] developed the full analytical solution for flexure of a thick plate and numerous investigators have used the thin-plate approximation for flexure of plates [Chase and Wallace, 1986; Angevine and Flanagan, 1988; Buck, 1988; Hall and Chase, 1989]. More sophisticated boundary conditions and material properties require the use of numerical techniques such as the finite element method.

In this dissertation, I have adapted analytical solutions for flexure and faulting to finite element analysis to study a number of interesting problems of crustal scale deformation. Chapter 2 is a study of the nucleation and growth of dip-slip faults in a stable craton. A fault is modeled as a Mode II crack propagating in an elastic body. In Chapter 3, I applied a similar technique to study the rupture of the October 19, 1989 Loma Prieta earthquake. Rupture of the Loma Prieta Fault is modeled as a combination of Mode II and Mode III crack motion propagating in a tectonically active region. Buckling of a faulted lithosphere is the subject of Chapter 4; the finite element method is applied to solve a problem for which analytical solutions do not exist.

Crustal Scale Faulting

Historically, crustal-scale faulting has been studied with two approaches: (1) as a static process in which fault orientation and failure criteria are evaluated, and (2) as a dynamic process focused on the mechanics of slip. In the first approach, the Mohr-

Coulomb [Coulomb, 1773; Mohr, 1900] failure criterion is commonly used to predict the shear stress required for rock failure, τ, as

$$\tau = C_o + \mu\sigma_n \quad (1)$$

where C_o is the cohesive strength, μ is the coefficient of friction and σ_n the stress normal to the plane of failure. A great deal of experimental work has been performed to determine the value of μ and the affect of rock friction on the process of dynamic fault slip. Byerlee [1978] compiled data from a large number of experiments and found that the maximum coefficient of friction is nearly independent of rock type. In rock specimens with a normal stress greater than 200 MPa, the relationship for shear stress as a function of friction is

$$|\tau| = 50 + 0.6\sigma_n \quad (2)$$

and for a normal stress less than 200 MPa,

$$|\tau| = 0.85\sigma_n \quad (3)$$

If the normal stress is assumed to be approximately equal to the overburden pressure then equation (2) is valid for all depths greater than ~6 km in the absence of pore fluid pressure. Equations (2) and (3), known as Byerlee's Law, demonstrate that fault roughness and the elastic properties of the rock are relatively unimportant in frictional behavior. From the Mohr-Coulomb solution, the coefficient of friction is

$$\mu = \tan\phi \quad (4)$$

where ϕ is the angle of internal friction. A fault forms at an angle $(90° - \theta)$ from the axis of maximum compressive stress, σ_1, where

$$\theta = \pm(45° - \phi/2) \quad (5)$$

The angle of internal friction for most rocks is ~ 30°, thus failure will occur on a conjugate pair of faults at an angle $\pm$ 30° from the maximum compressive stress.

Anderson [1951] combined the Mohr-Coulomb failure criteria with several basic assumptions about stress orientations to predict the orientation of faults in the Earth. Near

the surface of the Earth, one of the principal stresses is nearly vertical; thus, the orientations of the three principal faults, normal, reverse and strike-slip, can be predicted for a particular tectonic environment. In a compressive regime near the free surface, σ_1 and σ_2 (the maximum and intermediate compressive stresses) are horizontal and σ_3 (the minimum compressive stress) is vertical. Assuming ϕ=30°, this stress field will produce one or both of a conjugate pair of 30° dipping thrust faults with a strike parallel to σ_2. In an extensional environment, σ_1 is vertical and σ_2 and σ_3 are horizontal which results in 60° dipping normal faults. In regions where σ_1 and σ_3 are both horizontal, vertical strike-slip faults are formed at an angle of 30° from σ_1. One shortcoming of the theory is that it only relates the orientation of the faults to the stress field present at the time of fault formation. Because the frictional strength of a fault is less than the fracture strength of unbroken rock, once formed, a fault represents a plane of weakness which will continue to slip even if the stress field is no longer optimally aligned [Sibson, 1985]. Additionally, the theory predicts that one or both of a conjugate set of faults will develop, but provides no criteria for determining which fault to expect. In spite of this, the Anderson Theory of Faulting works quite well to explain most fault orientations, although there are notable exceptions such as low angle thrust and normal faults [Hubbert and Rubey, 1959].

Mohr-Coulomb failure combined with Byerlee's Law for rock friction predict that the stress required for failure is on the order of 1 kbar at depths of 8-10 km [Brace and Kolhstedt, 1979]. Further, from equations (1) and (2) we can see that the stress required for failure increases with depth thus, one would expect a fault to initiate at the free surface and rupture downward. On the other hand, dynamic measurements of rupture such as seismic stress drop or heat anomalies associated with fault motion imply that stress on faults is on the order of 10-100 bar [Zoback et al., 1987]. This is a subject of heated debate and the controversy remains to be resolved. The brittle failure of rocks has been

studied both experimentally and theoretically, and the field of modern fracture mechanics grew out of a major discrepancy between the two approaches. From the earliest experimental studies it was recognized that rock strength and the stress required for failure were incompatible. In general, the theoretical strength of rock, the stress required to break the atomic bonds in a crystal lattice, is several orders of magnitude greater than the stress required to break rock in the laboratory. Griffith [1920, 1924] proposed that the discrepancy between the observed and predicted strength of materials is due to the presence of microcracks which substantially reduce the strength of rock and control the growth of failure planes. Griffith formulated a criterion for extension of an isolated crack in a solid subjected to an applied stress, based on the fundamental energy theorems of mechanics and thermodynamics. Creating a new crack requires work in the breaking of molecular bonds, which increases the potential energy of the system. This increase is balanced by a reduction in the strain energy. If the rate of strain energy supplied to a crack tip equals the energy required to extend the crack, growth will occur.

The growth of a crack depends on the tip of the crack serving as a stress concentrator. The ability of a crack to concentrate stress depends on the type of displacement at the crack tip. There are three fundamental types of cracks. The simplest, Mode I, or tensile mode, is a crack which opens normal to the direction of crack propagation. The other two types of cracks have shear displacements. Mode II has displacements in the plane of the crack and along the direction of crack propagation. Mode III has displacements in the plane of the crack but normal to the direction of crack growth. A crack could be any combination of the three fundamental types, but in general, the shear motion of earthquake rupture is modeled with Mode II and Mode III cracks. The crack tip stress depends on the mode type and is proportional to $K_n r^{-1/2}$, where r is the distance from the crack tip. K_n is called the stress intensity factor (n is the mode type) and is a

function of the boundary conditions within the system. Griffith theory requires an energy balance for cracks to grow, which can be used to define the crack extension force, G, given by:

$$G = K_{II}^2(1 - \nu^2)/E \quad (6)$$

where E is Young's modulus and ν is Poisson's ratio. When G at the crack tip exceeds some critical value, G_C, unstable fracturing occurs. G_C, a material property determined experimentally, is dependent on rock type, pressure, and temperature. The scale at which G_C is measured, i.e., from a laboratory sample or a crustal feature, is also important in determining its magnitude. Absolute values of G_C for faulting processes in the crust are poorly constrained. G_C incorporates the energy required to fracture the rock and create new surface area. The G_C calculated for faults occurring in nature (Li, 1987) includes the energy expended to overcome friction and allow slip and crack growth on the existing fractures.

The dynamics of fracture growth is an area of active research. A number of modifications to Griffith's theory are now used and are being applied to predict rupture velocity and model the way faults grow with time. In this dissertation, conditions for fault growth are evaluated using the energy criteria of Griffith, specifically the shear fracture energy criteria for crack growth. The stress and strain relationships of the fault and surrounding region are modeled with the numerical technique of slippery nodes in the finite element formulation [Melosh and Williams, 1990]. A slippery node [Melosh and Williams, 1989] is a node in the finite element model which has an extra degree of freedom and allows differential slip across the node and element boundary. The node is represented as a free surface with no resolved shear stress and is allowed to slip in a specified direction [Melosh and Williams, 1989].

Crustal Scale Flexure

The earliest work in flexure of a plate was motivated by engineering design problems for structures and foundations such as the loading of a railroad track. Hetenyi [1946] developed the equations for flexure of finite beams on an elastic foundation which are now used extensively in thin-plate flexural analysis. Comer [1983] developed the full analytical solution for flexure of a thick plate. Thus, the governing equations for the analysis of flexure of a uniform elastic plate are well established. The challenge in flexure and buckling analysis lies in understanding regional variations in lithospheric strength due to thermal anomalies or mechanical weaknesses and the rheological properties of the upper mantle which are responsible for the plate-like behavior of the lithosphere.

The implausibility of elastic buckling in the lithosphere was first pointed out by Smoluchowski [1909a, b, c]. He demonstrated that the stress required to buckle the lithosphere is greater than the strength of crustal rock, thus faulting would occur before buckling. In the last two decades, several investigators have attempted to solve the buckling problem with elastic-plastic [McAdoo and Sandwell, 1985], plastic [Zuber, 1987], or viscoelastic rheologies [Lambeck, 1983]. These models generally result in a significant folding at stresses well below the fracture strength of the rocks.

In Chapter 4, I investigate the process of buckling a faulted lithosphere. Although the presence of inhomogeneities or weaknesses within the lithosphere have been recognized as a factor influencing the behavior of the plate, no one has incorporated them in their models. This study is the first to analyze the effect of faulting in a thick elastic lithosphere on the buckling response of the plate. A modification to the finite element formulation in which the position of each node is updated as deformation progresses was essential to modeling the buckling process [Wallace and Melosh, in prep]. Although the stress

required for buckling in the elastic models of Chapter 4 is still large, ~ 1 kbar, the presence of the faults can reduce the buckling stress three-fold and the buckling wavelength by one half. A similar analysis of buckling utilizing an elastic-plastic rheology and faults may be the key to understanding buckling in the lithosphere. The implications of the study are two-fold: (1) faulting is an important process for reducing the buckling stress and buckling wavelength, and (2) constraints on the effective Young's modulus and elastic thickness are developed for flexural models that utilize the thin and continuous elastic plate assumptions. As noted above, the thin plate approximation for flexure of a continuous plate has been applied to nearly every possible geologic flexure problem. The method is simple and provides reasonable results. Yet, we know that the lithosphere is neither thin nor continuous. This finite element analysis provides constraints on the effect of faults in the lithosphere for the flexure models of a thin, continuous plate.

CHAPTER 2

NUCLEATION AND GROWTH OF DIP-SLIP FAULTS IN A STABLE CRATON

Historically, there has been a discrepancy between numerical models of fault nucleation and growth and the earthquake data set. Numerical models of faulting in the crust that include the material property of increasing strength with depth predict that faults initiate at the free surface of the Earth where rocks are generally weak and the largest deviatoric stress occurs [Melosh and Williams, 1989]. However, the seismic record indicates that as many as 90% of the crustal earthquakes have hypocentral depths of 8-10 km (near the base of the seismogenic zone), suggesting nucleation of fault slip at depth. Crustal earthquakes are thought to be a result of a frictional instability allowing stick-slip behavior on a pre-existing surface. Because most earthquakes occur on pre-existing faults, it can be argued that the earthquake record is not representative of fault nucleation or growth but only fault rupture. Field evidence indicates that faults grow in width and displacement with repeated events but direct observation of the process of fault lengthening in the field or within a single earthquake is rare [Walsh and Watterson, 1988]. Fault nucleation at depth was proposed for fault growth in sedimentary sequences [Boyer and Elliott, 1981] as well as the Laramide basement-cored uplifts [Berg, 1962]. On the other hand, the 1968 Meckering, Australia earthquake (M_S=6.8) has been interpreted as a thrust fault which ruptured from near the surface downward to a depth of about 7 km [Langston, 1987]. Understanding the controls on fault rupture is fundamental to resolving the question of fault nucleation depth.

Fault growth can be modeled with linear elastic fracture mechanics by characterizing the displacement as either tensile opening (Mode I), in-plane shear (Mode II) or antiplane shear (Mode III). We use the finite element method in conjunction with a Mode II crack growth criteria to model fault growth. The analysis is done for a thrust fault but applies to normal faults as well. We limit the study to a stable cratonic environment and development of faults in crystalline rock. The effect of fault dip and shear fracture energy gradient on the magnitude of stress and the stability of fault growth is evaluated for three different crustal models to help understand the apparent discrepancy between numerical experiments and the seismic record.

Models of Fault Growth

Seismic faulting in the crust appears to involve shear fracture and frictional sliding rather than tensile fracture, although the development of tensile fractures plays an important role in the formation of macroscopic faults and all joints. Petit and Barquins [1988], Cox and Scholz [1988] and Melin [1988] have shown that Mode II cracks cannot exist as an primary fracture but develop as a secondary feature from Mode I tensile cracks. Laboratory and field studies suggest that shear failure corresponding to an earthquake rupture results from rapid growth and linking of microscopic fractures, tensile or shear, to form macroscopic zones of shear [McGarr et al., 1979; Segall and Pollard, 1983; Petit and Barquins, 1988].

Segall and Pollard [1983] investigated the formation of strike slip faults in granitic rocks in the central Sierra Nevada, California and found that faults did not propagate into intact rock in their own planes as shear fractures. Rather, adjacent shear fractures were joined by secondary, dilational fractures. As the number of secondary fractures increased, the shear fractures developed into larger fault zones with increased displacements. In

biaxial rock tests [Petit and Barquins, 1988], shear zones develop within samples through the coalescence of en echelon Mode I microcracks, similar to the observations of Segall and Pollard [1983]. Reches [1990] used acoustic emissions to monitor crack initiation in the laboratory and observed that cracks are most frequently initiated at the edge of the sample. Cox and Scholz [1988] also observed that the cracks initiate at the edge of the samples rather than the centers in triaxial, Mode III shear tests. The large-scale shear failure typically follows a plane of high shear stress with little change in fault orientation. We model the fault as a Mode II crack which grows within its own plane as a result of degradation of the rock strength by microscopic fractures.

The majority of all crustal earthquakes initiate at depths of 5-15 km. Controls on the maximum depth include temperature, pressure, strain rate, lithology, and the presence of fluids [Chen and Molnar, 1983; Meissner and Strehlau, 1982; Sibson, 1982,1984]. Sibson [1982] assumed that all frictional sliding on faults is of the stick-slip variety and thus occurs seismically. Further, he proposed that the depth of seismicity is controlled by the transition from brittle to ductile rheology. Tse and Rice [1986] concluded that not all frictional sliding is stick-slip and suggested that the depth of seismicity is controlled by the transition from stick-slip behavior to stable sliding. Thus, fault formation and displacement could occur without any corresponding seismicity. Miller and Furlong [1988] suggested that the maximum depth of seismicity can be controlled by the magnitude of the principal tectonic stress and individual fault development in the region and not necessarily by the brittle-ductile transition. Marone and Scholz [1988] found that the minimum depth of seismicity is governed by the presence of fault gouge, low strength rock or a poorly developed fault. Poorly developed faults with little or no gouge show stick-slip seismicity at all depths, while well developed faults with gouge are seismically active only at depths where the gouge is thin. How these conditions affect fault nucleation and, more

importantly, our observation of that process is unknown. In this study, we evaluate the role of lithology and shear fracture energy on fault nucleation and growth.

Fracture Mechanics Model

We analyze conditions for nucleation and growth on a planar dip-slip fault by assuming that the fault can be modeled as a Mode II crack in an elastic body under plane strain. The crack has an initial length of $2a_0$ and dips at an angle, ß to the principal horizontal stress, σ_1 (Figure 1). Using linear elastic fracture mechanics (LEFM), the near-field approximation of the shear stress at the crack tip is

$$\tau = \frac{K_{II}}{\sqrt{2\pi R}} \left\{ \cos\left(\frac{\Theta}{2}\right)\left[1 - \sin\left(\frac{\Theta}{2}\right)\sin\left(\frac{3\Theta}{2}\right)\right]\right\} \qquad (1)$$

where τ is the shear stress parallel to the fault, K_{II} is the Mode II stress intensity factor and R is a radial distance from the crack tip to a point in front of the crack tip. Θ is the angle between the fault plane and a point of known shear stress, measured positive in the counter clockwise direction [Lawn and Wilshaw, 1975]. K_{II} is a function of crack geometry and boundary conditions on the crack and body and can include the effects of friction or material layering. Solutions for K_{II} can be found in general reference books [see Paris and Sih, 1965; Tada, Paris and Irwin, 1973; and Rooke and Cartwright, 1976]. LEFM predicts that the stresses become infinite at the crack tip as R approaches zero. In reality, stress at the tip remains finite due to yielding and stress relaxation in a small region at the crack tip known as the process zone. Within the process zone increased fracturing of the rock occurs by non-linear processes before the fault propagates. As crack length increases, the process zone is thought to enlarge and the shear stress required for failure decreases. Several models were evaluated to choose a process zone size, R_p, which would allow

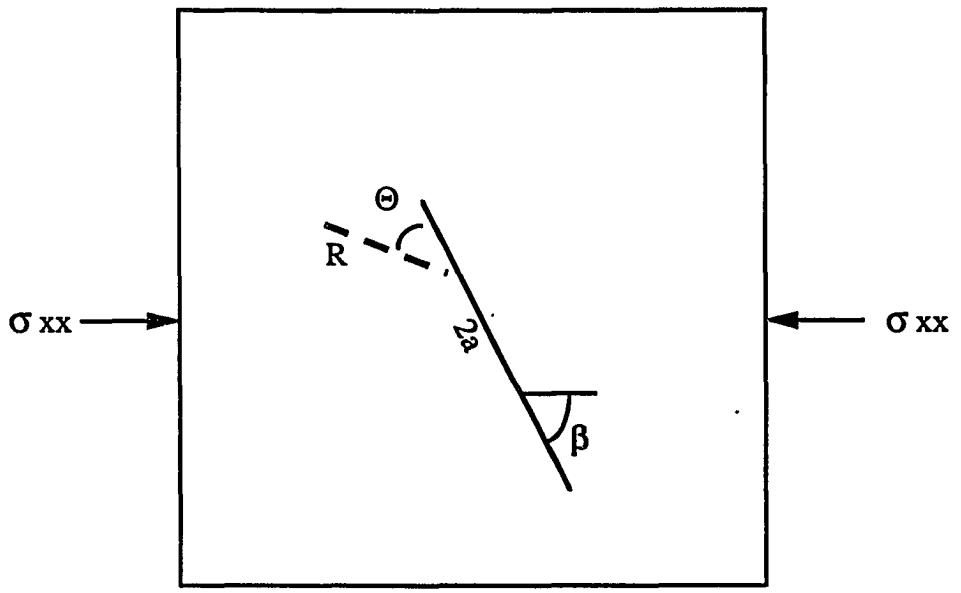

Figure 1: Model of a single crack of length 2a in a body under compressive stress. The crack dips at an angle ß to the maximum horizontal stress. Stress in the region of the fault tip is calculated at a distance R and an angle Θ to the plane of the crack.

reasonable stresses for fault growth. We chose an $R_p = 0.05\ a_o$, to reflect a reasonable area in front of the crack tip that is yielding. Any other R_p calculated as a function of crack length would result in similar fault behavior. The magnitude of R_p has an effect similar to G_c, the shear fracture energy, and, as such, will only affect the magnitude of the shear stress needed for fault growth and not the general fault behavior.

Unstable crack propagation leading to fault rupture occurs when G, the energy release rate, reaches a critical value G_c. G is related to K_{II} by (for plane strain)

$$G = \frac{(1 - \nu^2)}{E} K^2_{II} \tag{2}$$

where ν is Poisson's ratio and E is Young's modulus. Combining equations (1) and (2), and setting $G = G_c$ and $R = R_p$ gives the criteria for crack growth:

$$G_c = \frac{(1 - \nu^2)}{E} \frac{\tau^2 2\pi R_p}{\left\{\cos\frac{\Theta}{2}\left[1 - \sin\left(\frac{\Theta}{2}\right)\sin\left(\frac{3\Theta}{2}\right)\right]\right\}} \tag{3}$$

From equation (3) we can determine the stress at the edge of the process zone required to propagate the fracture. G_c, a material property determined experimentally, is dependent on rock type, pressure, and temperature. The scale at which G_c is measured, i.e., from a laboratory sample or a crustal feature, is also important in determining its magnitude. Absolute values of G_c for faulting processes in the crust are poorly constrained. G_c incorporates the energy required to fracture the rock and create new surface area. The G_c calculated for faults occurring in nature [Li, 1987] include the energy expended to overcome friction and allow slip and crack growth on the existing fractures. We know from laboratory studies that the frictional and fracture strength of rocks increases with

increasing pressure or depth. Stuart and Mavko [1979] proposed a model for the San Andreas Fault in which G_C increased as an exponential function of depth down to the base of the seismogenic zone before rapidly decreasing in the aseismic zone. Laboratory studies by Wong [1986] indicate values of G_C increase linearly with increasing pressure and temperature. At lower crustal pressures, G_C values are on the order of 1×10^4 J/m^2 but range over an order of magnitude. These values are still two orders of magnitude smaller than the G_C values calculated from seismic events on active faults [Li and Rice, 1983; Li, 1987]. Presumably, the higher G_C values calculated for real faults are indicative of the total energy required to overcome friction, complications in fault plane structure and degradation of the rock surrounding the fault plane.

We have chosen to use two different G_C gradients to model the increase in shear fracture energy with depth (Figure 2c). We simplified the model of Stuart and Mavko [1979] and assume G_C increases linearly to a depth of 15 km in all models. The shear fracture energy at the surface is always 1×10^5 J/m^2 and increases to either 1×10^6 J/m^2 (low G_C gradient) or 1×10^7 J/m^2 (high G_C gradient). Below 15 km depth, G_C decreases rapidly to 1×10^5 J/m^2 to reflect the low shear strength of the aseismic crust. The material properties include the effects of a uniform number and distribution of cracks and defects in the process zone in front of the crack tip. The magnitude of G_C is only important for calculations of absolute values of shear stress necessary for failure. The stability of fault growth indicated by the results of our modeling is relatively independent of the magnitude chosen for G_C but not the gradient.

The seismic moment associated with the fault growth is calculated as

$$M_0 = \mu DA \qquad (4)$$

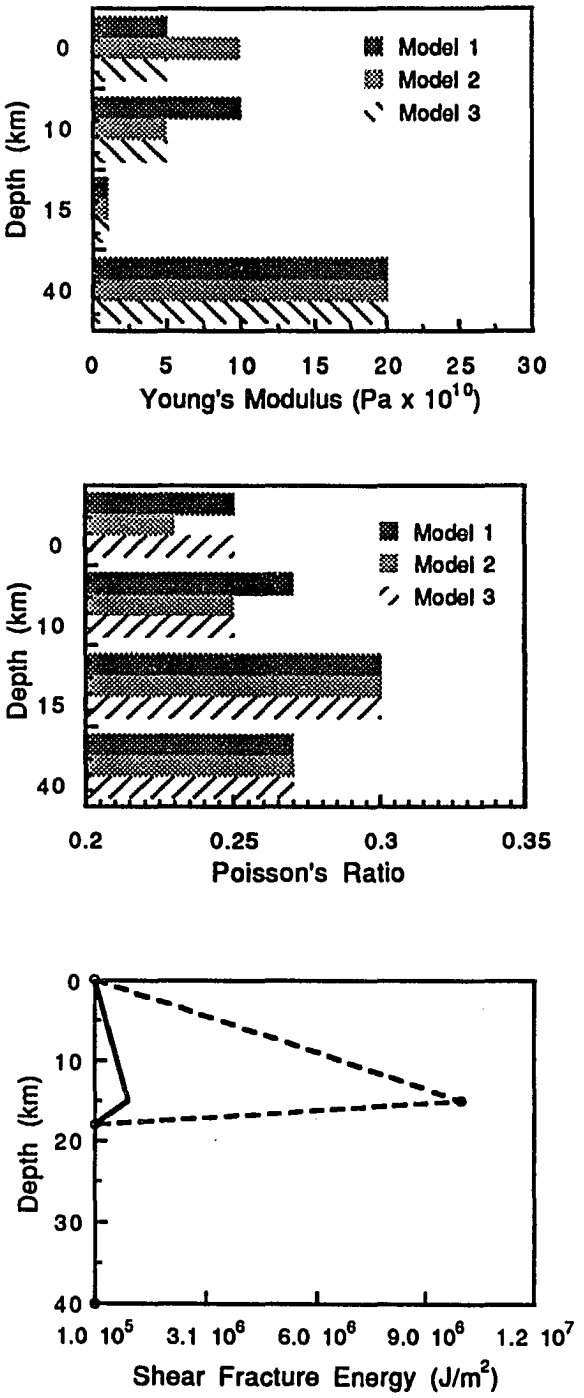

Figure 2: Elastic parameters for the three crustal models. (a) Young's modulus, (b) Poisson's ratio, and (c) G_C, shear fracture energy, as a function of depth. Shear fracture energy represents the energy required to initiate crack growth. The curves chosen represent two possible members of a suite of curves that are constrained by calculations of G_C from earthquake events.

where μ, the shear modulus is 3×10^{10} Pa, D is the average displacement on the fault, and A is the area of the fault. For the calculation of the moment, the fault is assumed to be circular with a radius of a_0, the half length of the fault. In addition to the requirement that $G = G_C$ for crack growth, the displacement at any point on the fault must remain constant or increase at every step of fault growth. Although the average displacement at any step of fault growth may decrease, the displacement at every point must remain constant or increase, i.e., the model does not allow a fault to "overshoot" in displacement then readjust, as it grows.

Mechanical Model

The finite element model has 849 nodes and 1044 quadrilateral elements (Figure 3). Faults initiate along the dipping boundaries of the triangular and diamond shaped elements in the center of the grid. The length of the grid varies from 257 km to 373 km to accommodate changing fault dips, while the depth of the grid is constant at 100 km. Constant thickness for all models keeps the tip of the fault at the same depth for all dip angles, as it grows from one node to the next. The shear stress is calculated at the edge of the process zone, a distance R_p from the fault tip. We calculate the crack tip stress in a multi-step process. From the finite element calculation, we know the stress at the centroid's of all the elements in the grid. For the elements within a 90° arc in front of the crack tip, we then perform a simple transformation of axis and calculate the shear stress parallel to the crack at the centroid's of the elements. These values of shear stress are interpolated to the edge of the process zone and averaged to get the shear stress at the crack tip. The interpolation function incorporates the rapid increase in shear stress as R approaches zero [Sneddon and Lowengrub, 1969; Lawn and Wilshaw, 1975].

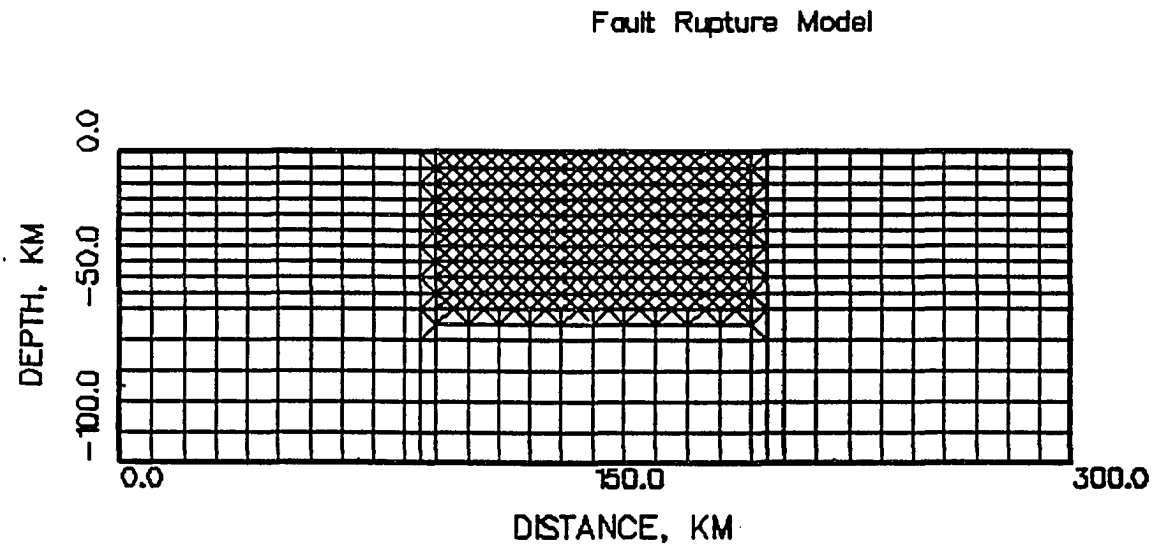

Figure 3: Finite element model with 1044 elements and 849 nodes. Length of the grid is varied from 257 km to 373 km to accommodate changes in fault dip. Grid displacement is fixed in the vertical direction along the base of the grid while uniform horizontal displacements are applied to the vertical sides of the grid.

In our model, a layered elastic lithosphere is subjected to far-field horizontal displacement boundary conditions and is free to move horizontally along its base but is fixed in the vertical direction. We assume that the vertical and horizontal gravitational stresses in the crust are equal to the lithostatic stress [McGarr, 1988]. Elastic moduli for the various models evaluated are listed in Table 1 and Figure 2. Assuming a cold cratonic environment, stick-slip behavior of faults would be expected to at least 15 km, the depth at which the material strength is significantly reduced in all models in Table 1.

All models include a seismogenic zone from 0-15 km depth, an aseismic layer with reduced stiffness and shear modulus between 15 and 40 km, and a strong rigid mantle from 40-100 km (Figure 2). Model 1 represents an average crust with a granitic rheology from 0-10 km overlying a stronger, diabase rheology from 10-15 km depth. In Model 2, a strong diabase between 0-10 km overlies a slightly weaker diabase from 10-15 km forming a seismic zone with decreasing elastic strength with depth. A single layer granitic crust from 0-15 km is represented by Model 3. For all evaluations G_C increases with depth. Thus, comparison of a crustal model of decreasing strength with depth, Model 2, with a crustal model of increasing strength with depth, Model 1, should give insight into the role of the G_C gradient on failure.

We model a fault as a slippery node [Melosh and Williams, 1989], which is a node in the finite element model which has an extra degree of freedom and allows differential slip across the node and element boundary. The node is represented as a free surface with no resolved shear stress and is allowed to slip in a specified direction [Melosh and Williams, 1989]. Presently, a slippery node does not account for friction that is present along the fault surface. In light of the present understanding of the state of stress on a fault plane during rupture, i.e. stress and therefore friction along the fault are relatively low [Kanamori, 1980; Zoback et al., 1987], this appears to be an acceptable simplification in

TABLE 1: Elastic Moduli for Lithospheric Models of a Stable Craton

Model	Depth (km)	Young's Modulus, E (Pa)	Poisson's Ratio, ν
1. Average Crust	0.0	5.0×10^{10}	0.23
	10.0	1.0×10^{11}	0.25
	15.0	1.0×10^{10}	0.30
	40.0	2.0×10^{11}	0.27
2. Decreasing Strength with Depth	0.0	1.0×10^{11}	0.23
	10.0	5.0×10^{10}	0.25
	15.0	1.0×10^{10}	0.30
	40.0	2.0×10^{11}	0.27
3. Single Material	0.0	5.0×10^{10}	0.23
	15.0	1.0×10^{10}	0.30
	40.0	2.0×10^{11}	0.27

the model. A constant value of friction along the fault would require a higher far-field stress to initiate rupture in our model but the relative behavior would not change. The increase in the frictional/fracture strength with depth is taken into account by linearly increasing the G_C value with depth. In the future, we plan to include friction in the formulation of the slippery node, and the effects of friction along the fault surface can be explicitly considered.

All faults initiate at either the surface or base of the seismogenic zone, at depths of 0 and 15 km depth, respectively. Each fault initiates as a crack 1 km long and grows to a length between 17 and 30 km, depending on dip. A fault grows by one node increments from 1 to 7 nodes, by increasing the stress in the grid to reach failure when necessary. The initial model contains one slippery node representing the initial crack. A horizontal displacement is applied at the boundaries until the shear fracture energy at the fault tip node is sufficient to cause growth. Once the node has reached the critical energy for growth, we assume the fault is capable of rupturing to the next node in the fault plane. Then, that node is changed to a slippery node and the process continues until the fault has grown through the seismic zone. For the case of rupture upward, the criteria for fault growth is evaluated at 6 nodes beginning at 15 km depth and progressing to the surface. The seventh node lies at the surface and once it is changed to a slippery node the fault has grown completely through the crust. Thus, satisfying the growth criteria at the seventh node is not necessary. Rupture downward includes evaluation of fault stability or growth at the seventh node which lies on the boundary between the seismic and aseismic zones.

MODEL RESULTS

Strain

Our results confirm that fault rupture upward required a larger strain than fault rupture downward, suggesting that it is more difficult to initiate rupture at depth (Figure 4). Strains required for fault growth in our crustal models are on the order of 1×10^{-5} to 1×10^{-4} and are comparable to strains observed for earthquakes. In general, fault nucleation and growth downward requires less than one half as much total strain as nucleation and growth upward. To evaluate the effect of dip on the strain required for failure and subsequent fault growth, we evaluated Model 1 using fault dips of 30°, 45° and 60° and found that the strain required for initial failure was independent of dip. However, differences in the minimum strain required for fault growth are evident between the crustal models. Model 2 requires 30% less strain to rupture downward than crustal Model 1 or Model 3 because the fault starts in a strong layer of diabase rather than granite (Table 1).

Previous analyses of fault growth using the Mohr-Coulomb failure criterion [Williams, 1990; Melosh and Williams, 1989; Wallace et al., 1990; Wallace and Kemeny, 1990] indicate that failure of rocks at depth is much more difficult to achieve than failure at the surface. Melosh and Williams [1989] and Williams [1990] showed that within a single layer crust, faults will always nucleate at the surface. Wallace et al. [1990] evaluated fault growth within a layered crust using the Mohr-Coulomb criteria and found that a fault will nucleate at depths near 10 km only if there is a significant contrast in the elastic properties between the surface and at depth, and if the rocks at the surface are generally weak. Rocks become stronger under increasing confining pressure and therefore the critical stress necessary for failure should increase with depth. Yet, earthquake data show that for the majority of events, rupture initiates at depths of 8-10 km in the continental crust and

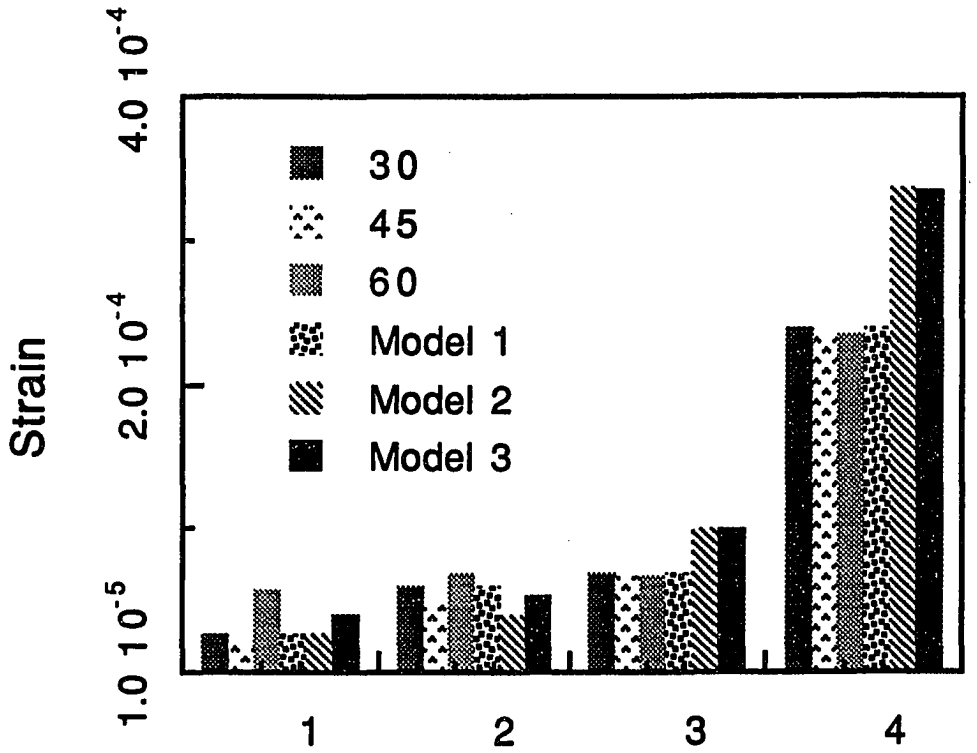

Figure 4: Maximum strain required for fault growth through the seismogenic zone. The graph shows strain levels for 4 categories: (1) rupture downward with a maximum $G_C = 1 \times 10^6$ J/m^2, (2) rupture upward with a maximum $G_C = 1 \times 10^6$ J/m^2, (3) rupture downward with a maximum $G_C = 1 \times 10^7$ J/m^2, (4) rupture upward with a maximum $G_C = 1 \times 10^7$ J/m^2. Comparison of group 1 and 2 or 3 and 4 indicates that rupture upward requires a minimum of 50% more strain than rupture downward. Only minor differences in the required strain are observed for faults with different dip. However, major differences are observed between the different crustal models.

propagates to the surface, and only rarely initiates at the surface where the crust is weakest and propagates downward.

Stability of Rupture

Rupture instability, the ability of a fault to continue growth without adding strain to the system, was evaluated for all crustal models, G_C gradients, dip, and rupture direction. A fault begins to grow when the condition $G \geq G_C$ is met and continues until $G < G_C$. Two general conclusions can be drawn from our analysis: (1) rupture upward from the base of the seismogenic zone, where G_C is greatest, is always unstable, and (2) rupture in a downward direction using the low G_C gradient (1×10^5 to 1×10^6 J/m^2) is always unstable, independent of all other factors. In these models, once a fault nucleates and reaches the point of failure, it ruptures unstably through the seismogenic zone as an earthquake. This result does not address why the fault would nucleate at a particular depth: only that once it has nucleated and reaches failure, it ruptures through the crust. On the other hand, stable growth of a fault only occurs when the shear fracture energy increases rapidly with depth and rupture initiates at the surface. In the following sections we discuss the details of rupture patterns and associated changes in stress at the fault tip.

Rupture Upward

For all cases of rupture upward, the shear stress required for fault growth is always less than the stress available once fault growth begins, independent of fault dip or crustal model. The required stress is the magnitude of shear stress necessary for the condition of fault growth and the available stress is the magnitude of stress present in the process zone. Figures 5 and 6 show the change in shear stress, both available and required, with increasing fault length for both high and low G_C gradients. Each data point represents a

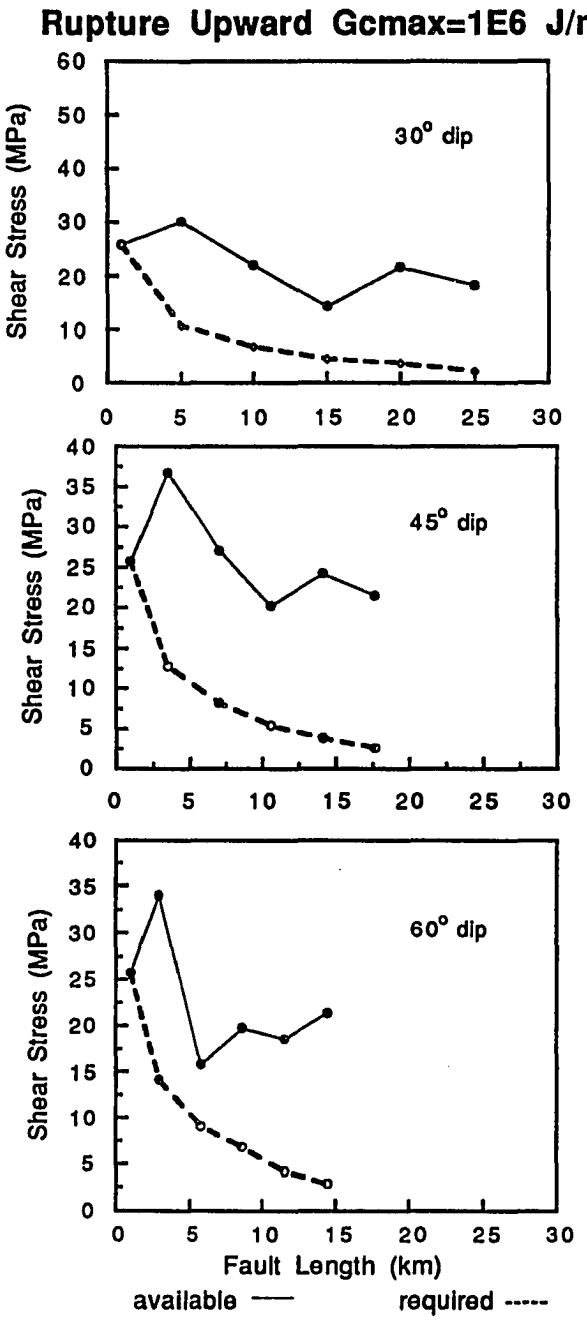

Figure 5a: Fault stability for rupture upward with $G_c=1x10^6$ J/m^2. Points at which the curves coincide indicate stages at which crack growth stabilized and additional strain was required to continue growth. Comparison of rupture stability for Model 1 with 30°, 45° and 60° dipping faults. Fault initiates at the base of the seismogenic zone and ruptures unstably to surface. Required stress decreases as fault length increases. Variability is a function of dip, fault length, and far-field stress.

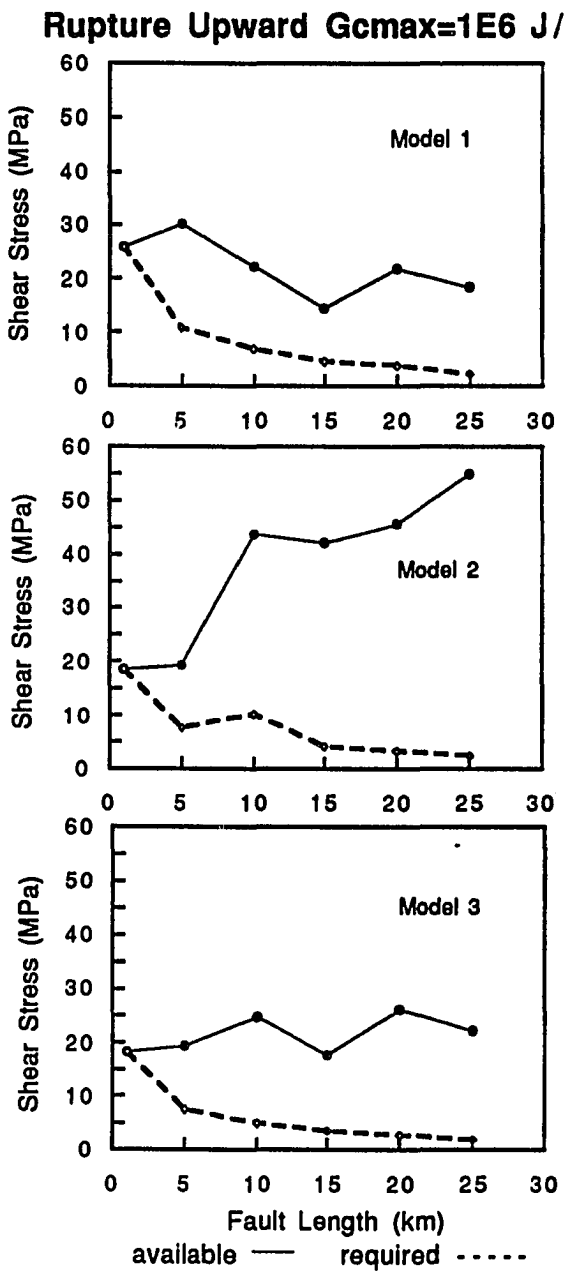

Figure 5b: Fault stability for rupture upward with $G_C=1x10^6$ J/m^2. Points at which the curves coincide indicate stages at which crack growth stabilized and additional strain was required to continue growth. Comparison of rupture stability for the 3 crustal models. Increase in required stress at node 3 in Model 2 results from fault growth from a low stress lower crustal layer to a higher stress upper crust layer. Model 2 has increasing available stress as the fault grows into regions with increasing far-field stress. See text for further discussion of variability in available stress.

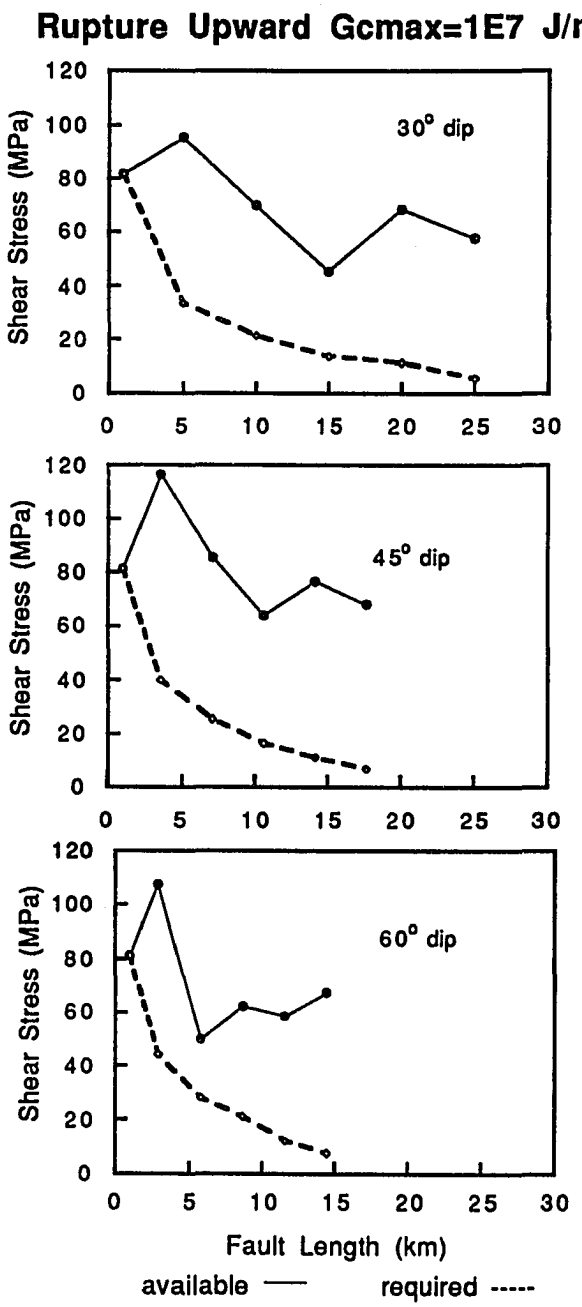

Figure 6a: Fault stability for rupture upward with $G_c=1x10^7$ J/m^2. Points at which the curves coincide indicate stages at which crack growth stabilized and additional strain was required to continue growth. Curves differ from figure 5 only in magnitude of shear stress. Comparison of rupture stability for Model 1 with 30°, 45° and 60° dipping faults. Fault initiates at the base of the seismogenic zone and ruptures unstably to surface. Required stress decreases as fault length increases. Variability is a function of (1) dip, (2) fault length, and (3) far-field stress.

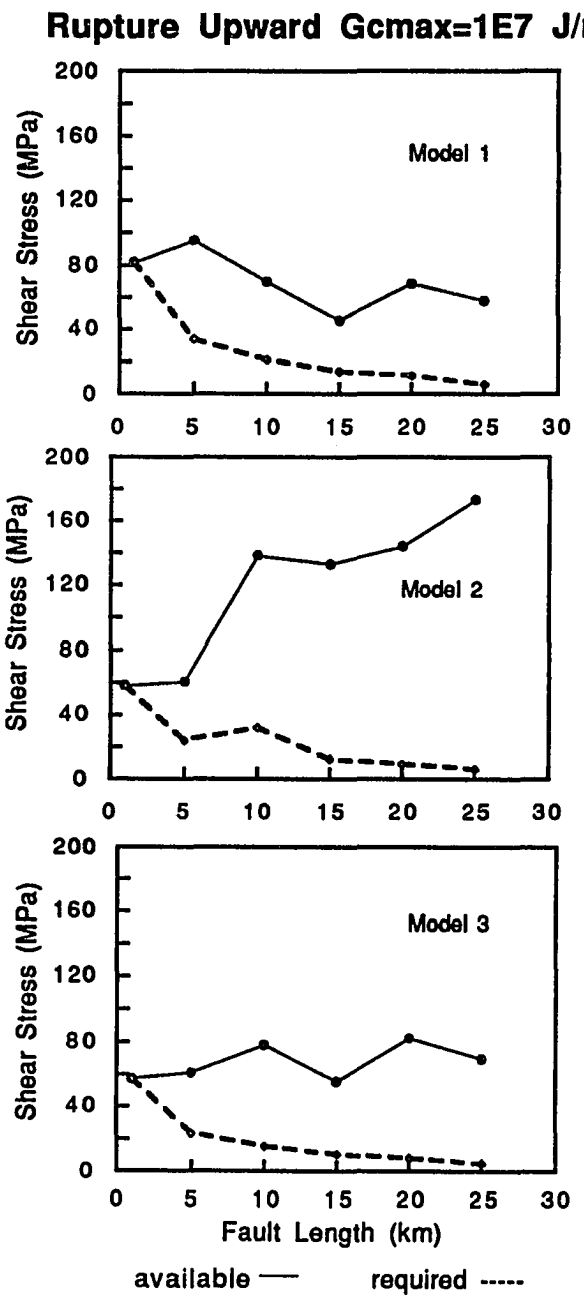

Figure 6b: Fault stability for rupture upward with G_C=1x10^7 J/m^2. Points at which the curves coincide indicate stages at which crack growth stabilized and additional strain was required to continue growth. Curves differ from figure 5 only in magnitude of shear stress. Comparison of rupture stability for the 3 crustal models. Increase in required stress at node 3 in Model 2 results from fault growth from a low stress lower crustal layer to a higher stress upper crust layer. Model 2 has increasing available stress as the fault grows into regions with increasing far-field stress. See text for further discussion of variability in available stress.

node in the finite element grid at which the fault tip is located. Points at which the curves coincide indicate stages at which crack growth stabilized and additional strain was required to continue growth.

The pattern of shear stress for a particular crustal model changes only in magnitude for the different G_C gradients but variations in shear stress for different crustal models and fault dips are evident. Figures 5a and 6a show the change in shear stress with respect to changes in fault dip. Crustal Model 1 was used in the analysis of dip, which was varied from 30° to 45° to 60°. The required stress decreases smoothly for all fault dips as the fault length increases, while the available stress shows more variability. The variability of the available fault tip stress as the fault grows is a function of (1) fault length, (2) dip angle, and (3) far-field stress, which at a specific depth is a function of the material properties. For the 30°, 45°, and 60° fault dips, the fault length increases dramatically from an initial value of 1 km to 5.0, 4.33, and 2.8 km at the second node, respectively. All subsequent fault length increases are uniform and smaller in size.

The large increase in the available stress between the first and second nodes (the first and second data points) of the fault rupturing upward (Figure 5a and 6a) is in response to both the large increase in fault length between nodes 1 and 2 and an increase in far-field stress between the two nodes. Node 1 lies at 15 km depth on the border between the low shear zone and the diabase layer in Model 1, therefore the far-field stress at this location is an average of the stress in the two layers. Node 2, at 12.5 km depth, lies completely within the higher stress diabase layer. Thus, as the fault grows from node 1 to node 2 it moves into a layer with higher available stress. As the fault continues to grow, it ruptures into a low stress granite layer and the available stress begins to decrease. Node 3 lies on the boundary between the diabase and granitic layers in Model 1, thus the tip stress at that point is an average of both the higher stress environment of the diabase and the lower stress

of the granite. Node 4 has a lower stress due to its location in the granitic material. The effect of changing dip and fault length is evident in the available stress pattern between nodes 3 and 4, and 5 and 6. As the dip increases and fault length decreases the minimum in the available stress curve moves from node 4 in the 30° and 45° models to node 3 in the 60° model. In addition, between nodes 5 and 6 the slope of the available stress curve changes from positive to negative at 60°.

A comparison of rupture stability for the three different crustal models evaluated with a fault dip of 30° indicates rupture in the upward direction is unstable for all cases as well (Figure 5b and 6b). Again, the shape of the shear stress curves is identical for a model evaluated at either G_C gradient, differing only in magnitude. The similarity in the available stress curves for Models 1 and 3 are a result of the similar material properties for the upper layer in both models. The last three nodes in Model 1 and Model 3 lie in the same material thus, the required stress for the nodes common to both models is the same. However, Model 3 requires a greater initial strain resulting in an overall higher available stress as compared to Model 1. The differences in the available stress curves are a result of the fault in Model 1 initiating in a higher stress region than the fault in Model 3. The effect of the lower initial far-field stress in Model 3 is observed in the smaller jump in stress available between node 1 and 2. The available stress increases at node 3 with increasing fault length in Model 3. While in Model 1, the available stress decreases as the fault grows from a high stress region into the lower stress upper crustal layer.

In Model 2, the available stress increases only slightly while the fault remains in the low stress diabase (Figure 5b and 6b). Then, as the fault moves into the higher stress diabase a dramatic increase in the available stress occurs. Overall, the magnitude of the available stress increases significantly as the fault grows, a phenomenon not observed in Models 1 and 3. Model 2 differs from others in that the required stress for failure at node 3

increases as the fault moves from the lower stress layer into the higher stress upper layer. As we will discuss later, a similar behavior occurs for faults rupturing downward from a lower stress layer to a higher stress layer. In Model 2 the available stress increases steadily as the fault grows into a region of higher stress, whereas the stress required for growth decreases as the G_C decreases, making rupture increasingly unstable.

Rupture Downward

Rupture downward is essentially unstable for the low G_C gradient for all dips and crustal models. However, the amount of available stress in the initial stages of fault growth is not significantly greater than the stress required (Figures 7 and 8). As the dip angle increases the changes in required stress are much smaller. Faults with a 30° or 60° dip also appear much closer to a point of stable rupture than the 45° dipping fault (Figure 7a and 8a). The frictional stress included in calculations of G_C for natural faults is uniform for all fault orientations. The variation in shear stress at the fault tip for the three different dips is simply a function of the angle between the maximum principal stress and the fault plane and reflects the preferred 45° orientation of the stress free fault plane. For both G_C gradients, rupture downward of the fault proceeds to the boundary between the seismic and aseismic layer but rupture will not continue into the aseismic zone unless strain is increased in the system. Again, the available stress curves show much variability in magnitude due to dip angle, far-field stress and fault length. The stress required and available for failure in Model 1 shows a marked increase at the fifth node point which is not observed in Models 2 and 3 (Figure 7b and 8b). The increase is a result of the fault growing from the layer of granite with a lower stress into the layer of diabase with a higher stress. Models 2 and 3 do not show an increase at node 5 because they grow into regions in which the far-field stress either drops or remains constant. The required and available stress in Model 2 decreases

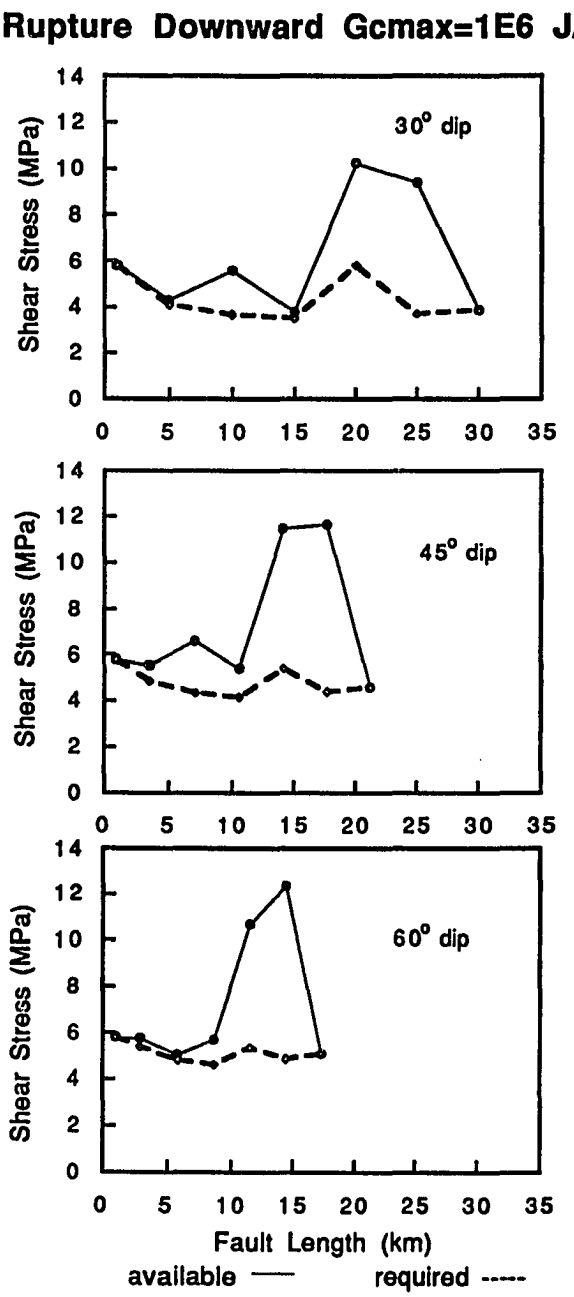

Figure 7a: Fault stability for rupture downward with G_C=1x10^6 J/m^2. Where curves coincide indicates points of stable rupture and for additional growth to occur strain must increase in the model. Comparison of rupture stability for Model 1 with 30°, 45° and 60° dipping faults. Fault initiates at the surface and ruptures unstably to the base of the seismogenic zone. The increase in the required and available stress at node 5 for all dip angles corresponds to a change in material properties.

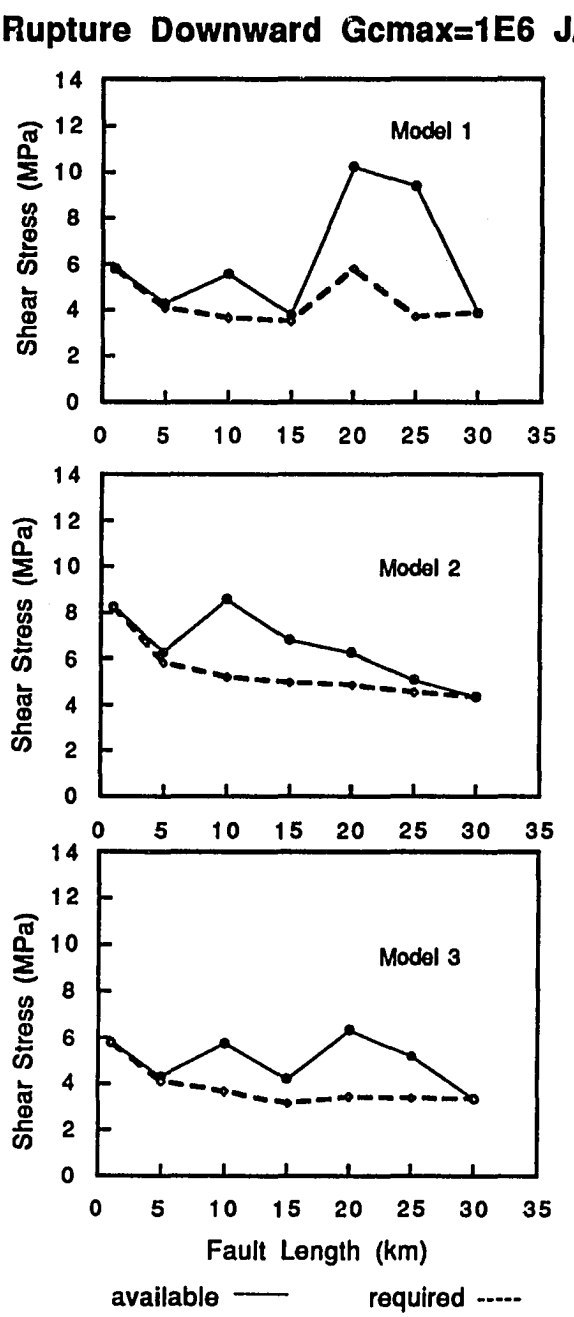

Figure 7b: Fault stability for rupture downward with $G_C=1x10^6$ J/m^2. Where curves coincide indicates points of stable rupture and for additional growth to occur strain must increase in the model. Comparison of rupture stability for the 3 crustal models. Again, the fault is able to rupture unstably through the entire seismogenic zone. The required stress declines as the fault length increases except in Model 1. As noted above, the increase at node 5 in Model 1 corresponds to a change in material properties as the fault grows from a lower stress region into a higher stress region. See text for additional discussion of variability in available stress.

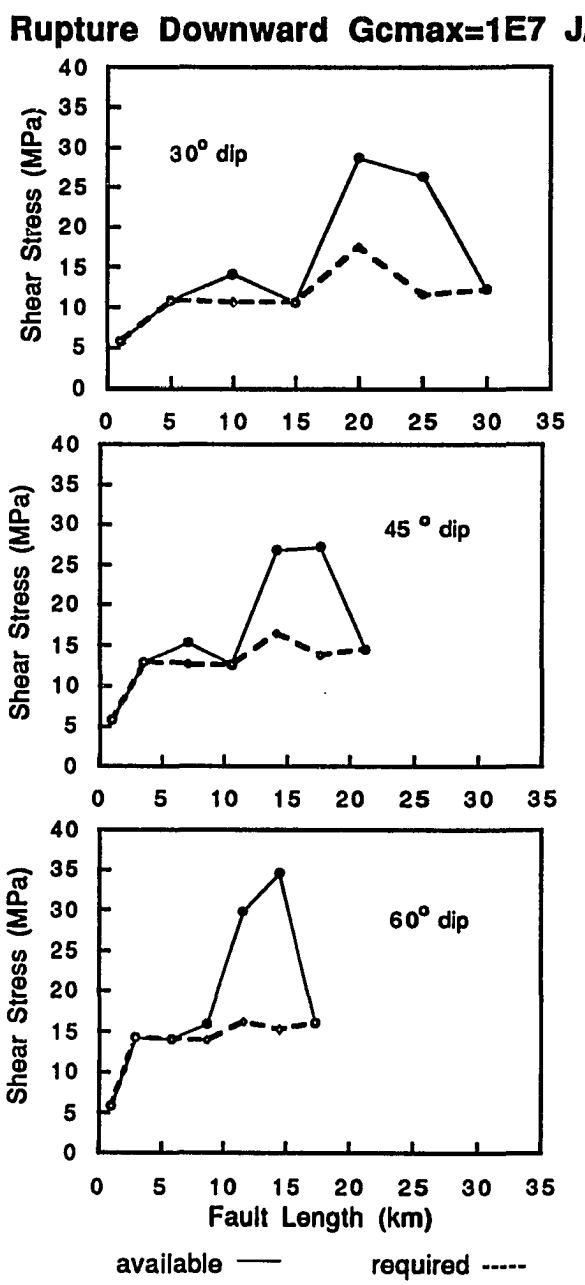

Figure 8a: Fault stability for rupture downward with $G_C=1x10^7$ J/m^2. Where curves coincide indicates points of stable rupture and for additional growth to occur strain must increase in the model. Comparison of rupture stability for Model 1 with 30°, 45° and 60° dipping faults. Fault initiates at the surface and requires several increases in far-field strain to rupture to the base of the seismogenic zone. Fault growth is stable for all 3 models until the fault length is greater than 5 km. The 30° and 45° dipping faults require additional strain once the fault tip reaches the boundary between the two layers of the seismogenic zone, while the 60° fault ruptures to the base of the seismogenic zone. All models require additional strain to rupture into the aseismic zone.

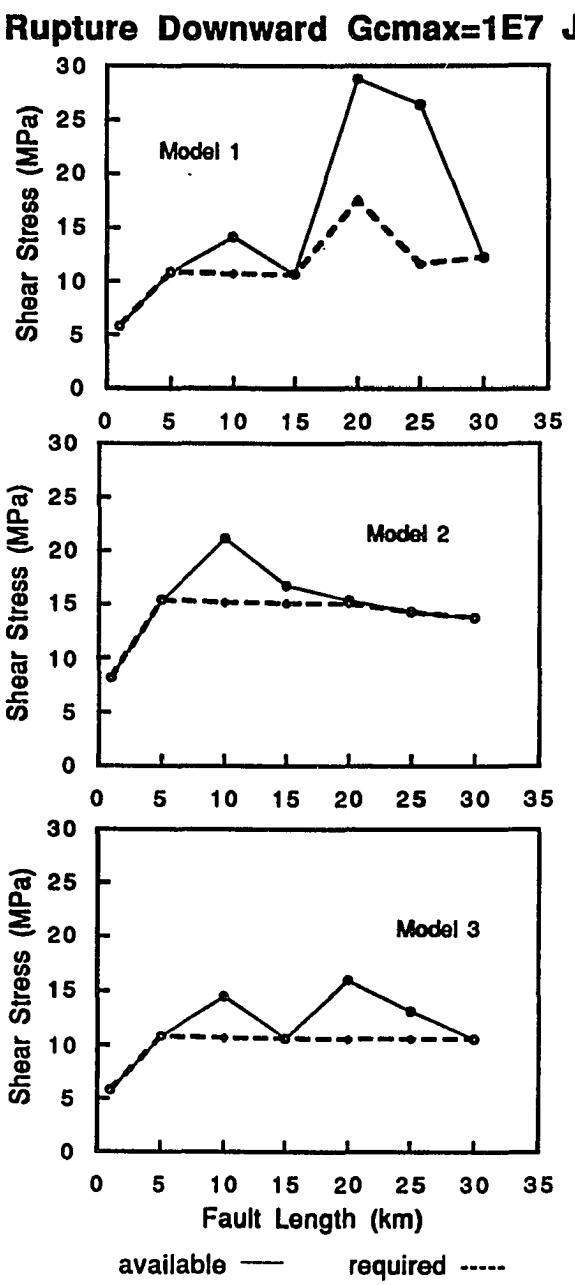

Figure 8b: Fault stability for rupture downward with $G_C=1x10^7$ J/m^2. Where curves coincide indicates points of stable rupture and for additional growth to occur strain must increase in the model. Comparison of rupture stability for the 3 crustal models. All models indicate the fault would grow by stable increments to a length of 5 km. Models 1 and 3 require additional strain to rupture beyond 15 km in length. Model 2 ruptures unstably until it reaches the low stress region in the lower part of the seismogenic zone and all models require additional strain to rupture into the seismogenic zone. See text for discussion of variability in available stress.

slightly as the fault grows from the high stress diabase layer into a lower stress diabase layer. In Model 3 the required stress is nearly constant, reflecting equal increases in G_c and R_p with no change in elastic moduli. It is interesting to note that the required stress for rupturing through a material boundary increases significantly at that boundary but once the fault progresses into the higher stress layer the required stress drops to near the value prior to entering the second layer.

At the higher G_c gradient, rupture downward is stable over significant lengths of the fault for all crustal models and dip angles. Faults with a 30° or 45° dip indicate that stable rupture occurs at the first and second nodes as indicated by the large increase in required stress between the two nodes and overlaying data points (Figure 8a). The 60° dipping fault grows in a stable manner for the first three nodes, and at all three dip angles rupture is stable to near 5 km fault length. The 60° fault will be unstable and rupture to the base of the seismogenic zone once past the third node but the 30° and 45° dipping faults reach a stable point again at the fourth node before rupturing to the base of the seismogenic zone. The same pattern occurs for the 30° fault in Model 3 (Figure 7b and 7b) because it has the same initial layer and shear fracture energy gradient through node 4 as Model 1. Model 2, with decreasing strength with depth grows through stable increments for the first two nodes and last two nodes but would allow unstable rupture between those points.

For either G_c gradient, the available stress decreases to the level of the required stress at node 4 in Models 1 and 3 rather than the required stress increasing to cause stable rupture. The large drop in stress does not correspond with an overall stress drop for the system, only a local change in tip stress. The cause of this behavior is puzzling. It does not appear to be a function of fault length because it is not observed in both the faults rupturing up and down. Further, within Model 1 it only occurs for the 30° and 45° faults. Thus it appears to be a function of dip angle. The behavior is not observed in Model 2

which suggests it may also be a function of crustal model. The most obvious conclusion is that the fault has achieved an optimum configuration to stabilize fault growth and reduce the stress in the fault region.

In all models, the increase in G_c is equal to the increase in R_p after the fault is two nodes long. Because G_c and R_p have equal and opposite effects on the required and available stress after node 2, the changes in those curves are independent of them. The increase in material strength and G_c with depth in Model 1 results in an increase in both the required and available stress in the lower layer of the seismic zone. In Model 2, strength decreases and G_c increases with depth resulting in a slight decrease in required and available stress as the fault ruptures from the higher strength diabase layer into the lower strength diabase layer at depth. Model 3 has a single layer crust with an increasing G_c with depth which results in a uniform far-field stress and a nearly constant required stress.

Displacements

Average displacements along the fault decrease with increasing dip and decreasing fault length for both upward and downward propagation, a result supported by field observations [Walsh and Watterson, 1988] (Figure 9). In the case of rupture downward, as the fault ruptures into the low stress region of the aseismic zone, this pattern changes such that the 60° dip has the largest average displacement followed by the 30° and 45° dips. The fact that the order does not change as the fault grows from the high stress lower layer into the low stress upper layer of the seismogenic zone when rupturing upward suggests that the change in the pattern of average displacement is not simply a function of moving into a low stress environment but may also be affected by the magnitude of that change. Note that all the displacements increase dramatically as the fault ruptures through the aseismic zone.

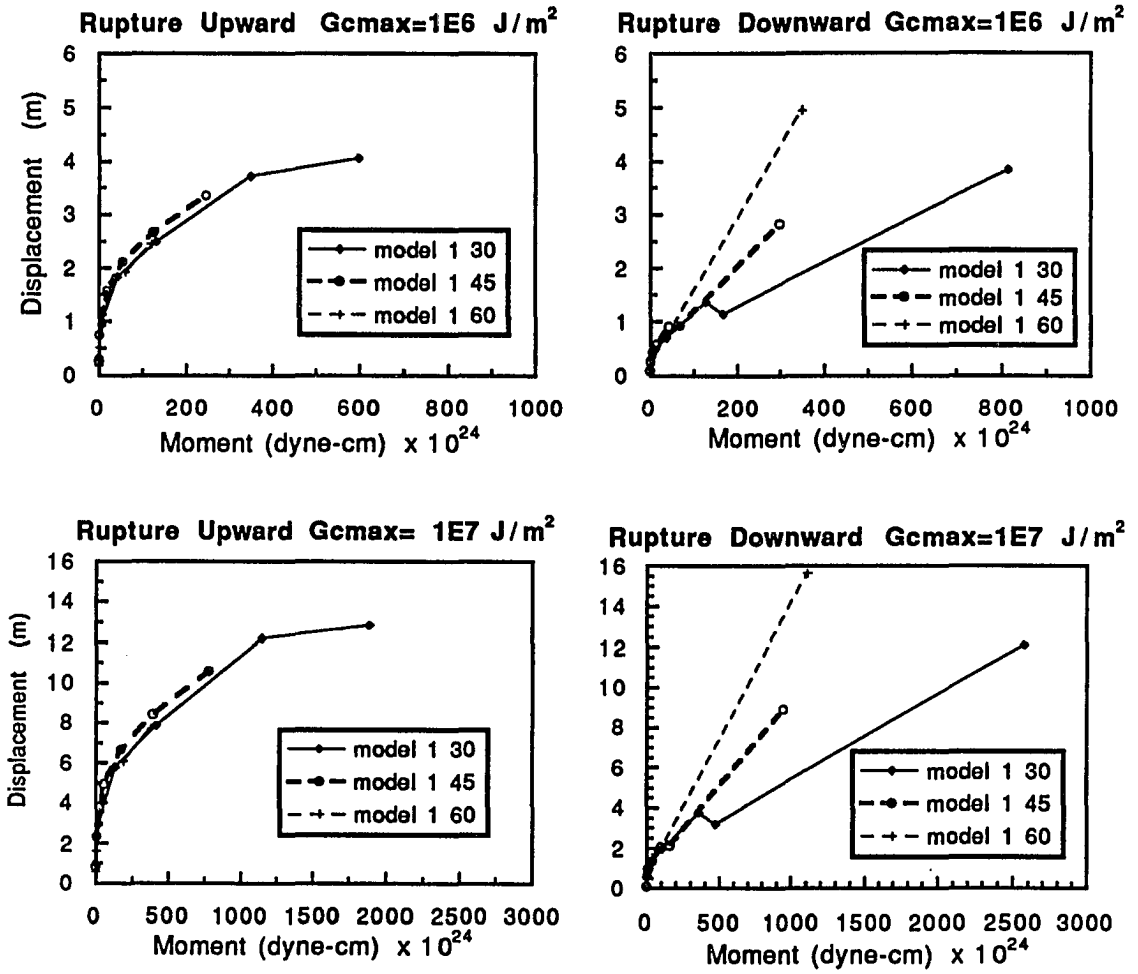

Figure 9: Average displacement as a function of seismic moment for models with varied dip angle. Moment is calculated by assuming a circular fault plane and μ=3.0 x 10^{10} Pa. (a) Average displacement decreases with increasing fault dip for rupture upward with a large increase in average displacement once the fault has grown half way through the seismogenic zone. The higher G_c value results in larger displacements. (b) The average displacement decreases with increasing fault dip for rupture downward as well, although as the fault grows into the aseismic zone the average displacement is greatest for the 60° dipping fault. Again a large increase in average displacement occurs once the fault has grown half way through the seismogenic zone, although the largest increase occurs when the fault has completely cut the seismogenic zone. The average displacement for all models decreases as the fault grows into the lower crustal layer but the displacement at any point on the fault does not. The decrease in average displacement is most prominent for the 30° fault as it grows into the lower layer.

The average displacement curves show much variability for the three crustal models (Figure 10). For faults growing downward, the average displacement is initially the smallest in the high stress diabase layer of Model 2 and lower in Models 1 and 3 where the fault initiates in a lower stress granite layer. As the fault grows downward into the lower stress layer in Model 2 and then into the aseismic zone the average displacement increases dramatically. Once the fault reaches the lower stress diabase layer within the seismic zone it surpasses the average displacements for faults in Models 1 and 3. Models 1 and 3 have similar average displacements for the initial stages of fault growth downward. Model 1 shows a jump in average displacement at node 5 as the fault tip moves to the boundary between the low and high stress granite and higher stress diabase. When the fault tip in Model 1 lies at the boundary between the granite and diabase, it is affected by the higher stress in the diabase and the average displacement increases. But once the fault moves into the higher stress region, the average displacement decreases because more stress is needed to continue fault growth.

Rupture upward in Model 2 has the largest average displacement at all stages of fault growth for all three crustal models. The fault begins in a low stress layer then grows into a higher stress layer and experiences a definitive drop in average displacement at that boundary. The behavior of the fault in Models 1 and 3 is somewhat complicated. Model 3 begins in a lower stress layer than Model 1 and has more initial displacement. In Model 1, as the fault grows toward the surface and enters the lower stress region, the average displacement increases beyond that calculated for Model 3. Again, we see the increase in average displacement as the fault moves into a lower stress region. However, at the surface, the average displacement in Model 3 surpasses that in Model 1 possibly because the total strain in Model 3 is greater.

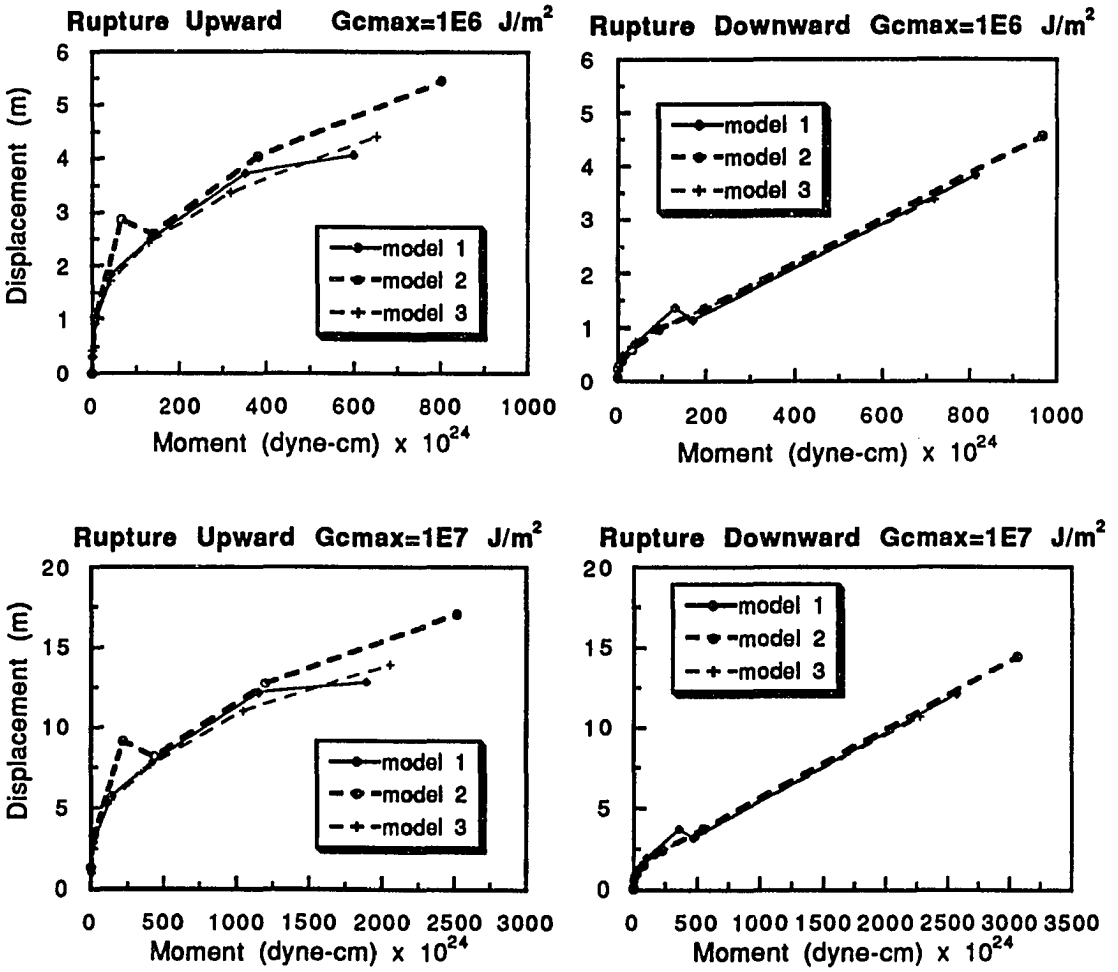

Figure 10: Average displacement as a function of seismic moment for the three crustal models. Moment is calculated by assuming a circular fault plane and μ=3.0 x 10^{10} Pa. The higher G_C value results in larger displacements. (a) Average displacement increases with increasing initial strain for fault rupturing upward. Average displacement increases more rapidly once the fault has grown half way through the seismogenic zone, although the largest increase occurs when the fault has completely cut the seismogenic zone. The average displacement for Model 2 decreases as the fault grows from a lower stress region into a higher stress region. (b) Rupture downward results in a jump in the average displacement in Model 1 as the fault grows from a lower stress region into a higher stress region. The jump in average displacement is only observed when the contrast in material properties is large.

The moment and average displacement calculated for all models have two dominant characteristics: (1) until the fault has cut at least half of the seismic zone, the average displacement and moment are small, and (2) large increases in the average displacement and moment occur at the point the fault ruptures the entire seismic zone. Because the average displacements are relatively small (less than a few meters) on these developing faults, very little topography is developed at the surface and even less deformation is required at depth to accommodate the strain accumulated at the fault tip. Furthermore, large displacements along the fault do not occur until the fault has cut the entire seismogenic zone.

We have chosen our initial state of stress such that the vertical and horizontal components of the gravitational stress are equal. Including a linearly increasing pore fluid pressure in the formulation of the problem, commonly calculated as a function of overburden pressure, results in a relative change in the shear fracture energy between individual material layers but no change in the gradient. At a material boundary, a relative change in G_c could occur due to the change in density across the boundary. Taking the ratio of the densities between layers 1 and 2 for Model 1, we find that G_c decreases by 7.2% at the boundary. As G_c scales with τ^2, this results in a 2.67% decrease in the required shear stress. The decrease in the required shear stress for Model 2 is the same as Model 1 because they have the same density structure; however, Model 3 would be unchanged because it has a uniform density in the seismogenic zone. The decrease in required stress is small enough that the rupture stability of our models would be unchanged.

DISCUSSION

Our results show that it is easier to initiate a fault at the surface where the overburden pressure and strength of rocks is generally lowest and a fault can grow under conditions with less total strain. Rupture downward in models with the lower G_C gradient is always unstable. Because rupture downward is seldom observed in nature, and the unstable rupture of a fault from near the surface to the base of the seismogenic zone suggested by our models is even more rare, the lower gradient may not be realistic for crustal models. But, faults that initiate at the surface in a model with a high G_C gradient will grow by stages which would result in several smaller events ($M_O = 1 \times 10^{23}$ to 1×10^{25} dyne-cm) to develop the fault. Large events would occur only in cases where the faults initiate at depth, either on a new fault or by re-rupturing an existing fault that extends to the surface, a result also obtained by Das and Scholz [1983].

Our results indicate that faults initiating at the base of the seismogenic zone are always unstable and would always result in large earthquakes ($M_O = 1 \times 10^{27}$ dyne-cm). Although large earthquakes generally initiate at the base of the seismogenic zone, they almost always occur on pre-existing faults. This observation, combined with the result that greater strain is required to initiate at depth, suggests that this is probably not a mechanism for establishing a new fault. However, from these results and equation (3) we can conclude that any planar fault initiating within the seismogenic zone would rupture unstably upward and, depending on the crustal model and shear fracture energy gradient, may rupture either stably or unstably downward, as well. From equation (3) we know that as the initial fault length and R_p increase, fault growth can occur at a lower shear stress. Thus, re-rupturing an old fault will generally be easier than forming a whole new fault. We have not examined the role of non-planar surfaces nor faults with major bends or intersecting fault planes which may allow a fault to rupture from near the base of the

seismogenic zone to a point below the surface. Although complicated fault configurations may enhance stable rupture, the faults would still require higher strains to initiate at depth.

Identifying specific cases of new fault growth is difficult because (1) the smaller events expected on a new fault are more difficult to monitor and locate and (2) documenting that the events occurred on a new fault (with little offset or exposure) requires detailed field investigation or may not be in evidence at all. The 1968 Meckering Australia event is a possible example of rupture on a new or developing fault. The M_S=6.8 earthquake was a moderate size intraplate event with a very shallow source depth. The event was located in the Archean shield within the South West Seismic Zone and was accompanied by large scale thrust faulting over a 200 km area [Vogfjord and Langston, 1987]. The largest fault was the Meckering fault, which prior to this event was not shown on any structural maps of the region. However, mapping by Gordon and Lewis [1980] provided evidence of a pre-existing fault. They found iron-stained breccia on the fault and noted a correlation between the fault trace and frequent quartz scatter or iron-rich soils. Faulting is not exposed in the bedrock and there have been no other historical moderate or large scale earthquakes in the region of this fault. Vogfjord and Langston [1987] used body wave inversion techniques and finite fault modeling to determine that the majority of the seismic energy results from an event that ruptured a planar fault initiating at a depth of 1 km and propagated downward to 6 km. Analysis of the foreshocks and aftershocks by Langston [1987] confirms this pattern of rupture; both foreshocks and aftershocks cluster near 1 km depth and the deepest aftershock occurs at 7 km depth.

Vogfjord and Langston [1987] and Langston [1987] conclude that the depth of faulting in this shield area is confined to the near surface because most of the crust is too strong to be fractured. Based on strength curves of Meissner and Strehlau [1982], they propose that the brittle-ductile transition occurs at great depth and generating sufficient

shear stress in the transition zone to cause earthquake rupture at that depth would be extremely difficult. Thus, the Meckering event may be an example of a fault growing and developing in a region in which the available stress is not capable of full rupture through the crust. The long recurrence interval of this and other intraplate events has led Scholz et al., [1986] to suggest that healing of the fault will occur between events, which may facilitate rupture initiation at the surface over long periods until the fault is well established. However, the observation that rupture propagated downward rather than upward, supports the idea of fault initiation and growth suggested by our results.

Marone and Scholz [1988] studied the earthquake depth distribution along well developed and poorly developed faults and found that for poorly developed faults with little net slip, such as the Meckering event, there is no upper level cut off for shallow seismicity. Their observations suggest that shallow seismicity may be controlled by the presence of gouge on the fault. Poorly developed faults with little net slip and no appreciable gouge zone undergo seismic failure throughout the upper region of the seismic zone. In general, the poorly developed faults have shallower depths of faulting overall with the maximum depth at less than 10 km, which supports the idea that the faults with shallow seismicity are young faults which are growing at depth.

Miller and Furlong [1988] studied the depth of faulting on the San Andreas Fault system in northern and central California. They suggested that seismicity is controlled by the maximum level of shear stress on the faults rather than any rheological consideration. In central California, the San Andreas Fault is a well developed plate boundary which extends from the surface through the brittle crust. In contrast, the San Andreas Fault in northern California is less well developed and does not accommodate all plate motion [Furlong et al., 1989]. Seismicity occurs on several new faults to the east of the San Andreas in northern California and the overall maximum depth and the depth of the peak

seismicity are 3 km shallower than on the well developed San Andreas Fault to the south. Miller and Furlong [1988] conclude that the maximum shear stress on the faults in northern California is not sufficient to rupture the entire seismogenic zone. As the stress in the region increases and becomes more concentrated on fault plane asperities, one would predict the depth of faulting would increase. Thus, we suggest that fault growth occurs as a gradual process with initiation at the surface. As stress builds in the region, the ability to rupture the crust at greater depths increases.

Patterns of foreshocks and aftershocks may hold important clues to the process of fault nucleation. Foreshocks, although generally difficult to identify, rarely if ever nucleate below the depth of the main shock. Aftershocks frequently occur at depths below the main shock. This pattern suggests a need for initial rupturing at shallow depths through smaller events which open the fault zone. Rupturing the shallow and presumably weaker portions of the fault creates a longer initial fault capable of concentrating greater stress at depth to rupture the stronger portions of the fault. The occurrence of aftershocks below the main shock has been proposed as a mechanism of extension of the fault in a downward direction through small adjustments after displacements associated with the main shock redistribute stress concentrations at depth.

CONCLUSIONS

Initiation and propagation of a planar fault from the base of the seismogenic zone to the surface requires greater strain and results in larger earthquakes than rupture downward, independent of dip angle or crustal model. Once a fault initiates at depth, rupture would always progress to the surface without the need for increased regional strain. However, initiation of a fault at the surface and growth downward requires less total strain and can occur in a stable manner. To develop a fault which grows from the surface completely through the seismic zone would require increasing the level of strain at various stages of fault growth depending on the fault dip and crustal model. For an appropriate shear fracture energy, fault growth occurs in stages, developing at shallow depths through small earthquakes with little displacement. The moment and average displacement calculated for all fault models have two dominant characteristics: (1) the average displacement and moment are small until the fault has cut at least half of the seismic zone and (2) large increases in the average displacement and moment occur once the fault has cut the entire seismogenic zone. Additionally, growth of a fault into a region of significantly lower stress results in a large increase in average displacement and vice versa, growth of a fault into a higher stress region results in a decrease in average displacement at the boundary layer. We suggest that initial development of faults in a stable cratonic region is a result of nucleation at the surface and rupture downward. Re-rupturing of an established fault may initiate at the surface or at depth depending on the degree of fault healing between events and the tectonic stress available.

CHAPTER 3

RUPTURE OF A DIP-SLIP FAULT IN A TECTONICALLY ACTIVE REGION: A STUDY OF THE LOMA PRIETA EARTHQUAKE

The seismicity in California during the decade of the 1980's was both surprising and contrary to conventional "seismic wisdom" and has initiated a wholesale re-evaluation of the basic premises of seismic hazard assessment and fault behavior. In California, there were 12 significant earthquakes in the 1980's. Only one of the earthquakes occurred on or near the San Andreas Fault, even though seismic hazard maps for California indicate that the San Andreas poses the greatest hazard [Working Group of California Seismic Hazard Assessment, 1988, 1990]. The October 19, 1989 Loma Prieta earthquake is perhaps the most unusual of the California events [See Special Issue on Loma Prieta, Bull. Seis. Soc. Am., 81, 1991].

The hypocenter of the M_S =7.1 earthquake was located southwest of the San Andreas Fault trace in the Santa Cruz Mountains (Figure 11). Aftershocks outline a fault area roughly 40 km long, centered on the epicenter. The northern segment of the fault rupture is coincident with a segment of the San Andreas which last ruptured during the great 1906 San Francisco earthquake. The southern extent of the fault rupture overlaps with the creeping segment of the San Andreas. Considerable controversy exists over the nature of the Loma Prieta Fault. The rupture characteristics of the earthquake simply do not agree well with the expected character of an earthquake on the San Andreas Fault. Rupture initiated at 18 km depth, nearly twice as deep as the average hypocentral depth on the San Andreas [Wald et al., 1991]. The fault plane for the Loma Prieta event dips approximately 65° W, not the 90° expected for the San Andreas. The slip of the Loma Prieta event was

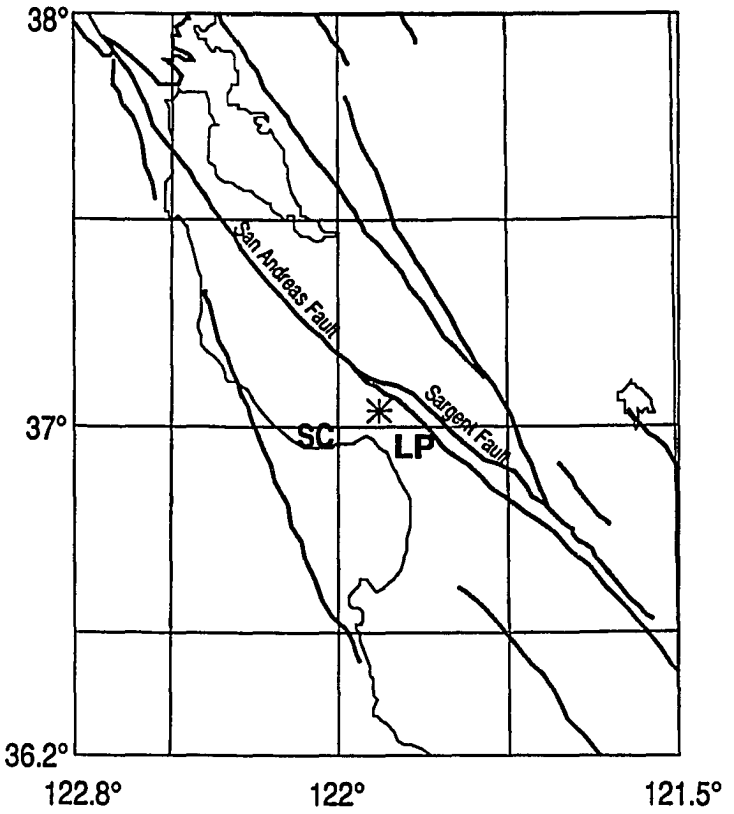

Figure 11: Location map of the Loma Prieta Earthquake. The asterisk marked LP is the location of the epicenter. SC denotes the city of Santa Cruz, California. Bold lines are locations of major faults in Northern California.

oblique strike-slip, divided into nearly equal components of right-lateral strike slip and reverse motion [Wallace et al., 1991]. Further, the rupture appears to have propagated from 18 km depth and abruptly terminated at 8-5 km depth [Wald et al., 1991]. The San Andreas Fault is exposed in the Santa Cruz Mountains, but apparently did not have surface rupture during the event. Anderson [1990] proposed that the high topography present in the Santa Cruz region is a result of repeated slip along a high angle reverse fault, which implies that the 1989 event must be a relatively common occurrence. The character of the event strongly suggests that the rupture did not occur on the San Andreas Fault and that the Loma Prieta Fault is a separate entity from the San Andreas Fault.

The fact that the Loma Prieta rupture stopped well below the surface is at odds with our understanding of rupture mechanisms and raises important questions about seismic hazard assessment for the area. Is the seismic hazard of the Loma Prieta region now low, or is the San Andreas Fault now ready to fail? We need to understand the rupture process to address questions about seismic hazard. If the earthquake occurred on the San Andreas Fault, why did rupture stop below the surface? If the earthquake occurred on a separate fault, what is the relationship between the rupture plane and the San Andreas Fault? In Chapter 2, I showed that, in a stable cratonic region a fault initiates at the surface and propagates downward by a process in which incremental increases in the regional stress generate rupture events. By contrast, a fault that preferentially nucleated at the base of the seismogenic zone would always rupture to the surface in a large earthquake. So the question becomes: What stopped the rupture of the Loma Prieta Fault? The answer lies in our understanding of the role of the elastic rock properties and fault interactions on the process of fault rupture.

Several of the other significant earthquakes occurring in California during the 1980's also initiated at depth and stopped before rupturing the surface, e.g. the 1983

Coalinga, 1985 Kettleman Hills, and 1987 Whittier Narrows events. All occurred as blind thrusts initiating at depth at a major decollement [Eberhardt-Phillips, 1989; Stein and Yeats, 1989]. Fault rupture in the Coalinga event terminates at the intersection of two faults and thus supports a model in which fault interaction dominates the rupture process.

To place constraints on parameters affecting fault rupture, we evaluated a suite of models in which the role of crustal rheology and fault interaction were investigated. Using linear elastic fracture mechanics and the finite element method, we modeled rupture of the Loma Prieta Fault. Shear fracture energy, a measure of rock strength, was varied, as was the depth of the boundary between the upper and lower crustal rocks, to constrain the role of crustal rheology on rupture stability. Similarly, the effect of the interaction of displacement and stress fields of adjacent faults on rupture of the Loma Prieta Fault was also investigated.

Fracture Mechanics Model

Earthquake rupture can be described as a two step process: (1) the formation of the crack, and (2) the propagation, or growth of the crack through repeated sudden slip events. An enormous body of literature on criteria for crack growth exists, most of it rooted in experimental work. As described in Chapter 2, laboratory and field studies suggest that shear failure corresponding to an earthquake rupture results from rapid growth and linking of microscopic fractures, tensile or shear, to form macroscopic zones of shear [McGarr et al., 1979; Segall and Pollard, 1983; Petit and Barquins, 1988]. With modifications of the method outlined in Chapter 2, the oblique strike-slip and thrust motion of the Loma Prieta Fault is modeled as a combination of Mode II and Mode III crack displacement in an elastic body. The crack has an initial length of $2a_0$ and dips at an angle, ß to the principal

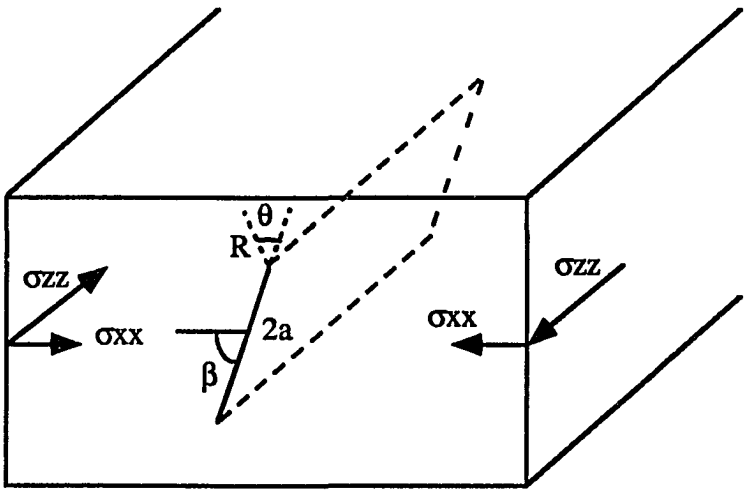

Figure 12: Model of buried crack in an elastic body and associated boundary conditions. Crack of length 2a in a body under compressive stress in the x- and z- directions. The crack dips at an angle ß to σ_{xx}. Stress in the region of the fault tip is calculated at a distance R and an angle Θ to the plane of the crack.

horizontal stress, σ_{xx} (Figure 12). Using linear elastic fracture mechanics, the near-field approximation of the shear stress parallel to the fault at the crack tip is

$$\tau_{xy} = \frac{K_{II}}{\sqrt{2\pi R}} \left\{ \cos\left(\frac{\Theta}{2}\right) \left[1 - \sin\left(\frac{\Theta}{2}\right) \sin\left(\frac{3\Theta}{2}\right) \right] \right\} \tag{1}$$

for Mode II failure and

$$\tau_{zy} = \frac{K_{III}}{\sqrt{2\pi R}} \left\{ \cos\left(\frac{\Theta}{2}\right) \right\} \tag{2}$$

for Mode III failure. K_{II} and K_{III} are the Mode II and Mode III stress intensity factors, respectively. Θ is the angle between the fault plane and a point of known shear stress at a distance R in front of the crack tip, measured positive in the counterclockwise direction [Lawn and Wilshaw, 1975]. The stress intensity factor is a function of crack geometry and boundary conditions on the crack and on the body and can include the effects of friction or material layering. Solutions for K_{II} and K_{III} can be found in general reference books [see Paris and Sih, 1965; Tada, Paris and Irwin, 1973; Lawn and Wilshaw, 1975; and Rooke and Cartwright, 1976].

Unstable crack propagation leading to fault rupture occurs when G, the shear fracture energy, reaches a critical value G_C. G is related to K_{II} by

$$G = \frac{(1 - \nu^2)}{E} K^2_{II} + \frac{(1+\nu)}{E} K^2_{III} \tag{3}$$

where ν is Poisson's ratio and E is Young's modulus. Combining equations (1) - (3), and setting $G = G_C$ and $R = R_p$ gives:

$$G_c = \frac{(1 - \nu^2)}{E} \frac{\tau^2_{xy}\, 2\Pi R_p}{\cos\frac{\Theta}{2}\left\{1 - \sin\left(\frac{\Theta}{2}\right)\sin\left(\frac{3\Theta}{2}\right)\right\}} + \frac{(1+\nu)}{E} \frac{\tau^2_{zy}\, 2\pi R_p}{\left(\cos\left(\frac{\Theta}{2}\right)\right)^2} \quad (4)$$

From equation (4) we can determine the stress at the edge of the process zone required to propagate the fracture. However, as noted in Chapter 2, the critical shear fracture energy G_c, required for crack growth in the crust is poorly constrained. In our experiments to explore the features controlling the rupture of the Loma Prieta Fault, we use two different G_c curves (Figure 13). Based on the results of fault rupture discussed in Chapter 2, we restricted the maximum G_c value to 1 x 10^6 J/m^2; however, we varied the depth of the maximum value. We constrain the shear fracture energy at the surface to be 1 x 10^5 J/m^2 then increase the value linearly with depth to a maximum value of 1 x 10^6 J/m^2. At depths below the maximum value, G_c decreases rapidly to 1 x 10^5 J/m^2 to reflect the low shear strength of the aseismic crust. The material properties include the effects of a uniform number and distribution of cracks and defects in the process zone in front of the crack tip. The magnitude of G_c is only important for calculations of absolute values of shear stress necessary for failure. The stability of fault growth indicated by the results of our modeling is relatively independent of the magnitude chosen for G_c but not the gradient.

The seismic moment associated with the fault growth is calculated as

$$M_0 = \mu D A \quad (5)$$

where μ, the shear modulus is 3 x 10^{10} Pa, D is the average displacement on the fault, and A is the area of the fault. For the calculation of the moment, the fault is assumed to be circular with a radius of a_0, the half-length of the fault. In addition to the requirement that $G = G_c$ for crack growth, the displacement at any point on the fault must remain constant

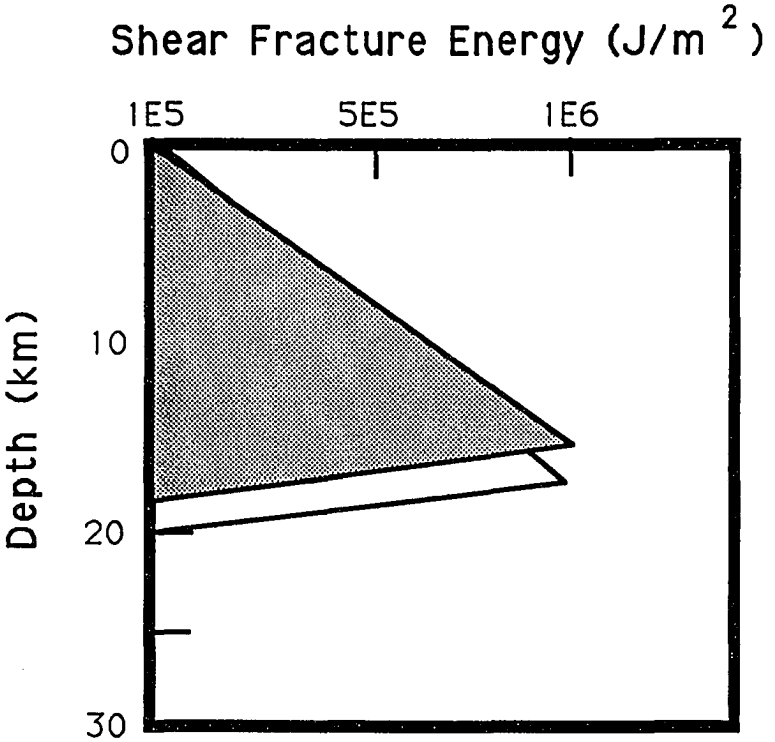

Figure 13: Shear fracture energy as a function of depth. The shaded area highlights the Gc curve with a peak value at 16 km depth. The solid black line is the Gc curve with a peak value at 18 km depth. Shear fracture energy represents the energy required to initiate crack growth. The curves chosen represent two possible members of a suite of curves and are constrained by calculations of G_c from earthquake events.

or increase at every step of fault growth. Although the average displacement along the entire length of the fault may decrease as the fault grows, the displacement at any point on the fault must remain constant or increase, i.e., the model does not allow a fault to "overshoot" in displacement then readjust, as it grows.

Mechanical Model

The finite element model has 3216 nodes and 3010 quadrilateral elements (Figure 14). Faults initiate along the dipping boundaries of the triangular shape elements in the center of the grid. The length of the grid is 187 km, the depth is 40 km, and the thickness is infinite. To accommodate the out-of-plane strike slip motion of the rupture, we use a finite element formulation which allows strain in three dimensions but assumes that $\sigma_{zz} = 0$. The formulation assumes that the fault is infinitely long and that the strain in the z-direction is uniform. In our model, a layered elastic lithosphere is subjected to uniform, far-field horizontal displacement boundary conditions in the x- and z-directions (Figure 12). The grid is free to move horizontally along its base but is fixed in the vertical direction. We assume that the vertical and horizontal gravitational stresses in the crust are equal to the lithostatic stress [McGarr, 1988]. Elastic moduli for the various models evaluated are listed in Table 2. The shear stresses, τ_{xy} and τ_{zy} are calculated at the edge of the process zone, a distance R_p from the fault tip. We calculate the crack tip stresses in a multi-step process. From the finite element calculation, we know the components of shear stress stress at the centroid of all the elements in the grid. For the elements within a 90° arc in front of the crack tip, we then perform a simple transformation of axis and calculate the shear stress parallel to the plane of the crack at the centroid of the elements. These values of shear stress are interpolated to the edge of the process zone and averaged to get the shear stress at

the crack tip. The interpolation function incorporates the rapid increase in shear stress as R approaches zero [Sneddon and Lowengrub, 1969; Lawn and Wilshaw, 1975].

All models include a seismogenic zone from 0-20 km depth and an aseismic mantle layer with reduced stiffness and shear modulus between 20 and 40 km. The rheology of our initial grid, Model 1, represents an average crust with a granitic rheology from 0-8 km overlying a stronger, diabase rheology from 8-20 km depth to be consistent with crustal models for the San Andreas region [Mooney and Walter, 1982]. The strength of the upper mantle is significantly reduced to correspond with the crustal heating associated with the removal of the subducted slab from beneath the North American plate [Furlong et al., 1989]. Furlong and Langston [1990] propose that the restraining bend in the San Andreas has resulted in a discrepancy in the displacement direction between the crust and mantle in this region. This differential displacement caused in a decoupling of the lower crust from the mantle and played a key role in rupture initiation at depth.

We model a fault as a slippery node [Melosh and Williams, 1989], which is a node in the finite element model with an extra degree of freedom and allows differential slip across the node and element boundary. The node is represented as a free surface with no resolved shear stress and is allowed to slip in a specified direction [Melosh and Williams, 1989]. Presently, a slippery node does not account for friction along the fault surface. In light of the present understanding that stress and therefore friction along a fault plane are relatively low [Kanamori, 1980; Zoback et al., 1987], this appears to be an acceptable simplification in the model. A constant value of friction along the fault would result in a higher far-field stress to initiate rupture in our model but the relative behavior would not change. The increase in the frictional/fracture strength with depth is taken into account by the linearly increasing G_c value with depth.

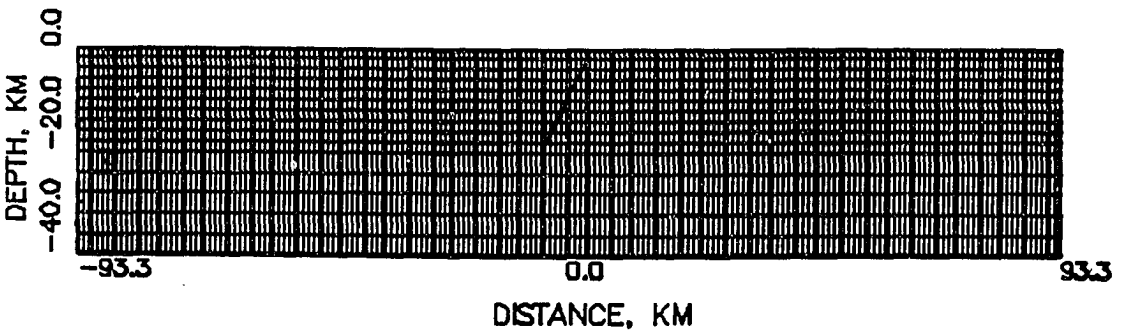

Figure 14: Finite element grid for models of fault rupture. The dipping plane is the Loma Prieta Fault. Uniform horizontal displacements are applied in both the x- and z-directions until the energy at the crack tip reaches the critical energy for crack growth. The base of the grid is fixed in the vertical direction but free to move in the horizontal directions.

TABLE 2: Elastic Moduli for Lithospheric Models of the Loma Prieta Fault

Model	E_2/E_1	Depth (km)	Young's Modulus, E (Pa)	Poisson's Ratio, ν
Model 1				
G_{cmax} at 16 km	5.88	0.0	1.7×10^{10}	0.25
		8.0	1.0×10^{11}	0.27
		20.0	6.0×10^{10}	0.35
G_{cmax} at 18 km	12.2	0.0	7.8×10^{9}	0.25
		8.0	1.0×10^{11}	0.27
		20.0	6.0×10^{10}	0.35
Layer at 6 km	10.0	0.0	1.0×10^{10}	0.25
		6.0	1.0×10^{11}	0.27
		20.0	6.0×10^{10}	0.35
Layer at 8 km	5.88	0.0	1.7×10^{10}	0.25
		8.0	1.0×10^{11}	0.27
		20.0	6.0×10^{10}	0.35
Layer at 10 km	6.10	0.0	1.65×10^{10}	0.25
		10.0	1.0×10^{11}	0.27
		20.0	6.0×10^{10}	0.35
Model 2	5.88	0.0	$1.7? \times 10^{10}$	0.25
		8.0	1.0×10^{11}	0.27
Shallow fault and Loma Prieta Fault		20.0	6.0×10^{10}	0.35
Model 3	5.88	0.0	1.7×10^{10}	0.25
		8.0	1.0×10^{11}	0.27
SAF slip 10-20 km		20.0	6.0×10^{10}	0.35
SAF slip 8-20 km	6.24	0.0	1.6×10^{10}	0.25
		8.0	1.0×10^{11}	0.27
		20.0	6.0×10^{10}	0.35
SAF slip 4-20 km	6.24	0.0	1.6×10^{10}	0.25
		8.0	1.0×10^{11}	0.27
		20.0	6.0×10^{10}	0.35

SAF = San Andreas Fault

All faults initiate at the base of the seismogenic zone at 20 km depth. Each fault initiates as a crack 1 km long in the x-y plane and infinitely long in the z-direction. The fault grows by increasing the stress in the grid to reach failure when necessary. The model contains one slippery node representing the initial fault. Equal horizontal displacements are applied in the x- and z-directions at the boundaries until the shear fracture energy at the fault tip node is sufficient to cause growth. Once the node has reached the critical shear fracture energy for growth, we assume the fault is capable of rupturing to the next node in the fault plane. Then, that node is changed to a slippery node and the process continues until the fault has grown through the seismic zone.

RESULTS

We investigated the ability of a simple rheologic boundary between the upper and lower crust to stop fault rupture between 8 and 5 km depth. Using the fault configuration in Model 1 (Figure 15), we determined the magnitude of the contrast in Young's modulus between the two layers required to stop fault rupture. Our initial model placed the material boundary at 8 km depth and used a G_c curve with the maximum value at 16 km depth. In this model, the ratio of the Young's modulus in the upper layer to that in the lower layer, E_2/E_1 must be equal to 5.88 to stop crack rupture in the upper crustal layer. The effect of the depth of the peak in the shear fracture energy curve on rupture stability was tested by changing the maximum from 16 km to 18 km depth. With the shear fracture energy maximum at 18 km depth, the ratio E_2/E_1, must be equal to 12.82 to stop crack rupture.

In both of the above models, fault growth is stable from initiation at 20 km depth to the depth of the maximum value of shear fracture energy (Figure 16). Incremental increases in fault length require comparable increases in the displacement applied at the boundaries to generate the required shear stress. If sufficient displacement is applied to continue crack growth past the depth of the maximum value in the G_c curve, the crack propagation is unstable as the crack grows into the upper crustal layer. In these models, fault rupture stops in the upper crustal layer, at 6 km depth, regardless of the G_c curve. For a G_c peak at 18 km depth, the required displacement is 34.86 m and the shear stress is 7.2 MPa while for the peak at 16 km depth the displacement is 18.14 m and the shear stress is 8.4 MPa. The difference in the displacement and shear stress required for crack propagation in the two models is a direct function of crack length. From equations (1) and (4), we know that the shear stress required for crack growth decreases as function of crack length thus, the longer the initial fault the lower the shear stress required for rupture. The

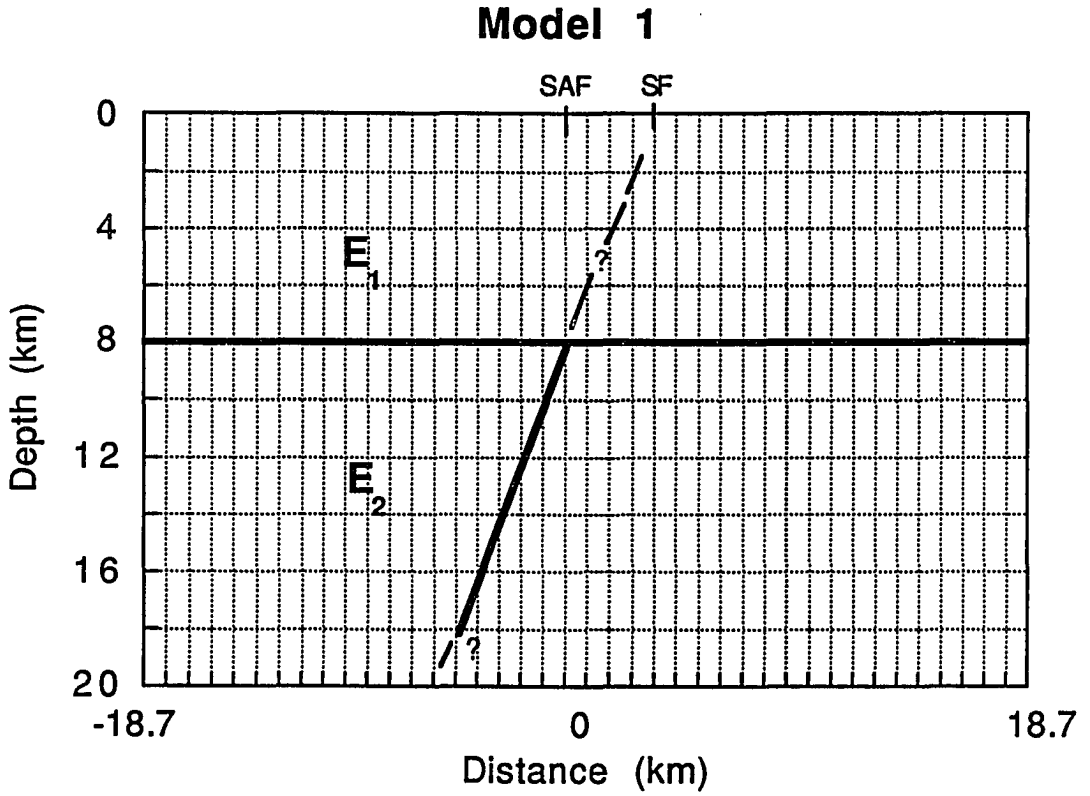

Figure 15: Finite element grid for Model 1 for different G_c curves. Heavy lines indicate the Loma Prieta Fault. The depth of the boundary between the upper and lower crustal layers is shown at 8 km although models with a boundary at 6 and 10 km were also evaluated.

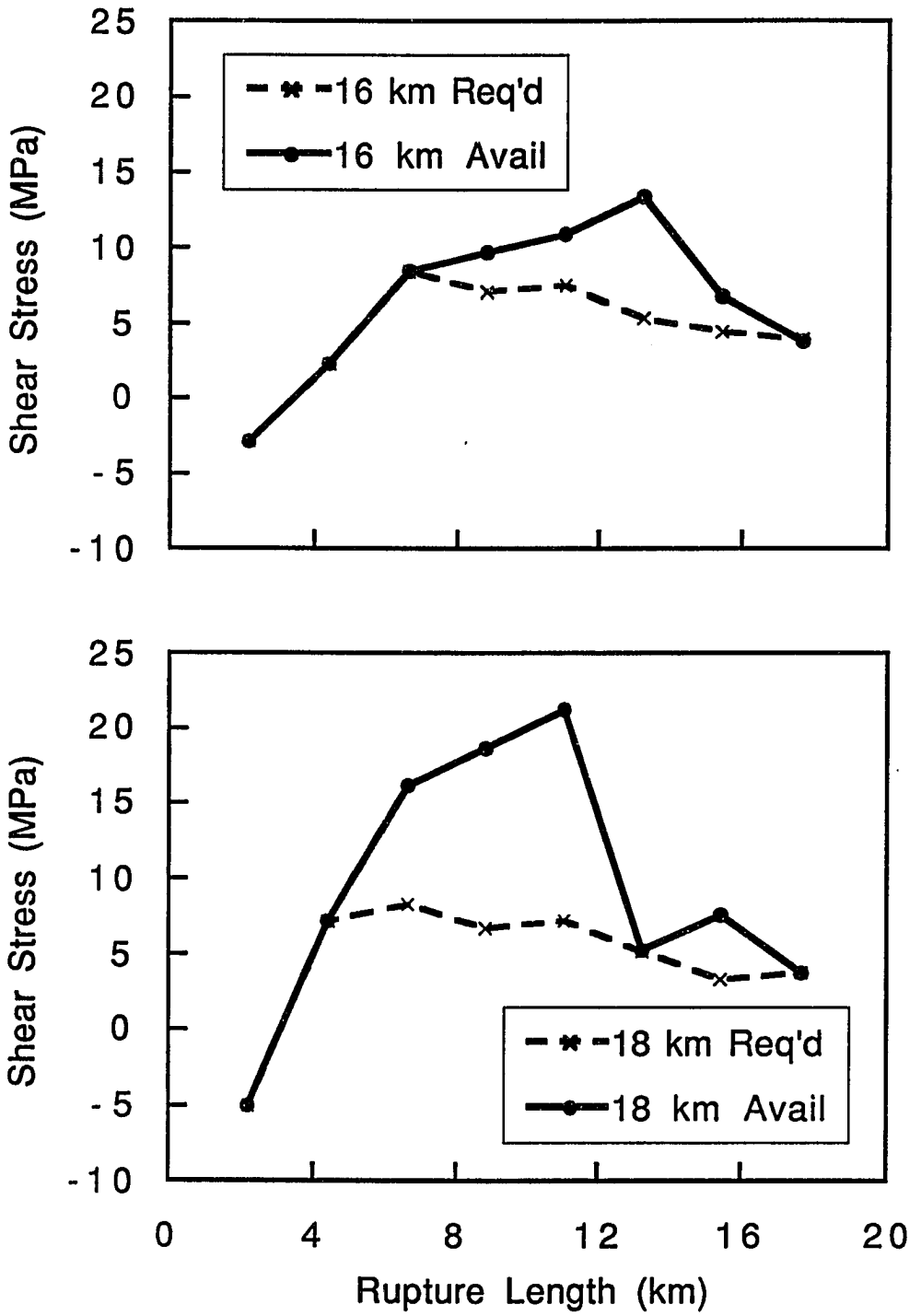

Figure 16: Shear stress as a function of rupture length of the fault for Model 1 with different G_c curves. Where the required and available shear stress curves coincide, continued propagation of the fault requires additional displacement.

difference in initial strain or displacement required to propagate the fault to the upper crustal layer results in greater available stress in the upper crustal layer and difficulty in stopping rupture. The steeper slope of the G_c curve for the case of the peak at 16 km has only a minor effect on the results.

To evaluate the success of these models, we compared the predicted displacements to the geodetically measured coseismic elevation change [Marshall et al., 1991]. The predicted surface displacements for both of the finite element models are nearly symmetric about the mid-point of the Loma Prieta Fault plane and shifted westward from the coseismic displacements modeled by Marshall et al. [1991] (Figure 17). For the model with a G_c maximum at 18 km depth, the predicted coseismic uplift is 1.78 m, approximately 3 times larger than the observed 0.55 m; the full amplitude (peak to trough) of displacement is 2.17 m, again, more than 3 times larger than observed. A model with a G_c maximum at 16 km predicts an elevation change of 0.85 m which is larger than the observed but much less than that of the model with the G_c maximum value at 18 km. Models with shallower Gc maximums, i.e. at 14 km or less, result in lower surface elevation changes but conflict with the seismological data which indicates rupture started at depths of 16-18 km.

Fault plane displacements determined using strong ground motion and teleseismic data [Wald et al., 1991] provide another constraint on the model (Figure 18). Several workers [Beroza, 1991; Steidl et al., 1991; Wald et al., 1991] have suggested that fault displacement was greater to the north than to the south of the epicenter. The average displacement is 3.94 m for the model with a G_c maximum at 18 km, more than twice the value calculated by Wald et al. [1991]. The average displacement associated with a G_c maximum at 16 km, 1.94 m, corresponds well with the average slip of 1.81 and 2.48 m calculated by Wald et al., [1991] for the northwest and southeast segments of the fault.

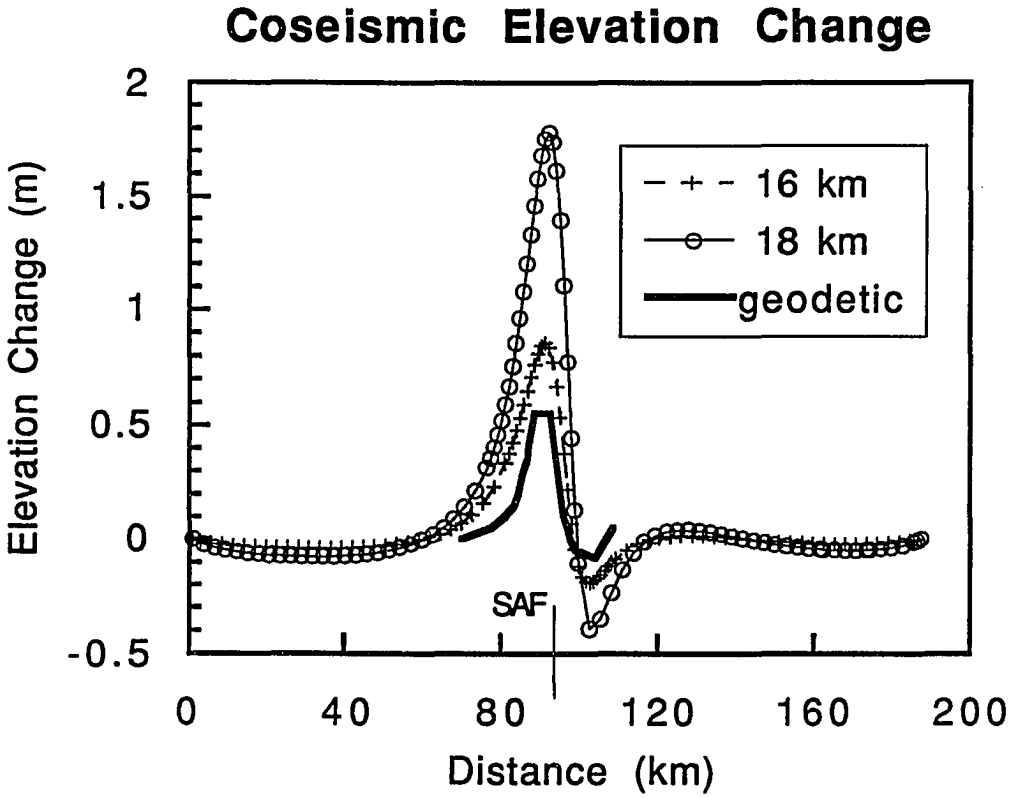

Figure 17: Coseismic elevation change for Model 1 with different G_c curves. The elevation change predicted by the model with a G_c maximum at 16 km agrees well with the observed displacement from Marshall et al., [1991]. Predicted displacements for the model with a G_c maximum at 18 km are more than 3 times than observed displacements.

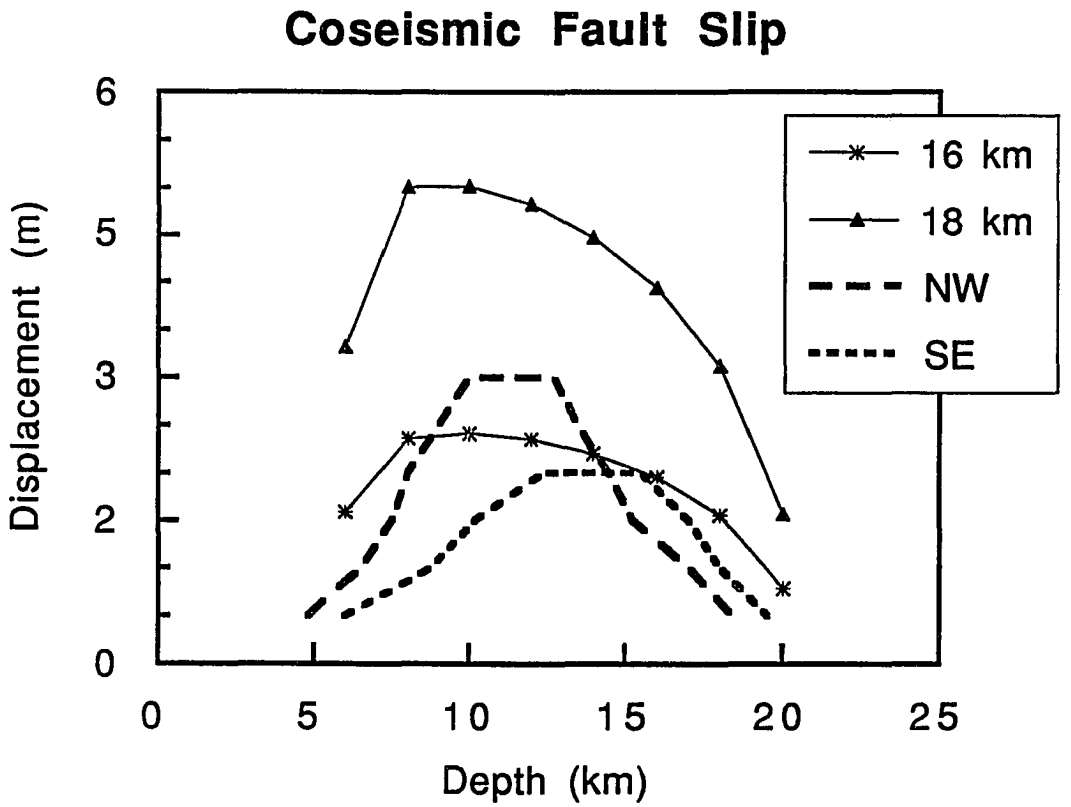

Figure 18: Oblique slip displacement for Model 1 with different G_c curves. Heavy bold lines indicate the predicted slip displacements of Wald et al., [1991] for the northwest, NW, and southeast, SE, segments of the fault plane. The fault slip as a function of depth for the model with a G_c maximum at 18 km depth predicts displacements more than twice the values calculated by Wald et al., [1991] with models of the strong ground motion and teleseimic data. A good agreement between the average predicted displacement and the average displacements calculated by Wald et al. [1991] is achieved with a maximum in the G_c curve at 16 km.

The predicted displacements for the model with the G_c maximum at 16 km are greater at both the upper and lower tips of the fault. Our method does not incorporate the effects of individual asperities on a fault plane, thus we can only calculate average displacements for the fault plane. We calculated a moment for these models assuming an area of 400 km^2 and $\mu = 3.0 \times 10^{10}$ Pa. Using an average displacement of 1.94 m and 3.98 m for the models with a maximum value of G_c at 16 and 18 km, we calculated a moment of 2.34×10^{26} dyne-cm and 4.73×10^{26} respectively, as compared to a moment of 2.4×10^{26} dyne-cm from a joint inversion of the surface and body waves [Wallace et al., 1991].

The poor correlation of the results for the model with a G_c maximum at 18 km are a result of the larger displacements required to initiate unstable rupture and the corresponding excess in available stress once unstable rupture commences. For all subsequent analyses, we use a G_c curve with a maximum value at 16 km depth. This G_c curve corresponds to the E_2/E_1 ratio of 5.88 which is in good agreement with the ratio E_2/E_1 equal to 5.0 used by Marshall et al. [1991] in dislocation models of the geodetic data. An E_2/E_1 ratio equal to 12.82 for the model with G_c maximum at 18 km depth is quite large and unreasonable for a geologic crustal model.

We varied the depth of the upper crustal layer boundary from the initial depth of 8 km used above, to 6 and 10 km, to evaluate the effect on rupture stability. In a model with the layer boundary at 6 km depth, we were able to stop the rupture with an E_2/E_1 ratio equal to 10.0 (Figure 15). The very low stress required to stop rupture in the upper crustal layer is difficult to obtain with a simple and geologically reasonable rheological contrast. For a layer boundary at 10 km, only a minor change in the E_1/E_2 ratio from 5.88 to 6.1 is required to stop fault rupture. The shear stress required for fault rupture in these three models is 10.8, 8.4, and 6.8 MPa for the 10, 8 and 6 km layer boundaries, respectively (Figure 19). Displacements required for rupture are 23.23, 18.13, and 14.65 m,

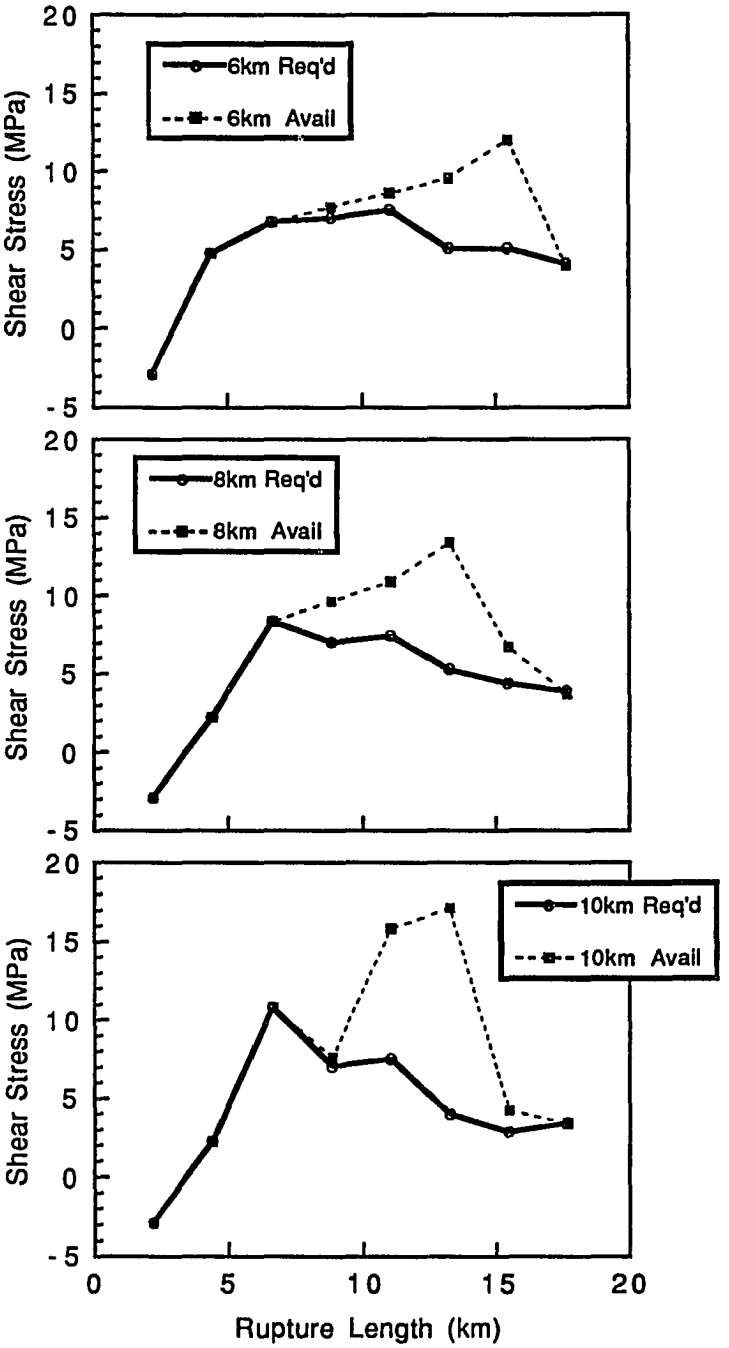

Figure 19: Shear stress as a function of rupture length of the fault for Model 1 with different boundary layer depths. Where the required and available shear stress coincide, additional displacement is required to continue rupture of the fault. In all three cases, the rupture is stable up to the maximum G_c value at 16 km depth (rupture length = 6.62 km) then becomes unstable to a depth of 6 km (rupture length = 15.45 km).

respectively. As the weak upper crustal layer thins and the average compliance of the crust decreases, it is easier to initiate rupture of the fault.

A comparison of the coseismic elevation change for all three models indicates there are only small differences (Figure 20). A boundary layer at 10 km results in a slightly larger uplift on the hanging wall and a smaller depression of the footwall of the fault, while a boundary layer at 6 km results in the opposite response. The boundary at 8 km depth falls between these two models. Fault slip at depth for the three models is quite similar (Figure 21). A layer boundary at 6 km results in the smallest average fault slip and an abrupt stop in slip displacement at 6 km depth. A boundary at 8 km or 10 km predicts a smooth decline in displacement at the shallow end of the fault. We chose a boundary at 8 km depth to best represent the observed displacements based on geodetic and strong ground motion studies although a boundary layer at 10 km is also acceptable. All subsequent models use a G_c curve with a maximum value at 16 km depth and a boundary layer at 8 km depth.

Using the fault configuration in Model 2 (Figure 22), we evaluated the effect of a free-slipping shallow surface fault on rupture stability. We included a short fault from 0-2 km updip of the Loma Prieta Fault plane. Rupture of the Loma Prieta Fault is easily stopped in the upper crustal layer with an E_2/E_1 ratio equal to 5.88 and can be stopped with a ratio as low as 5.7. A comparison of the shear stress available in Model 1 and 2 with the same rheology indicates that the shallow fault has little effect on the initial required stress. However, the presence of the shallow fault does relieve stress at the surface and allow fault rupture to stop more easily (Figure 23). The displacement required for rupture is 18.44 m compared to the 18.13 m required for Model 1.

The significance of this small stress reduction can be important in a tectonically and seismically active region such as California. If a sufficient number of faults are slipping

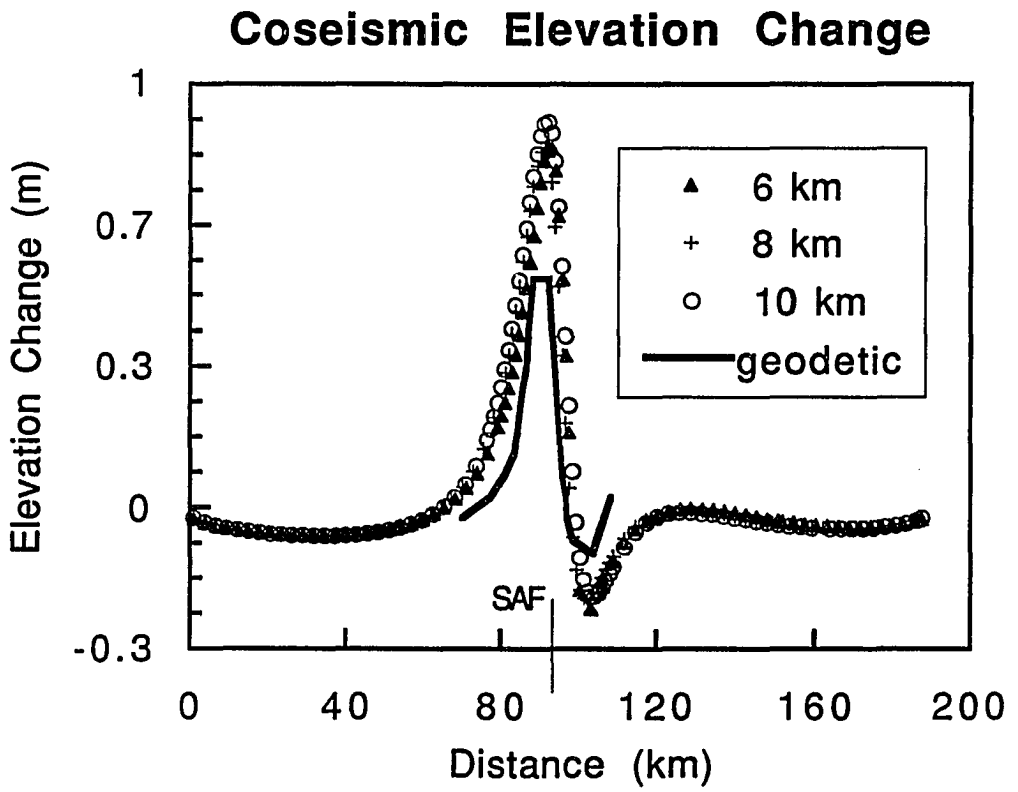

Figure 20: Coseismic elevation change for Model 1 with different boundary layer depths. Only small differences are obvious between the three models with layer depths at 6, 8 and 10 km. All predict surface elevation changes greater than the observed.

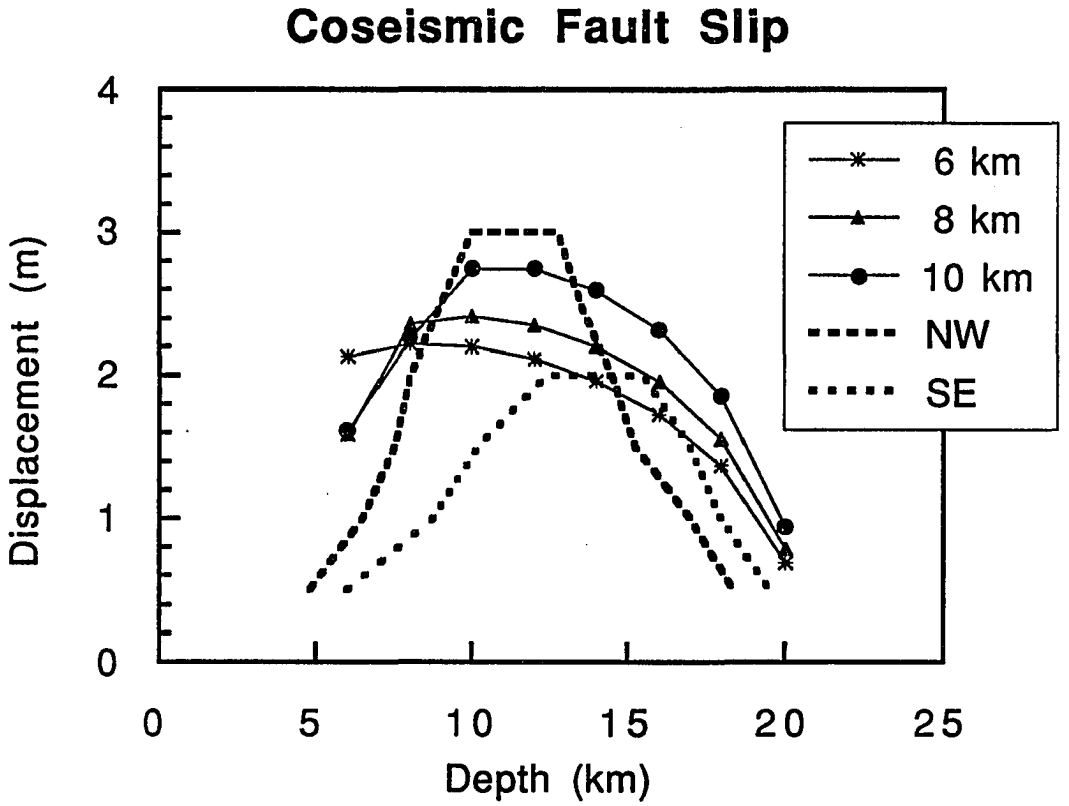

Figure 21: Oblique slip displacement for Model 1 with different boundary layer depths. Heavy bold lines indicate the predicted slip displacements of Wald et al., [1991] for the northwest, NW, and southeast, SE, segments of the fault plane. The average displacement for all three cases agrees well with the average displacement of Wald et al. [1991]. The model with a layer boundary at 6 km results in a large displacement at 6 km depth which does not correspond well with the model of Wald et al [1991].

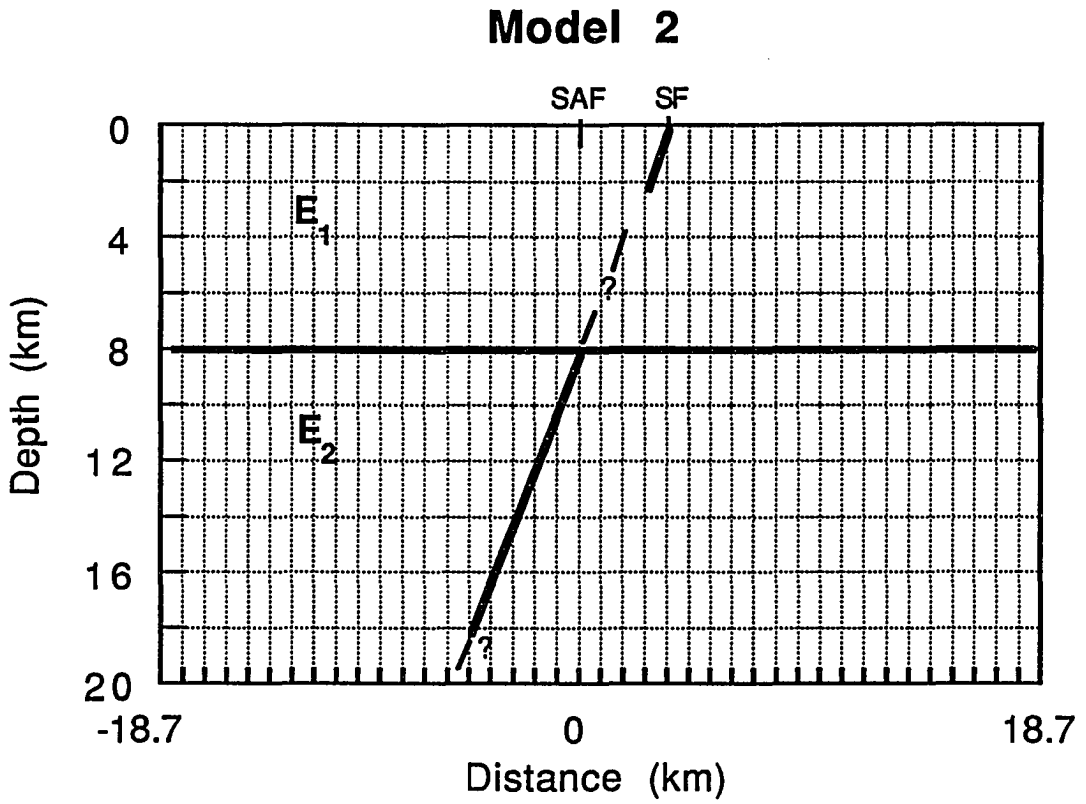

Figure 22: Finite element grid for Model 2 with a shallow fault. Heavy lines represent the Loma Prieta Fault plane at depth and a shallow dipping fault at the surface.

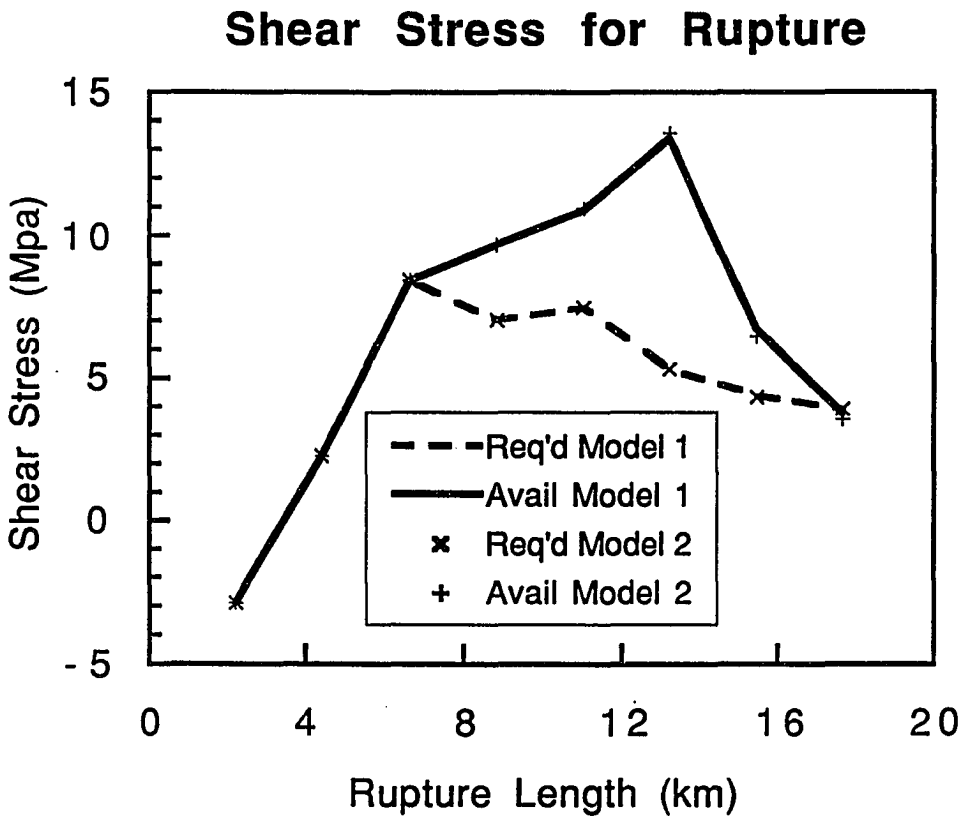

Figure 23: Shear stress as a function of rupture length of the fault for Model 2 with a shallow fault. A comparison of the shear stress required and available for Model 1 without the surface fault and Model 2 with a shallow dipping fault indicates very little difference in the initial stresses in the system. However, at a depth of 6 km, Model 2 requires less stress, less displacement and a smaller contrast in the Young's modulus between the upper and lower crustal layers.

and adjusting for changes in regional stress, it is possible to significantly reduce the effective Young's modulus of a material [See Chapter 4; Wallace and Melosh, in prep]. This allows the use of low Young's modulus values for crustal rocks with much larger experimentally measured values for intact rock specimens. This result also suggests that prior slip on one or more shallow faults in the region could have generated a slip 'credit', effectively reducing the stress in the upper crust and stopping rupture of the Loma Prieta Fault.

The coseismic elevation change associated with Models 1 and 2 differ in minor details not detectable in the geodetic data and models available. In Figure 24, the presence of the shallow fault slipping concurrently with the Loma Prieta Fault is evident in small anomalies on both the upthrown and downthrown sides of the fault and slightly higher amplitude of total surface displacement. Predicted fault slip for Model 2 is more than 1.3 m of total displacement at the surface, a result not substantiated by field investigations or the strong ground motion studies (Figure 25). Thus, coseismic slip on a shallow fault is not supported by the observations. Nevertheless, a situation in which slip on adjacent faults has occurred prior to rupture of the Loma Prieta event is capable of reducing the stress in the upper crust and helping to stop the Loma Prieta rupture before it reached the surface.

A final series of tests were evaluated using Model 3 (Figure 26) in which the San Andreas Fault is allowed to slip freely at various depths in the crust. The depth of the unlocked section was varied to evaluate the effect on rupture stability. Models in which the San Andreas slipped at depths of 10-20 km, i.e. below the intersection of the two faults, resulted in an increase in displacement on the Loma Prieta Fault and an increase in the displacement required for rupture, but did not affect the ability to stop fault rupture in the upper crust. In the case where the tip of the slipping San Andreas and Loma Prieta faults intersect at 8 km, the Loma Prieta Fault will rupture unstably to the surface as the stress

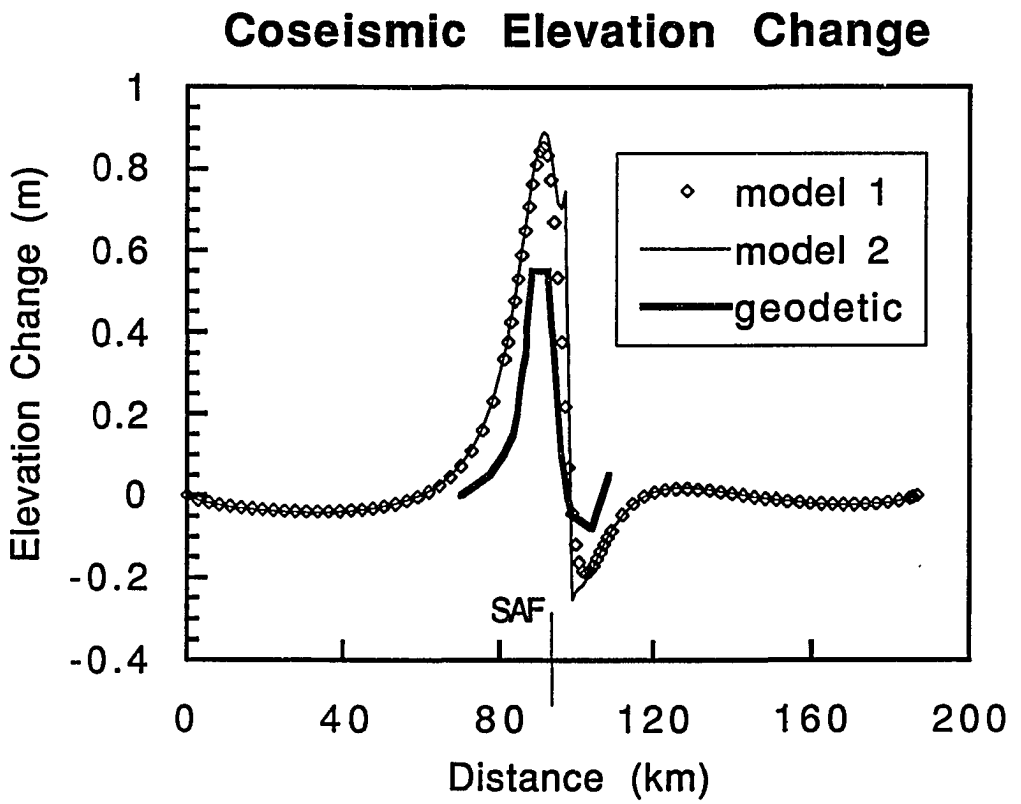

Figure 24: Coseismic elevation change for Model 2 with shallow fault. A small anomaly in the displacement is predicted in the area of the shallow fault. The anomaly is too small to detect and varify with the geodetic data available. Otherwise the predicted displacements for Model 1 and Model 2 are very similar.

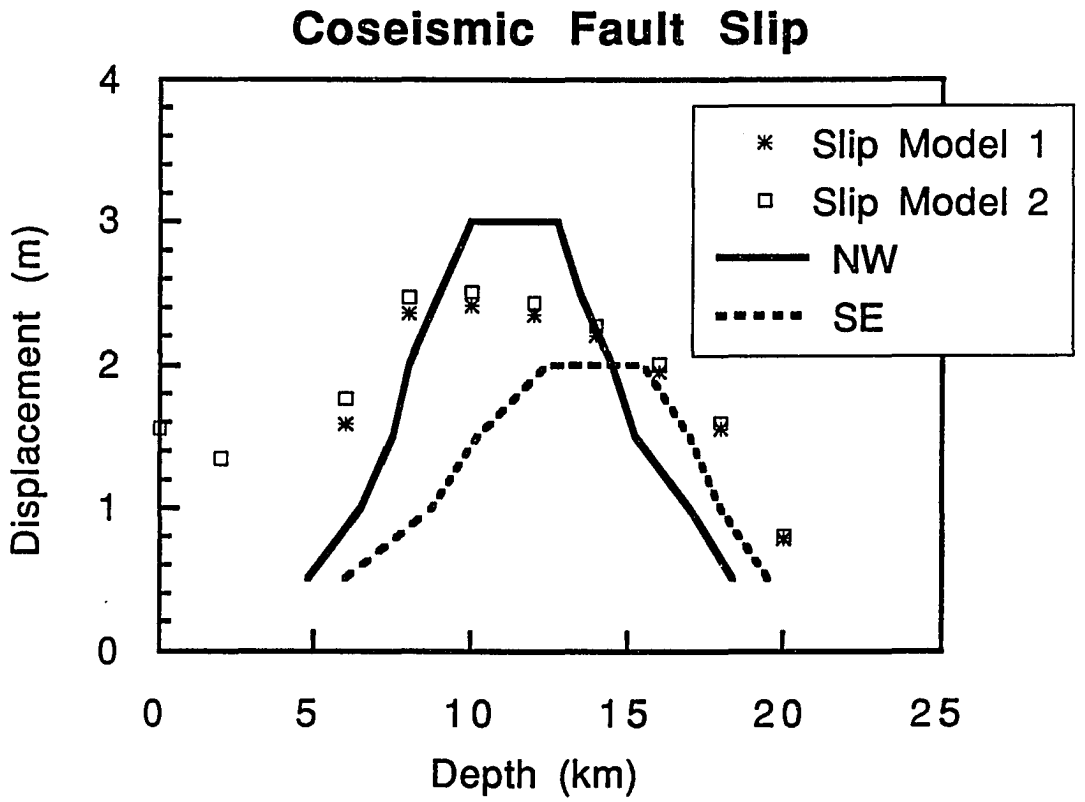

Figure 25: Oblique slip displacement for Model 2 with a shallow fault. Heavy bold lines indicate the predicted slip displacements of Wald et al., [1991] for the northwest, NW, and southeast, SE, segments of the fault plane. The presence of the shallow fault is apparent in the very shallow displacements predicted for this model. At depth there is little difference in the predicted displacements for Model 1 and 2 and both agree well with the displacements modeled with strong ground motion data [Wald et al., 1991].

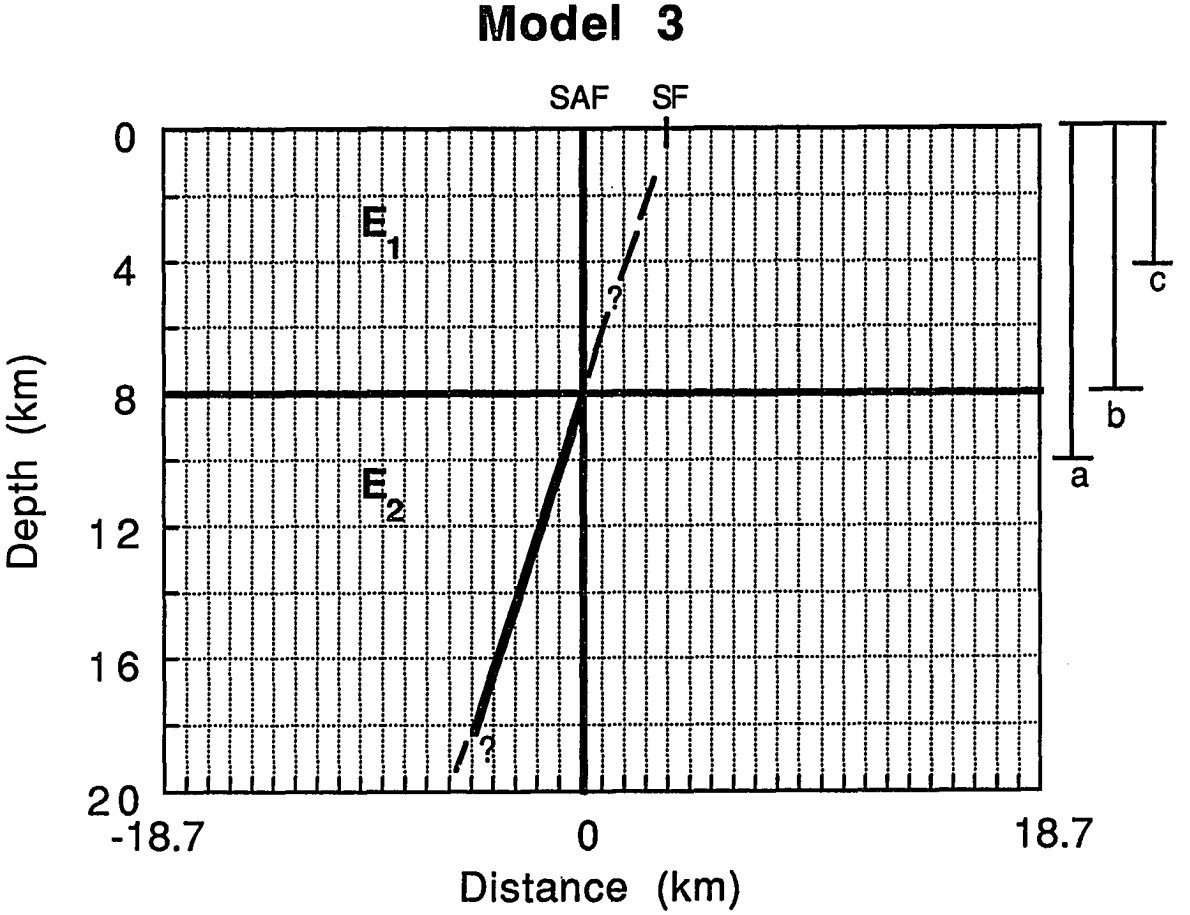

Figure 26: Finite element grid for Model 3 indicating depths over which the San Andreas Fault is locked. Grid shows only the central portion of figure 14. *a*, *b*, and *c* identify the depth range over which the San Andreas Fault was locked in three different models. For a model *a*, the Loma Prieta Fault ruptured unstably from 16 km to 6 km and required a ratio of $E_2/E_1 = 5.8$. Models *b* and *c* required a slightly higher $E_2/E_1 = 6.1$ to stop rupture at 6 km depth. The free-slipping San Andreas Fault caused the Loma Prieta Fault to have increasing displacements as more of the San Andreas Fault was allowed to slip.

concentration generated at the tip of the two faults is large enough to allow the crack to propagate. A change in the E_2/E_1 ratio from 5.88 to 6.1 will stop the rupture in the upper crustal layer. For this case, we also investigated the possibility of the Loma Prieta Fault changing dip orientation and propagating in the plane of the vertical San Andreas Fault once the two fault planes intersect. We found that rupture on the San Andreas Fault above 8 km requires larger displacements and is more difficult to achieve than continuing rupture on the Loma Prieta Fault at the same depth. In our models, the San Andreas Fault is not assigned any unusual elastic properties which might influence the rupture of the Loma Prieta Fault. If this assumption is valid, we can conclude that the Loma Prieta Fault is not an extension of the San Andreas Fault because there is no evidence for slip on the San Andreas Fault in conjunction with the Loma Prieta event. In a final test, the San Andreas Fault is locked from 0-4 km depth only and slips freely from 4-20 km. The displacements on both the San Andreas and Loma Prieta faults are the largest for any case and rupture initiation requires the greatest displacement, however, with $E_2/E_1 = 6.1$, rupture still stops at 6 km depth. All of these models investigate the role of a fault slipping at depth and stress relief at depth. The fault slip at depth has little effect on the Loma Prieta Fault rupture stability. In contrast, a fault slipping at the surface has the ability to relieve stress and stabilize rupture at the surface.

CONCLUSIONS

This analysis demonstrates that the primary factor controlling the depth of rupture on the Loma Prieta Fault is low stress in the upper crust. How this stress state is developed is not known. The low stress condition can be modeled by either choosing the material properties such that a large contrast in Young's modulus exists between the two layers of the crust, or by including numerous slipping faults in the upper crust. Although the latter case was not fully explored in this analysis, we can draw on the conclusions of Chapter 4 where the role of faults on the effective Young's modulus is thoroughly explored. In Chapter 4, it is demonstrated that the presence of faults cutting a thick elastic plate can reduce the effective Young's modulus by a factor of three. Certainly California is an active tectonic region cut by numerous faults slipping and weakening the upper crust. A model which included only one such fault reduced the tectonic stress and enhanced the ability for rupture to stop even though slip was occurring directly updip of the Loma Prieta Fault.

Questions about the seismic hazard potential of the San Andreas Fault can now be addressed. If we assume that the San Andreas Fault is of comparable mechanical strength to the Loma Prieta Fault, the rupture of the San Andreas requires greater displacement than rupture of the Loma Prieta Fault. If however, we assume that the San Andreas Fault is less compliant in the upper crust than the Loma Prieta Fault, rupture would have continued on the San Andreas Fault. We have no evidence that rupture occurred on the San Andreas at any depth nor do we have evidence that the material around the San Andreas Fault is mechanically stronger than the material around the Loma Prieta Fault. Thus, the most likely case is that the strength of the San Andreas Fault is equal to or less than the strength of the Loma Prieta Fault, which implies that the Loma Prieta Fault has a higher seismic hazard than the San Andreas Fault.

CHAPTER 4

BUCKLING OF A FAULTED LITHOSPHERE

In recent decades, a number of interesting geologic problems have been modeled using a continuous elastic plate. For example, elastic plate theory has been used to model the flexure due to the load of an island chain [Walcott, 1970], bending and buckling of the lithosphere [Hanks, 1971; Lambeck, 1983; McAdoo and Sandwell, 1985], and flexure and subsidence of foreland basins [Jordan, 1981]. Although the use of continuous elastic plates has been very successful for modeling many geologic observations, our understanding of the mechanics of the deformation is limited by the assumption that the elastic plate is homogeneous and isotropic. In the rigorous theory of plate tectonics, the lithospheric plates are idealized as internally rigid and continuous. Among other deviations from this ideal, the lithosphere is cut by numerous faults on many scales and the applicability of solutions for continuous materials is arguable.

Of fundamental importance in plate deformation, and the focus of this study, is the effect of faults on the elastic properties and the buckling response of a lithospheric plate. Faults in the lithosphere are ubiquitous at all scales, from the presence of dislocation planes in a single crystal to the scale of major plate boundary faults such as the San Andreas Fault. Yet, until recently, it has not been possible to include a fault in models of lithospheric deformation. We have incorporated two techniques in the finite element code, TECTON (v. 1.5), which allow us to investigate the buckling of a faulted plate. We use the method of Melosh and Williams [1989] and model a fault as an internal free surface with no (or a specified) resolved shear stress on its plane. Faults of any slip orientation and length can be included in the model with this technique. TECTON also includes a large-deformation

formulation that updates the positions of the grid nodes as deformation progresses. This procedure allows for a more accurate calculation of displacement within an element but most importantly, it is a fundamental requirement for accurate representation of buckling of the plate.

Buckling of an elastic plate occurs when it is subjected to a sufficiently large in-plane force. Previous studies of buckling have introduced only a single fault, and used approximate methods. Most commonly, the effect of faults on the mechanics of buckling is ignored [Chapple and Forsythe, 1979]. One possible approach is to use an effective elastic thickness which is equal to the unfaulted thickness of the plate to adjust for stress relief by fault slip. This model assumes that the fault relieves all stress and strength in the faulted layer. Similarly, a reduced Young's modulus could be used to reflect a reduction in plate stiffness by the presence of the fault. However, it is unclear whether these analytical solutions can accurately represent the change in buckling stress and wavelength caused by a fault.

Regions cut by large crustal-scale faults can be modeled as a completely broken plate. The lithosphere is modeled as a plate restrained at one end and loaded vertically and/or horizontally on the free end representing the fault [Walcott, 1970; Zandt and Owens, 1980; Angevine and Flanagan, 1987]. Using this approach, it is possible to calculate the shear stress and moment across the free end necessary to model the flexure of a region. Hall and Chase [1989] used a simple algorithm to linearly adjust the amount of moment and vertical shear stress transmitted across a fault in a plate and modify the degree of plate continuity to simulate a partially broken plate. While these techniques give reasonable results for flexural models and begin to address the mechanics of a broken plate, further improvements are needed.

In this Chapter, we investigate the general mechanical behavior of a pervasively faulted elastic plate. We specifically study the effects of fault depth, spacing and dip on the effective Young's modulus and the buckling wavelength for an elastic lithosphere of finite thickness. We will demonstrate that solutions to the buckling equation using thin plate theory and an effective elastic thickness for a faulted plate do not accurately account for changes in the buckling response due to the faults.

Finite Element Method Applied to Buckling

Linearized stability theory indicates that as an idealized, infinitely thin elastic plate approaches the buckling instability, the amplitude of deformation is unbounded. We tested the ability of our finite element code to correctly predict this sharp increase in amplitude and found that a very large, but finite, increase in amplitude occurs at the point of buckling. This is a more reasonable result for real geologic problems with finite plate thicknesses that include finite-amplitude effects, than the infinite amplitudes predicted by linear instability theory. In our model, we assume the plate has an initial topographic deflection, ω_o, described by

$$\omega_o = a_o \sin kx \tag{1}$$

where a_o is the initial amplitude of topography and k, the wave number, is $2\pi/\lambda$. The equation for buckling of an initially deflected plate [after Turcotte and Schubert, 1983], subjected to a horizontal force per unit width, N, and a hydrostatic restoring force, $\rho g h$ is

$$D\frac{d^4\omega_1}{dx^4} + N\frac{d^2}{dx^2}(\omega_1 + \omega_0) + \rho g \omega_1 = 0 \tag{2}$$

where ω_1 is the additional deflection caused by buckling. D, the flexural rigidity, is $Eh^3/12(1-\nu^2)$, where E is Young's modulus, h is the elastic thickness of the plate and ν is Poisson's ratio. Assuming the final deflection will be of the form

$$\omega_1 = a \sin kx \tag{3}$$

we can substitute (1) and (3) into (2) and solve for the amplitude of the final deflection, a. The ratio of the final amplitude to the initial amplitude gives the amplitude of deflection due to buckling, a/a_o, where

$$\frac{a}{a_o} = \frac{Nk^2}{Dk^4 - Nk^2 + \rho g} \tag{4}$$

Buckling occurs when the ratio a/a_o becomes unbounded at the buckling force N_b, defined by

$$N_b = Dk^2 + \frac{\rho g}{k^2} \tag{5}$$

The minimum buckling force is found by taking the derivative of (5) with respect to the wave number k. Then substituting $\sigma_b = N_b/h$ and rearranging, we can calculate the buckling stress, σ_b,

$$\sigma_b = \sqrt{\frac{E\rho gh}{3(1-\nu^2)}} \tag{6}$$

Using solutions to equations (4) and (6) for a given test model, we evaluate the ability of our numerical techniques to solve problems of buckling.

We use a two-dimensional finite element grid consisting of a homogeneous elastic layer to compare our numerical results to the analytical solutions. Parameters for all grids used in our analysis are listed in Table 3. Our initial grid, Model 1, is 1000 km long and 10 km thick with 1600 quadrilateral elements and 2005 nodes (Figure 27). We apply an initial sinusoidal deformation with a wavelength, λ_0 equal to the theoretical buckling wavelength of 200 km and an initial amplitude, a_0. A fixed displacement boundary condition is applied in the vertical direction at the bottom left and right corner nodes and Winkler forces [Winkler, 1867; Desai, 1979; Williams, 1990] are applied across the remaining basal nodes. The Winkler forces act as a spring foundation for the grid and simulate an isostatic restoring force by applying a force proportional to the vertical deflection at each node. The grid is fixed in the horizontal direction along the left side and a uniform horizontal displacement boundary condition is applied along the right side. The horizontal displacement is incrementally increased and the node locations updated until the grid buckles.

Initial tests determined the sensitivity of the numerical solutions to the grid. A grid with an element aspect ratio of 1:1, and a total length, L, greater than three times the buckling wavelength produced results that agreed well with the theory. Grid lengths much less than 3L are more rigid and buckle at a higher stress due to the cantilever boundary constraints. The addition of triangular elements, or elements with aspect ratios much greater than 1:1.25 resulted in an overestimate of buckling stress for the grid. Stresses were averaged over a column of elements covering the full depth of the grid to smooth the perturbations arising at the peaks and troughs of the topography. Fiber stresses generated by the flexure and buckling in the plate vary greatly in magnitude and sign at the peaks and troughs of the deformation. This resulted in a condition in which elements at the peaks and troughs reached the buckling stress well before the rest of the plate.

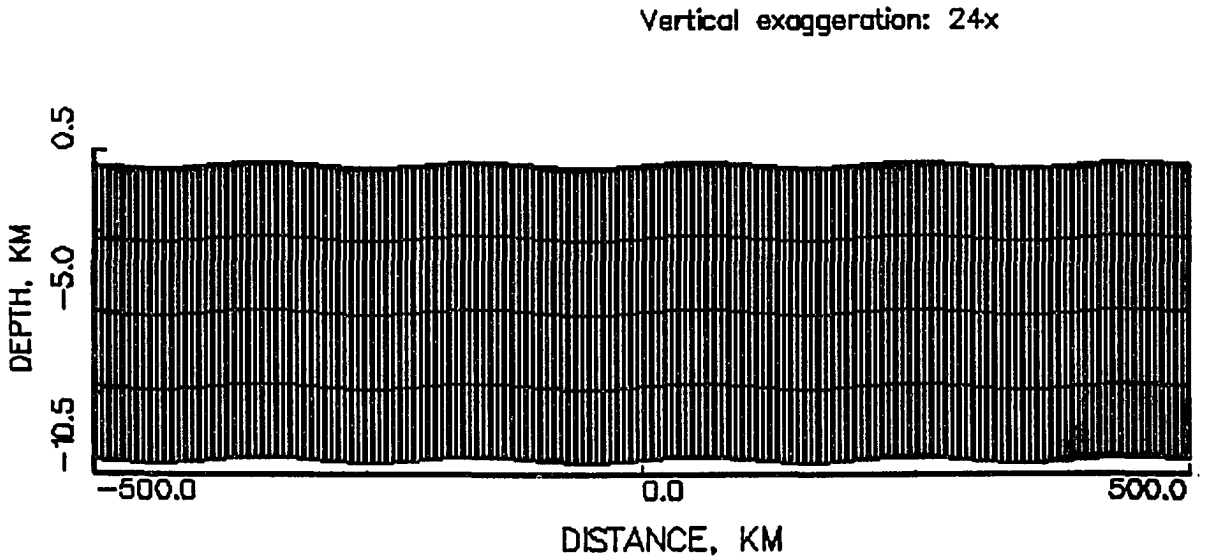

Figure 27: Finite element grid used for Model 1 and the testing of the numerical method. We apply an initial deformation with a wavelength equal to the buckling wavelength. The amplitude of the initial topography was varied to determine the value which produced the best agreement with the analytical solution.

TABLE 3: Model Parameters

Parameter	Model 1	Model 2
Young's modulus, E	3.169×10^{11} Pa	5.77×10^{10} Pa
Density, ρ	2800 kg/m^3	3300 kg/m^3
Poisson's ratio, ν	0.25	0.25
Buckling stress, σ_b	5.56×10^9 Pa	4.6077×10^9 Pa
Wavelength, λ_b	200 km	300 km
Initial amplitude, a_o	100 m	1600, 1400, 1800 m*
Length, L	1000 km	692, 1428, 2570 km*
Width, h	10 km	32 km

*Varies for fault dips of 25°, 40° and 60°.

Equation (4) predicts that, as the plate approaches the buckling instability, the ratio a/a_o is unbounded. We tested the ability of our finite element code to correctly reproduce this sharp increase in amplitude. The initial amplitude of deformation, a_o, was varied to determine the value which results in the best agreement between the theoretical and numerical amplitude-strain relationship. We calculated several numerical models using an a_o between 10 and 1000 m. The amplitude-strain relationships for the theoretical and numerical calculations show an excellent agreement up to a strain of 0.007, or at about half the buckling strain of 0.016 (Figure 28). Beyond a strain of 0.007, the curves begin to diverge. Models using a_o = 100 m or less resulted in a more accurate a/a_o ratio than the model with a_o = 1000 m. Near the buckling strain, the numerical and theoretical solutions differ by 20-70% depending on a_o. However, all but the model with a_o = 1000 m demonstrate that a_o increases rapidly at the theoretical buckling stress and all predict a reasonable a/a_o relationship at strains less than the buckling strain.

In our analysis, we noted that the stress-strain relationship is dependent on both the initial amplitude and wavelength. Using equation (6), we calculated the buckling stress, σ_b, and assuming plane strain deformation, the buckling strain, ε_{xx}, can be calculated as $(1-\nu^2)\sigma_b/E$. Based on our calculations, the best agreement between the buckling stress and strain occurs for a_o = 100 m (Figure 29). The stress-strain curve for a_o = 100 m increases linearly up to the buckling stress, then flattens immediately, maintaining a constant stress as the strain increases before ultimately decreasing. The stress-strain relationships for models with an a_o less than 100 m increase linearly, but then overshoot the theoretical buckling stress before becoming non-linear. The overshoot results from numerical error when the initial deformation is small. As with the amplitude-strain relationship, the worst agreement between the numerical and theoretical stress-strain curves occurs for a_o = 1000 m, where development of a non-linear stress-strain relationship is

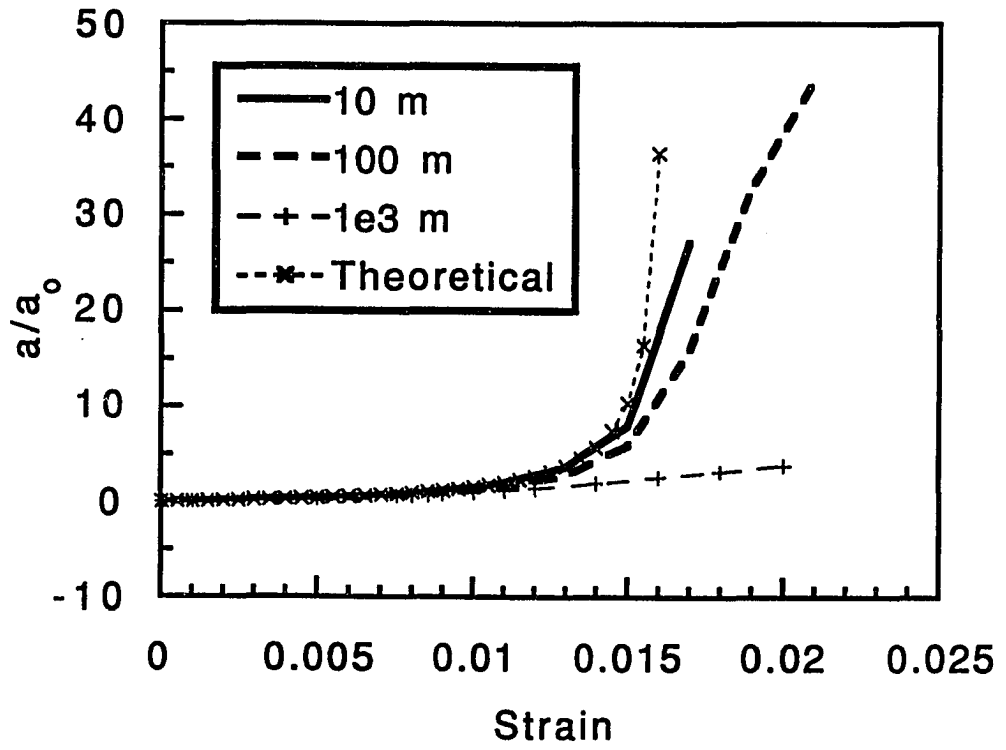

Figure 28: The amplitude-strain relationships for the theoretical and numerical calculations for different initial amplitudes of deformation, a_0. Excellent agreement occurs up to a strain of 0.007, or about half the buckling strain for all initial amplitudes. Near the buckling strain, the numerical and theoretical solutions differ by 20-70% depending on a_0. However, all but the model with a_0 = 1000m demonstrate that a_0 increases rapidly at the theoretical buckling stress.

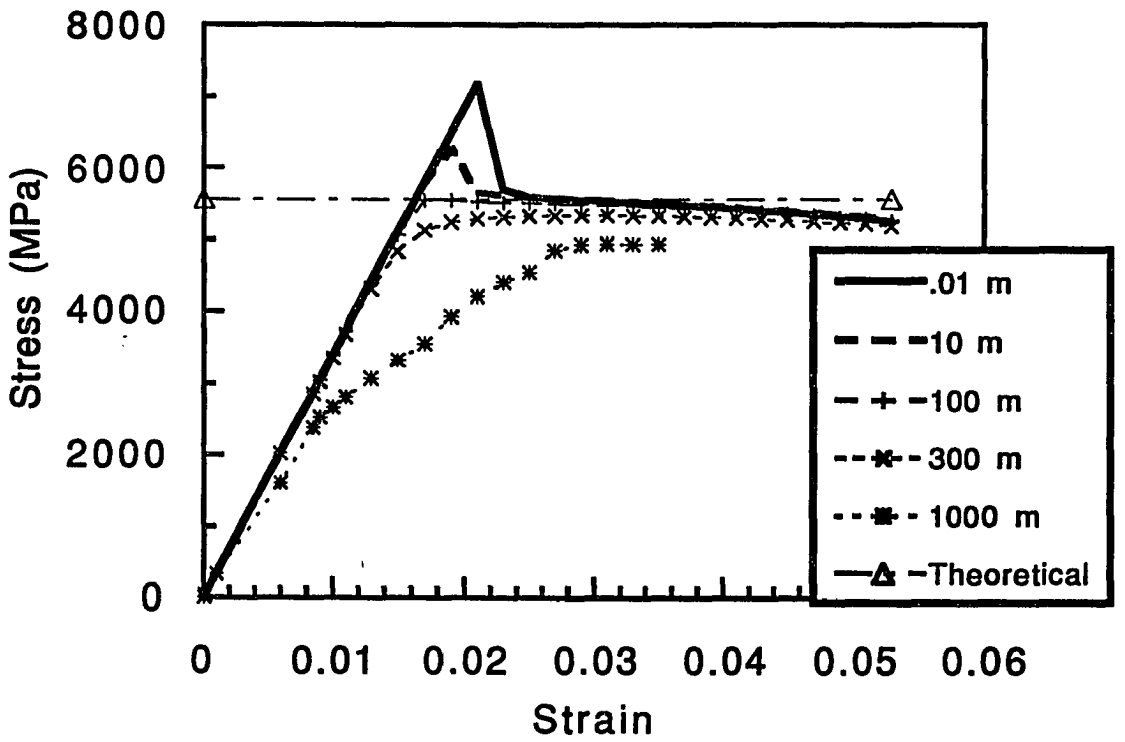

Figure 29: Stress-strain relationships for theoretical and numerical solutions with different initial amplitudes of deformation. The best agreement between the numerical and theoretical stress strain relationship occurs for a_0 = 100 m. The stress-strain curve for an a_0 = 100 m increases linearly up to the buckling stress, then flattens immediately, maintaining a constant stress as the strain increases before ultimately decreasing. The stress-strain relationships for models with an a_0 less than 100 m increase linearly, but then overshoot the theoretical buckling stress before becoming non-linear. As with the amplitude-strain relationship, the worst agreement between the numerical and theoretical stress-strain curves occurs for a_0 = 1000 m, where development of a non-linear stress-strain relationship is gradual and occurs before the theoretical buckling stress.

gradual and occurs before the theoretical buckling stress. Thus, for Model 1, the best agreement between the numerical and theoretical stress strain relationship occurs for a_O = 100 m.

We investigated the effect of the initial wavelength on the stress-strain relationship using Model 1 with the 10 km thick grid and a_O =100 m. The initial wavelength was varied from 50 km to 300 km (theoretical buckling wavelength = 200 km). An examination of the grid deformation indicates that all models show signs of a change in wavelength at the point of buckling, displaying a modified wavelength which approaches the theoretical buckling wavelength, regardless of initial wavelength. The change in wavelength after buckling is not easily observed if the input wavelength is close to the buckling wavelength due to the grid finiteness and the overall shortening of the grid as it is strained. The peak stress or a point of dramatic change in stress-strain response marks the point of buckling observed in the deformation plots. A plot of the peak stress as a function of wavelength (Figure 30) confirms that the minimum buckling stress occurs at the buckling wavelength. We also found that higher buckling stresses were required as the difference between the initial wavelength and the theoretical buckling wavelength increased.

As an additional test, we examined the dependence of the stress-strain relationship on a_O and the additional parameter, grid thickness. We held the element aspect ratio, Young's modulus, density and Poisson's ratio constant as in Model 1, while the thickness and length were modified. Thickness of the grid was varied from 1 km to 40 km, and the grid length was varied accordingly such that the ratio L/h and λ/L were held constant. For our grid, we found that the optimal relationship between initial amplitude and thickness is $a_O \sim 0.01h$. However, additional testing suggests this relationship is sensitive to the ratios L/h and λ/L and thus, is grid dependent.

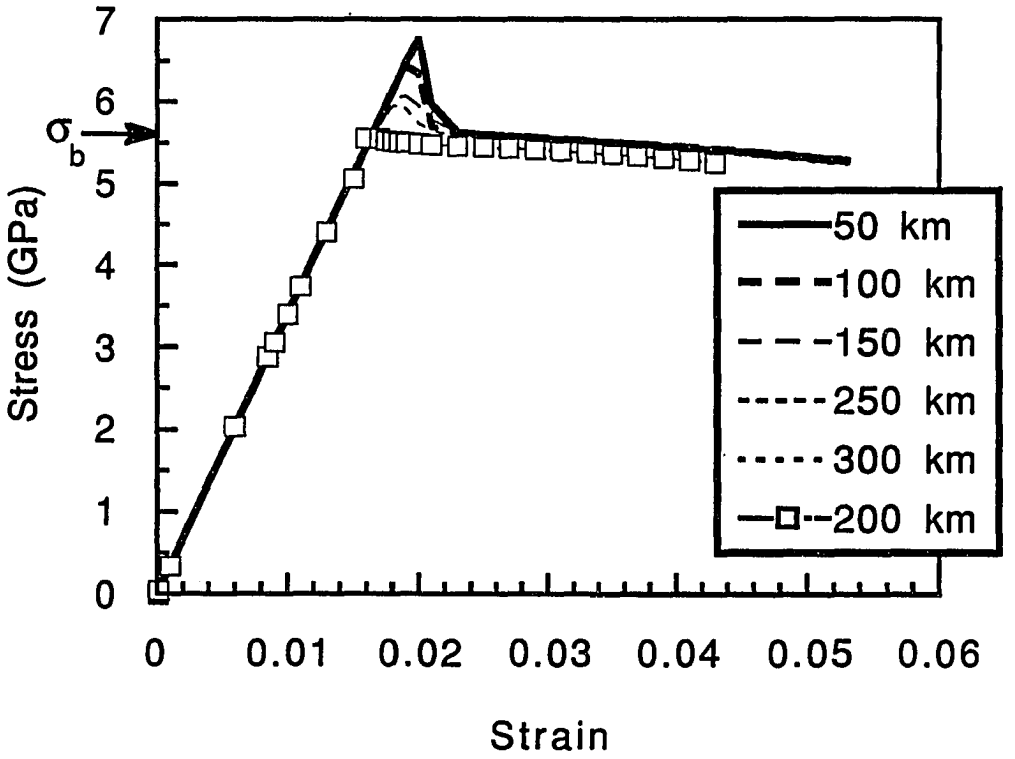

Figure 30: The effect of the initial wavelength on the stress-strain relationship using Model 1 with the 10 km thick grid with an a_0 =100 m. The peak stress or a point of dramatic change in stress-strain response marks the point of buckling observed in the deformation plots. The minimum buckling stress occurs for the model with an initial wavelength equal to the theoretical buckling wavelength of 200 km.

After extensive testing, we are confident that our finite element code reproduces the predictions of infinitesimal strain buckling to a reasonable degree of approximation. We compute an accurate buckling stress-strain relationship which also corresponds to an accurate amplification of the initial deformation. Although the effect of the initial deformation on the stress-strain and amplitude-strain relationships is grid dependent, by modifying the initial amplitude of deformation for a particular model, we are able to calculate accurate relationships. Thus, we have demonstrated that TECTON (v. 1.5) does reproduce the predictions of infinitesimal strain buckling to within a reasonable degree of approximation.

Buckling of a Faulted Plate

One of the goals in this study is to develop an understanding of how the presence of faults changes the buckling stress and wavelength in the lithosphere. Although faults vary in scale, their general behavior is scale independent [Walsh and Watterson, 1988; Walsh et al., 1991]. This suggests that the presence of several small faults can be as important as a single major fault in modifying the elastodynamics of the lithosphere. Thus, we have investigated the role of both fault spacing and fault depth.

Our principal model is a 32 km thick uniform elastic layer whose entire surface is cut by evenly spaced faults (Model 2, Table 3). Triangular elements extend over the depth of faulting (0-24 km) to allow for fault slip on dipping planes. An individual element is 4.76 km long and 4 km deep with an aspect ratio of 1:0.84 to accommodate a dip of 40°. We impose an initial sinusoidal deformation with a wavelength (equal to the buckling wavelength) of 300 km and an amplitude of 1400 m across the 1430 km long grid. The initial amplitude was chosen by insisting that the model predict the theoretical buckling stress at the theoretical buckling strain when the faults are locked and have minimal

overshoot of the buckling stress. The large increase in a_O, (relative to our test model), is due to thickening of the grid, degradation of the aspect ratio and the addition of triangular elements. All of these changes increase the calculated buckling stress and make choosing an optimal a_O more difficult because the change from a linear to non-linear stress-strain relationship is not as well defined.

Using the same boundary conditions as in the initial tests, we calculated the buckling stress for models with increasing fault depth. The faults extend across the entire grid with the exception of the nodes at the ends of the grid. Faults were initially one node long (cutting 12.5% of the plate thickness) then were increased by one node length until they were 6 nodes long (cutting 75% of the plate thickness). Spacing of the faults (4.76 km) is nearly equal to the depth of one element. The stress-strain relationship is linear at low strain for all fault depths, but becomes non-linear near the point of buckling (Figure 31). The exact point of buckling is more difficult to identify than in earlier tests because the change in slope is more gradual. To eliminate any ambiguity, we use the stress and wavelength at the theoretical buckling strain for a continuous plate as a reference for comparing changes in buckling stress and wavelength for the different models. The analysis indicates that buckling occurs at increasingly lower stress as the faults penetrate a greater percentage of the plate thickness. A fault cutting 75% of the plate thickness buckles at a stress more than 2.5 times lower than a similar plate with no faults. We will show later that the buckling stress is reduced by a factor of 4 for models in which the initial wavelength is equal to the buckling wavelength of the faulted plate. Beyond the point of buckling, we note a trend developing in which strain increases while the level of stress remains constant. This stress-strain curve superficially resembles a plastic rheology.

From the linear portion of the stress-strain curves, we calculate the effective Young's modulus as a function of the percent of the plate faulted (Figure 32). The change

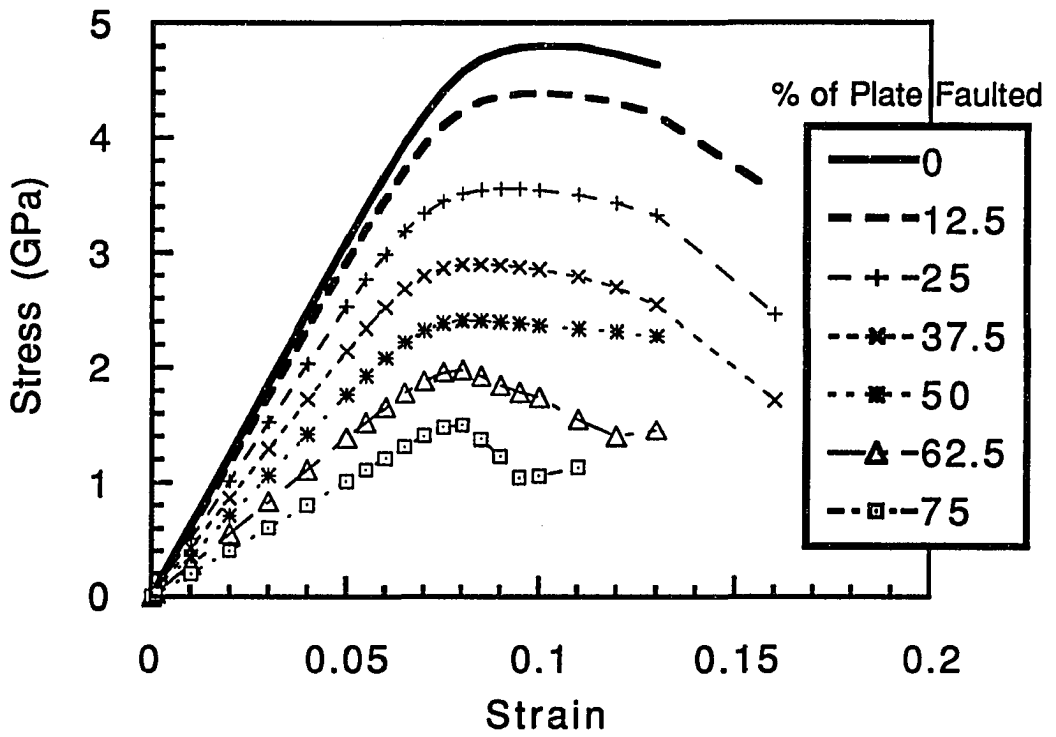

Figure 31: Stress-strain relationship for a plate cut by faults of increasing depth. Fault spacing is 4.76 km. The stress strain curve is linear at low strain for all fault depths, but becomes non-linear near the point of buckling. Buckling occurs at increasingly lower stress as the faults cut a greater percentage of the plate.

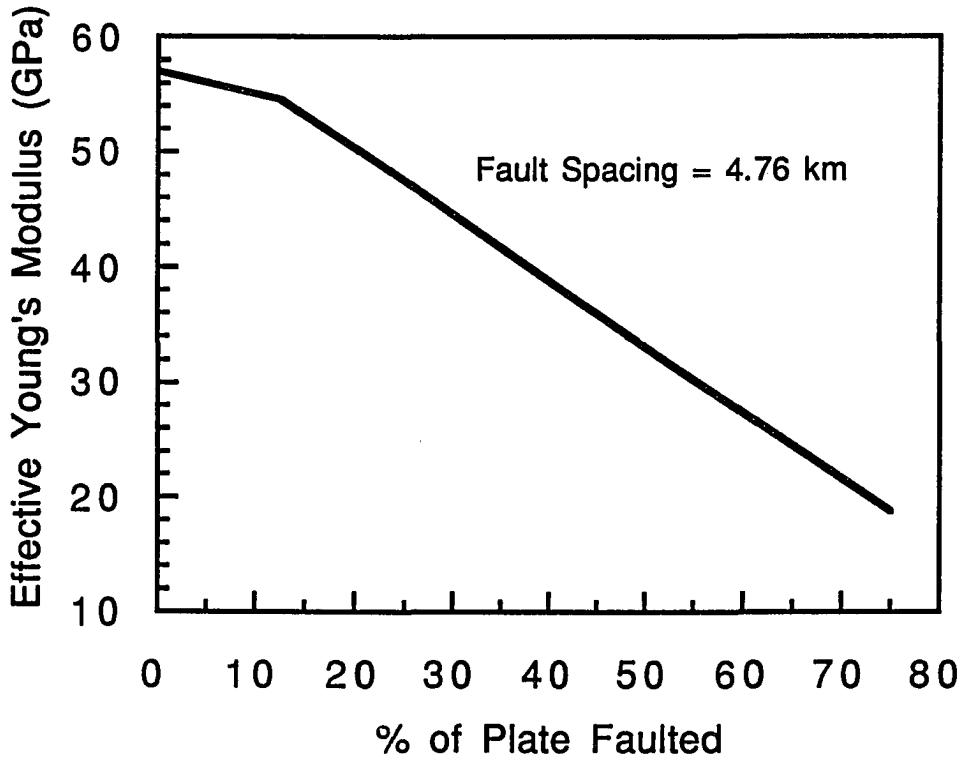

Figure 32: Effective Young's Modulus for a faulted plate. The fault spacing is 4.76 km. As the fault cuts a greater percentage of the plate, the effective Young's modulus decreases.

in the effective Young's modulus as the fault depth increases is nearly constant and suggests that the faults relieve essentially all of the stress over the depth of faulting. In this model, the depth of faulting is always nearly equal to or greater than the fault spacing which allows increased fault interaction and stress relief at all depths. A single node fault extending to 4 km depth causes a smaller change in the Young's modulus than for any other fault depth. The change in slope of the line may be an artifact of surface effects or it may indicate that a minimum depth of fault penetration is necessary to significantly modify the elastic properties of a thick elastic plate. Unfortunately, we are not able to differentiate these two possibilities.

A change in buckling wavelength is also observed as the fault depth increases (Figure 33). We compare the theoretical solution for buckling stress as a function of wavelength for a continuous plate to the faulted plate models and assume that the minimum buckling stress indicates the theoretical buckling wavelength for a faulted plate. The buckling wavelength decreases from an original length of 300 km to 262, 214 and 152 km as the percent of the plate faulted increases to 25, 50 and 75%, respectively. The arrows (Figure 33) indicate the minimum stress for each fault model. The accuracy of predicting the buckling wavelength is limited somewhat by the finiteness of the grid, the limited number of models, and the fact that the minimum in the buckling stress curve is broad. The minimum stress curve is broad because the faults force the plate to deform at a lower stress and wavelength than would be expected for a continuous plate. However, an increase in buckling stress for wavelengths increasingly far from the buckling wavelength is still observed.

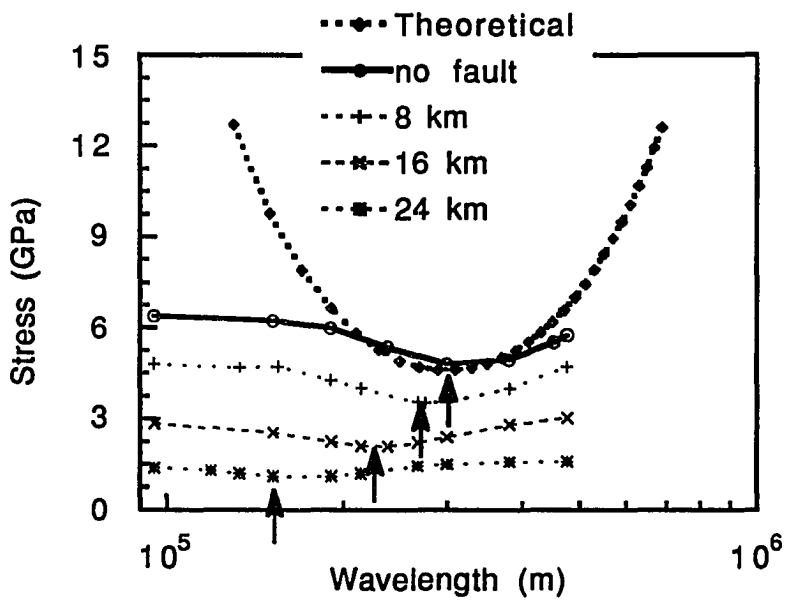

Figure 33: Change in buckling wavelength as fault depth increases. The buckling wavelength decreases from an initial 300 km for a continuous plate to 152 km for a plate with faults extending to 24 km depth (75% of the total thickness).

The Role of Fault Spacing

To determine the effect of fault spacing, we evaluated models at a suite of spacings across the grid and looked for changes in buckling stress and wavelength. From the analytical solution, we know that the buckling stress is proportional to the square root of the Young's modulus. Both buckling stress and wavelength demonstrate similar changes as the fault spacing increases (Figures 34 and 35). Careful scrutiny of the curves indicates that a slight curvature develops for the shorter faults as a result of the increased spacing and reduced interaction of the faults. Melosh and Williams [1989] demonstrated that the presence of a fault only relieves the stress over a distance roughly comparable to the fault depth. Thus, as the fault spacing increases, the faults must be longer to interact and fully relieve the stress over the faulted depth. For a spacing of one fault every ~9.5 km in our model, a fault extending to 16 km deep will create a stress field large enough to fully interact with the stress field of the adjacent faults. At a spacing of 38 km, the faults are never long enough to fully relieve the stress field between the closest faults. Thus, at larger spacings, the fault interaction is minimized and the deformation approaches that of an unfaulted plate.

The buckling stress-strain relationship shows a rapid approach to the unfaulted plate results for short faults penetrating less than 25% of the plate (Figure 34). A fault at a spacing of 4.76 km cutting 25% of the plate reduces the buckling stress by 27% while a similar fault at a spacing of 152 km results in only a minor reduction in the buckling stress. Similarly, the effective Young's modulus for a fault cutting 75% of the plate thickness is reduced by 60% for a fault spacing of 4.76 km but only 25% as the fault spacing reaches 152 km (Figure 35).

Deformation and changes in the stress-strain relationship are unique for the 152 km spacing model because the spacing is approximately one half the buckling wavelength (300

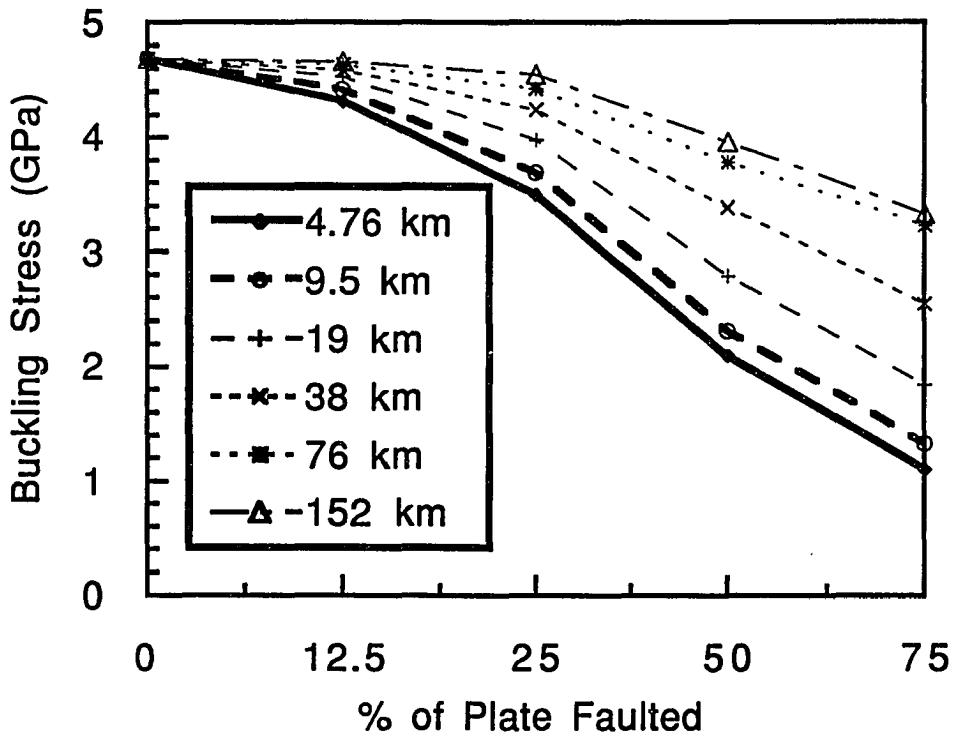

Figure 34: Change in buckling stress as a function of the percent of the plate thickness that is faulted. As the fault spacing increases and the percentage of the plate that is faulted decreases, the effect of the faults on the buckling stress decreases.

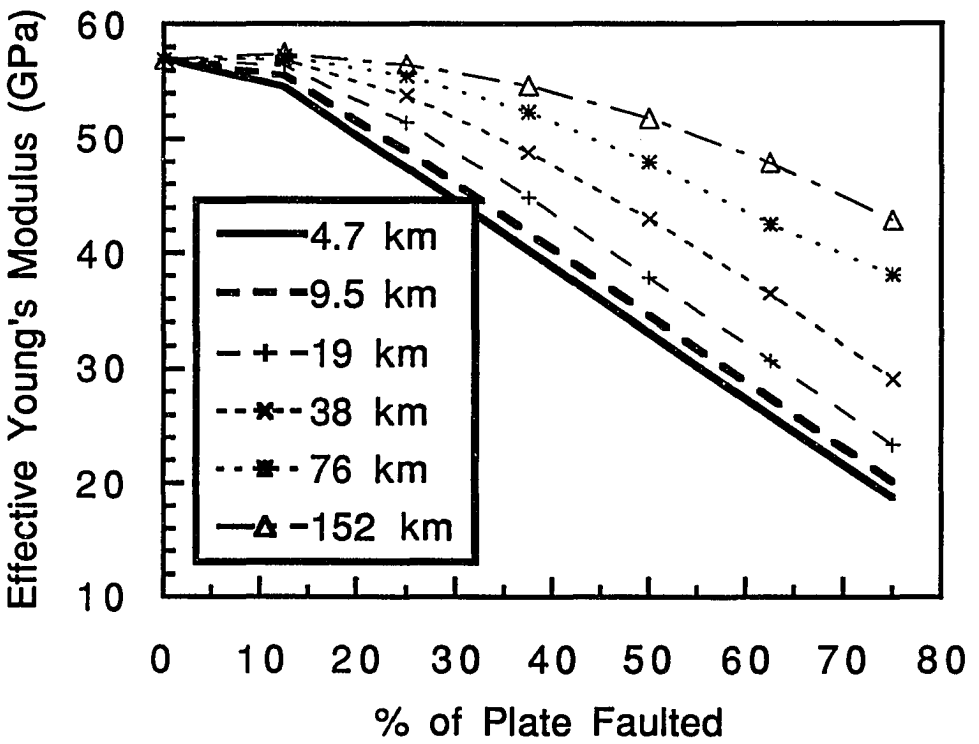

Figure 35: Change in effective Young's modulus as a function of a percentage of the plate that is faulted. As fault spacing increases, the effective Young's modulus increases.

km). As strain increases in the grid the regions between the faults begin to act as individual blocks hinged at the faults. As the hinge effect increases, the stress-strain relationship becomes non-linear at very low-strain. These changes are observed as a reduction in the buckling stress and effective Young's modulus for the fault cutting 75% of the plate. This behavior is not observed at other spacings and is simply due to the coincidence between fault spacing and buckling wavelength.

A more significant change is observed in the buckling wavelength as fault spacing increases (Figure 36). The greater spacing between faults results in a more rigid plate and longer buckling wavelength. Within the limitations of the grid, a smooth transition to longer wavelengths is observed as fault spacing increases. A model with a fault spacing of 4.76 km results in rather significant changes in buckling wavelength with increased fault depth; a 13, 29 and 66% reduction in buckling wavelength occurs for faults cutting 25, 50 and 75% of the plate thickness, respectively. But as the fault spacing increases to 152 km the change in buckling wavelength with fault depth is minimal for all but the fault cutting 75% of the plate thickness. In that case, the 24 km deep fault causes only a 9% reduction in buckling wavelength. Thus, faults at large spacing can still produce changes in effective Young's modulus and the buckling stress, but have a reduced influence on the buckling wavelength.

The Role of Fault Dip

As a final test, we varied the dip of the faults in Model 2. Of interest to us is whether the dip of the fault can alter the buckling stress or wavelength, i.e. is a plate cut by a low angle fault stronger than one cut by a high angle fault? Conceptually, one might imagine that a low-angle fault could transmit moment or stress across the break more efficiently, thus rendering it more continuous and less capable of buckling than a plate

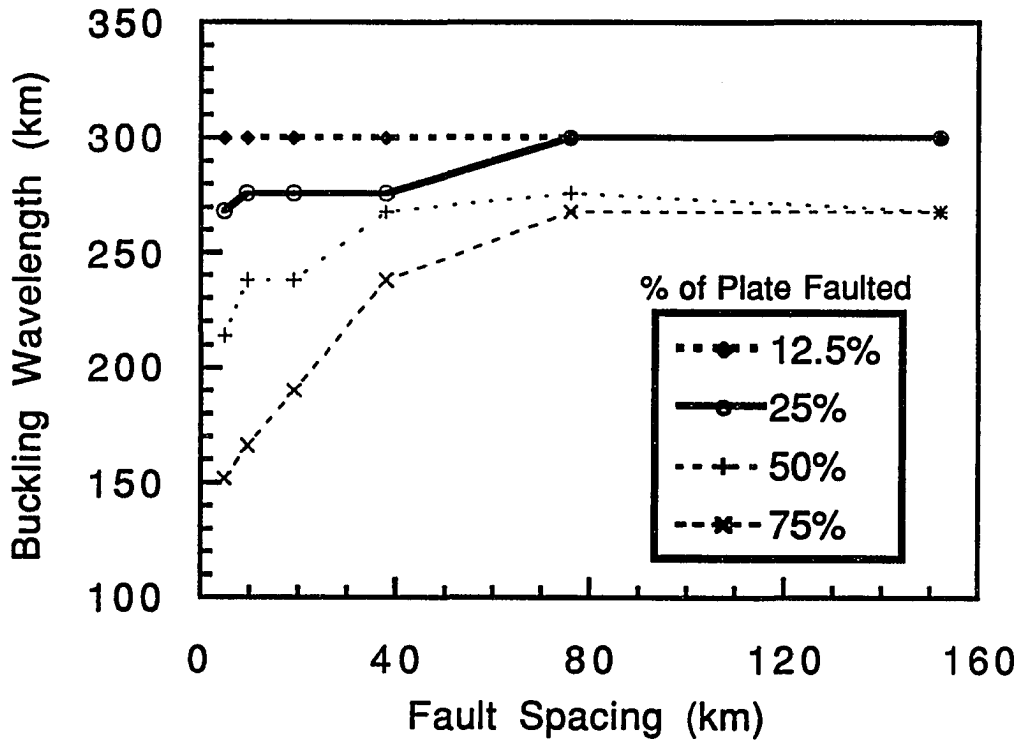

Figure 36: Change in buckling wavelength as a function of fault spacing. As the fault spacing increases and the percentage of the plate that is faulted decreases, the effect of the faults on the buckling wavelength also decreases. Within the limitations of the grid, a smooth transition to longer wavelengths is observed as fault spacing increases. The greater spacing between faults results in a more rigid plate and longer buckling wavelength.

broken into blocks by high angle faults. We evaluated fault dips of 25° and 60° with a fault spacing of 4.76 km in addition to the original model with a 40° dip to test this idea. To incorporate dip changes, we adjusted the length of the grid without changing the grid thickness. Regardless of fault dip, a fault of an equivalent number of nodes extends to the same depth in all models and only the fault length is changed. The change in dip results in a change in element aspect ratio, as well, but all other parameters in Model 2 remain the same. The grid with a fault dip of 25° is 2570 km long and has an aspect ratio of 1:0.466. For the 60° fault dip, the grid is 692 km long and has an aspect ratio of 1:1.732. The aspect ratio for both grids is considerably different than 1:1 and introduces some error into the solutions. To correct for this error, we found the optimal a_o to be 1600 m and 1800 m for the 25° and 60° dipping faults, respectively.

We examined the effect of fault dip on buckling stress and wavelength and found no significant differences for the three dip models (Figures 37 and 38). Only minor variations occur between the models as a result of grid finiteness. The change in the effective Young's modulus as a function of fault depth is shown for the three dip models in Figure 39. Again, there is no significant change in effective Young's modulus for the various fault dips. Thus, it appears that fault dip has little effect on the buckling response of a plate.

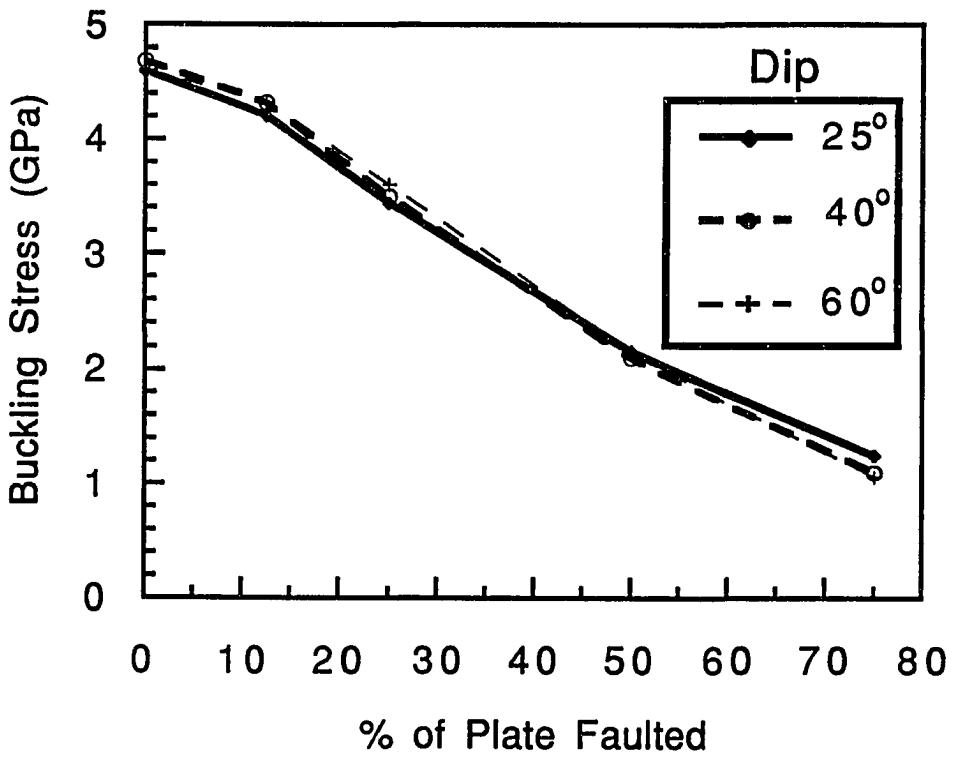

Figure 37: Buckling stress as a function of fault dip and percentage of the plate that is faulted. Fault dip has a minimal effect on the buckling stress as compared to the changes due to increased faulting of the plate.

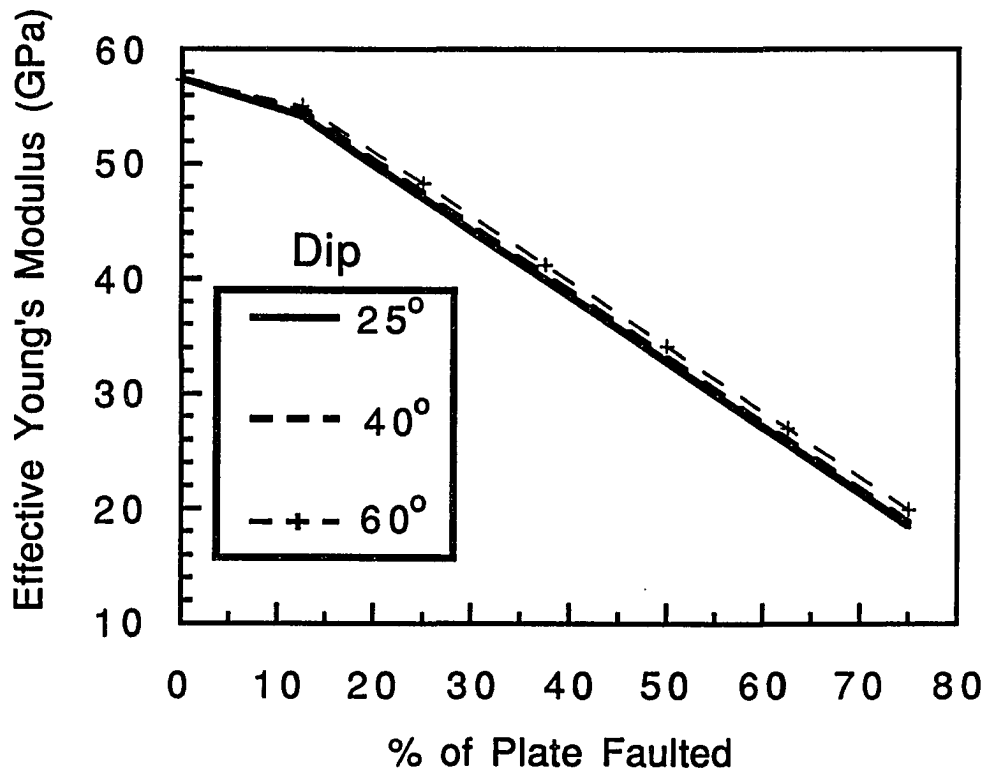

Figure 38: Effective Young's modulus as a function of fault dip and percentage of the plate that is faulted. Fault dip has a minimal effect on the effective Young's modulus as compared to the changes due to increased faulting of the plate.

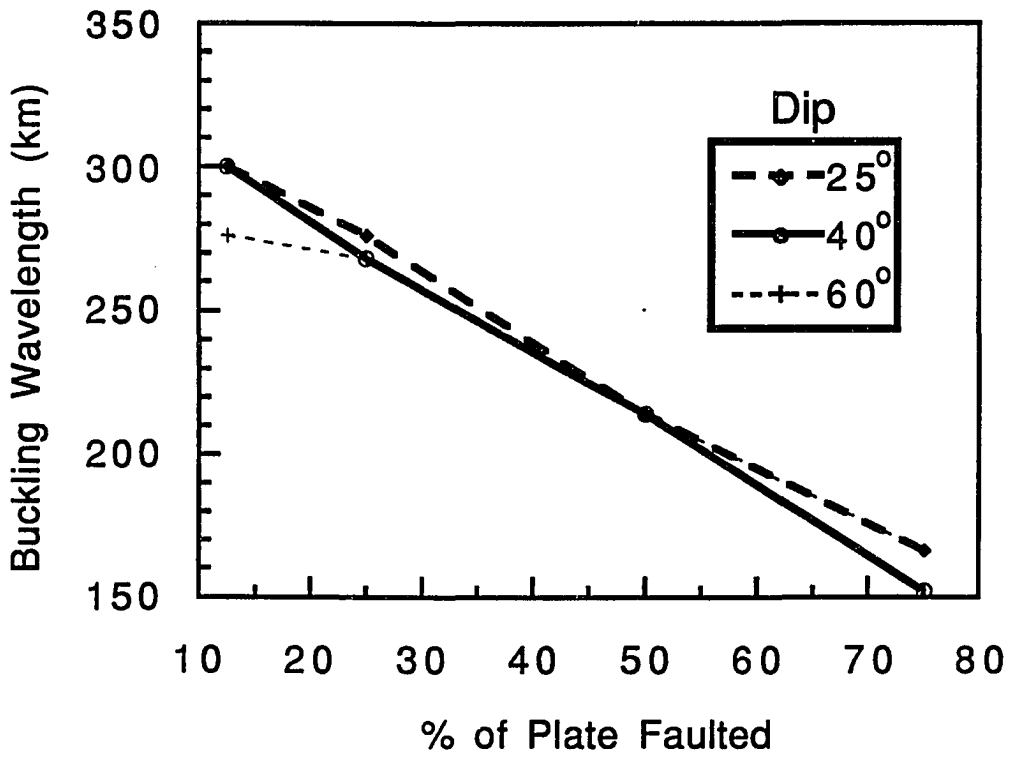

Figure 39: Buckling wavelength as a function of fault dip and percentage of the plate that is faulted. Fault dip has a minimal effect on the buckling wavelength as compared to the changes due to increased faulting of the plate.

DISCUSSION

It is interesting to see whether our results on faulted plates can be obtained from those for a continuous plate by means of simple approximations. For example, we might suppose that the portion of the faulted plate in which stress is relieved makes no contribution to buckling and the faulted plate can be approximated as a continuous plate of thickness equal to that of the unfaulted portion. We calculated the buckling stress for this case and compared that to our numerical results (Figure 40). The region of solutions predicted for the numerical models is highlighted and is bounded by the results for the fault models with spacings of 4.76 km and 152 km. The buckling stress predicted by the analytical solution falls within the region of solutions for the numerical models. For short, closely spaced faults (cutting less than 12.5% of the plate), a good correlation between the two methods occurs for buckling stress. As the faults cut a greater percentage of the plate, the buckling stress for the analytical solution approaches that of a less faulted plate with greater space between faults. For faults cutting 75% of the plate thickness, the buckling stress calculated with this approximate analytical model is 25-55% in error, depending on fault spacing.

The buckling wavelength for the approximate analytical solution was also compared to our numerical results. In this case, the buckling wavelength predicted by the analytical model is always shorter than that predicted by the numerical models (Figure 41). The error in the wavelength predicted by the analytical solution also increases as the percentage of the plate faulted increases. Thus, if the effect of a fault is approximated in an analytical solution for buckling by using an elastic thickness equal to the unfaulted thickness of the plate, the solution would greatly underestimate the buckling wavelength and could have errors as great as 55% in the buckling stress.

One might also approximate the effect of a fault by reducing the effective Young's modulus by a percentage equal to the percent of the plate thickness faulted. From equation (6) we can see that this has the same effect on the buckling stress as using an equivalent effective plate thickness because both E and h scale as a function of $\sqrt{\sigma_b}$. The buckling wavelength for an adjusted Young's modulus is different from that calculated with an adjusted elastic thickness. In Figure 41, the buckling wavelength calculated for this case falls between that calculated for the two numerical models with fault spacing at 4.76 and 152 km, respectively.

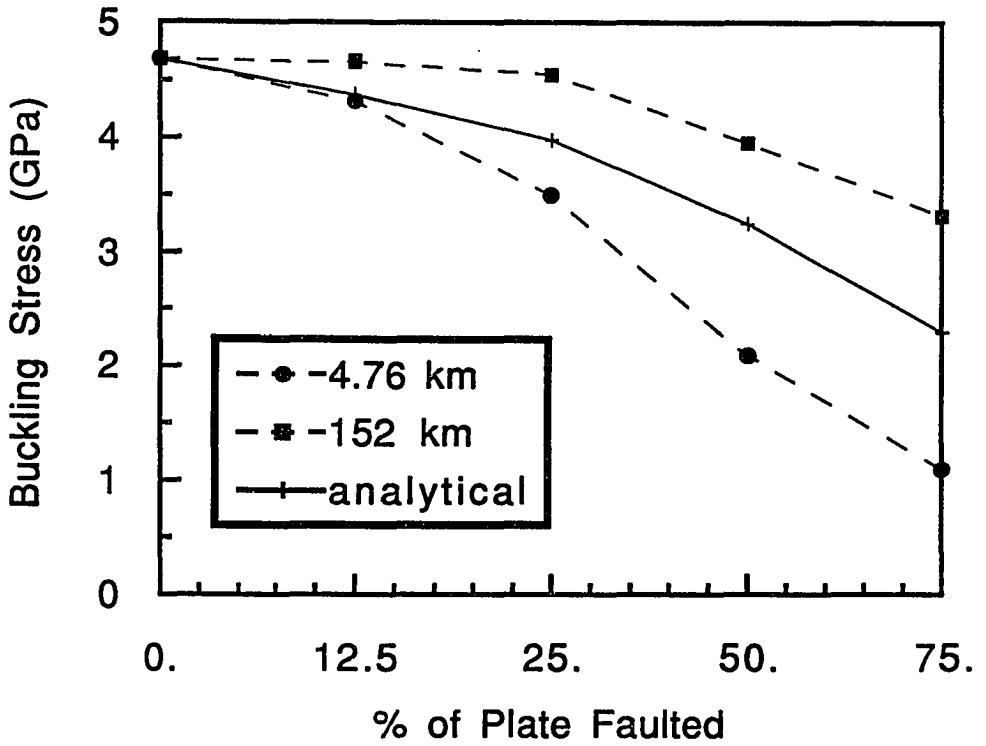

Figure 40: A comparison of two analytical approximations for the effect of faults on the buckling stress of a plate. Analytical solutions are calculated assuming that the effect of the faults can be approximated by using an effective thickness or Young's modulus reduced by the percentage of the plate that is faulted. Both of these assumptions result in the same analytical solution which predicts buckling stresses between the numerical results for the two extreme cases of faulting, spacing of 4.76 km and 152 km.

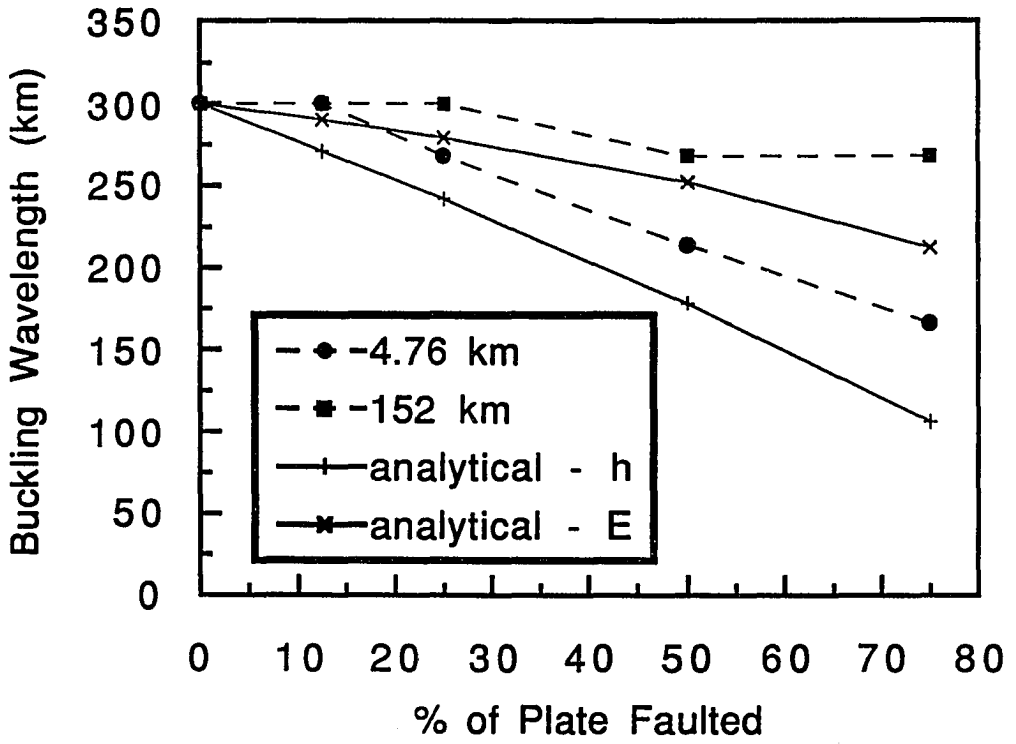

Figure 41: A comparison of two analytical approximations for the effect of faults on the buckling wavelength of a plate. Analytical solutions are calculated assuming that the effect of the faults can be approximated by using an effective thickness or Young's modulus reduced by the percentage of the plate that is faulted. Young's modulus and elastic thickness scale diffferently for buckling wavelength which results in two different analytical approximations. The analytical solution which uses an effective thickness predicts buckling wavelengths within the range of the numerical solutions while the analytical solution which uses an effective Young's modulus consistently predicts lower wavelengths than the numerical models.

CONCLUSIONS

We have demonstrated that the buckling response of a thick, faulted lithosphere is not equivalent to that of a thinner elastic plate. We found that faults lower the stress necessary for buckling, shorten the wavelength at buckling and result in a lower effective Young's modulus. Thus, a modification of only the elastic thickness or Young's modulus of a continuous plate does not accurately predict the buckling stress and wavelength. Buckling stress, wavelength and the effective Young's modulus are all dependent on fault depth as well as fault spacing. As fault depth increases, the buckling stress and wavelength decrease. For closely spaced faults that cut 75% of the plate thickness, the buckling wavelength is reduced by one-half and the buckling stress by 60% as compared to a continuous plate model. As fault spacing becomes very large, this reduction in buckling wavelength disappears. The decrease in buckling stress for the same model is slightly greater with up to a 60% reduction for closely spaced faults.

Analytical models which approximate the effect of the fault using the unfaulted thickness of the plate as the effective elastic thickness always underestimate the buckling wavelength and can have errors in the buckling stress of as much as 55%. Fault dip does not strongly affect either the effective Young's modulus or the buckling wavelength. Thus, the buckling response should be the same for a plate cut by a low angle fault or a high angle fault. Transmission of moment and shear stress across the fault is independent of dip.

CHAPTER 5

CONCLUSIONS

This dissertation is a collection of applications of the finite element method to complex tectonic problems. The nucleation and growth of faults is a fundamental, yet poorly understood, process at work in the Earth. In Chapter 2, I examined this problem for one tectonic environment, the stable craton. I assume there are no unusual thermal, mechanical or rheological anomalies at mid- or lower-crustal depths which could concentrate stress and provide a deep source of stress for earthquakes. For a model of a layered crust with increasing strength with depth, I found that the initiation and propagation of a planar fault from the base of the seismogenic zone to the surface requires greater strain and results in larger earthquakes than rupture downward, independent of dip angle or crustal model. Once a fault initiates at depth, rupture would always progress to the surface without the need for increased regional strain.

However, initiation of a fault at the surface and growth downward requires less total strain and can occur in a stable manner. To develop a fault which extends from the surface completely through the seismic zone would require increasing the level of strain at various stages of fault growth depending on fault dip and crustal model. For an appropriate shear fracture energy, fault growth occurs in stages, developing at shallow depths through small earthquakes with little displacement. The moment and average displacement calculated for all fault models have two dominant characteristics: (1) the average displacement and moment are small until the fault has cut at least half of the seismic zone and (2) large increases in the average displacement and moment occur once the fault has cut the entire seismogenic zone. I suggest that initial development of faults in a stable

cratonic region is a result of nucleation at the surface and rupture downward. Re-rupturing of an established fault may initiate at the surface or at depth depending on the degree of fault healing between events and the tectonic stress available.

These results are at odds with the seismic record in which 90% of all crustal earthquakes initiate at depth and rupture to the surface. The discrepancy can be addressed in two ways: (1) well developed faults behave differently than new young faults and most earthquakes are occurring on well established faults [Scholz et al., 1986; Marone and Scholz, 1988], and/or (2) the size of the earthquakes on new faults are generally small enough to go undetected or be ignored. No matter how one explains the discrepancy, true fault behavior remains an unknown. To complicate the picture, a whole new group of earthquakes were identified in the last decade, blind thrusts. Several blind thrust events occurred in California, the 1983 Coalinga and the 1987 Whittier Narrows. They are large events that initiated at depth and ruptured upward - but not all the way to the surface. Both occurred in active tectonic areas, nucleating on deep decollement surfaces which act to concentrate stress at depth. Both propagated through thick sedimentary sequences and stopped. The Coalinga event probably stopped due to interaction with a conjugate fault [Eberhardt-Phillips, 1990]. Nevertheless, the mechanics of blind thrusts is a problem which remains to be solved.

In Chapter 3, I analyzed the rupture history of one of the most over-published but still not understood earthquakes in history (over 90 abstracts were published within 2 months of the rupture and 200+ papers in the first year!), the Loma Prieta earthquake. This is also an enigma for the results presented in Chapter 2. The fault ruptured in an oblique, right lateral strike slip-high-angle reverse motion from 18 km depth to 8-5 km depth in a M_S =7.1 event. The primary factor controlling the depth of rupture on the Loma Prieta Fault is low stress in the upper crust. The low stress condition can be modeled by either choosing

the material properties such that a large contrast in Young's modulus exists between the two layers of the crust, or by including numerous slipping faults in the upper crust.

The region of the Loma Prieta event is complicated by a bend in the San Andreas which may be causing detachment of the lower crust from the mantle and uplift of the Santa Cruz Mountains [Furlong and Langston, 1990; Anderson, 1990]. Certainly the region is cut by numerous faults of variable orientation. Thus, the simple models presented here only begin to look at the stress state near the Loma Prieta Fault. The beauty of finite element modeling is that more complex models can be analyzed with additional faults and time dependent rheologies. The Loma Prieta rupture must be understood to reevaluate the seismic hazard potential of the San Andreas. The results of the rupture analysis support a model in which the strength of the San Andreas Fault is equal to or less than the strength of the Loma Prieta Fault. An evaluation of the stress at the intersection of the two faults indicates that the Loma Prieta Fault in the upper crust is still closest to the point of failure than the San Andreas Fault over the same depth. Thus, rupture of the Loma Prieta did not significantly increase the seismic hazard of the San Andreas in that region.

In Chapter 4, I investigated the role of faults in the buckling of an elastic plate. Traditional analyses of the deformation of lithospheric plates have relied heavily on the elastodynamics of continuous, isotropic elastic materials. However, experience shows that lithospheric plates are cut by many faults on many scales, and the applicability of solutions for continuous materials is questionable. I studied the effect of changes in fault depth, spacing and dip on the buckling stress, wavelength and effective Young's modulus.

In our models, we found that as the fault depth increases both the buckling stress and wavelength decrease. Similarly, the effective Young's modulus is a decreasing function of fault depth. As fault spacing was varied from 4.76 km to 152 km, the effect of the faults on the buckling stress and wavelength was minimized. Fault dip appears to have

no significant effect on buckling response. Thus, the buckling response should be the same for a plate partially cut by a high angle fault or a low angle fault, as transmission of moment across the fault is independent of dip.

The buckling response of a thick, faulted lithosphere is not equivalent to that of a thinner elastic plate. Faults lower the stress necessary for buckling, shorten the wavelength at buckling and result in a lower effective Young's modulus. Thus, a modification of only the elastic thickness or Young's modulus of a continuous plate does not accurately predict the buckling stress and wavelength.

The buckling analysis addresses a basic need for understanding of one of the major hurdles in crustal deformation problems, the role of faults in weakening the lithosphere. The other basic requirements we must satisfy for better flexural models are a better understanding of regional and temporal variations in the rheology of the lithosphere and the dynamics of the asthenosphere. With the results in Chapter 4, the next most obvious problem is to investigate both the role of varied rheologies and faults on deformation of the lithosphere.

REFERENCES CITED

Anderson, E. M., (1951), The dynamics of faulting and dyke formation with applications to Britain, Oliver and Boyd, Edinburgh, pp. 206.

Anderson, R.S., (1990), Evolution of the Santa Cruz Mountains by advection of crust past a restraining bend on the San Andreas Fault, *Science*, 249, 397-401.

Angevine, C.L., and K.M. Flanagan, (1987), Buoyant subsurface loading of the lithosphere in the Great Plains foreland basin, *Nature*, 327, 137-139.

Atwater, T., (1970), Implications of plate tectonics for the Cenozoic tectonic evolution of the western North America, in Plate tectonics and geomagnetic reversals, ed. A. Cox, Freeman Press.

Brace, W.R., and W. Kohlstedt,.(1980), Limits on lithospheric stress imposed by laboratory experiments, *J. Geophys. Res.*, 85, 6248-6252.

Berg, R., (1962), Mountain flank thrusting in Rocky Mountain foreland, Wyoming and Colorado, *Am. Assoc. Pet. Geol. Bull.*, 46, 2019-2032.

Beroza, G.C. (1991), Near source modeling of the Loma Prieta earthquake: evidence for heterogeneous slip and implications for earthquake hazard, *Bull. Seis. Soc. Am.*, 81, 1603-1621.

Boyer, S. E., and D. Elliot, (1982), Thrust systems, *Bull. Am. Ass. Petrol. Geol.*, 66, 1196-1230.

Buck, W.R., (1988), Flexural rotation of normal faults, *Tectonics*, 5, 959-974.

Butler, R.F., G.E. Gehrels, W.C. McClelland, S.R. May, and D. Klepacki, (1989), Discordant paleomagnetic poles from the Canadian Coast Plutonic Complex: Regional tilt rather than large-scale displacement?, Geology, 17, 691-694.

Byerlee, J.D., (1978), Friction of rocks, *Pure Appl. Geophys.*, 116, 615-626.

Chapple, W. M., and Forsythe, D. W., (1979), Earthquakes and bending of plates at trenches, *J. Geophys. Res.*, 84, 6729-6749.

Chase, C.G. and T.C. Wallace (1986), Uplift of the Sierra Nevada of California, *Geology*, 14, 730-733.

Chen, W.P., and P. Molnar, (1983), Focal depths of intracontinental and intraplate earthquakes and their implications for the thermal and mechanical properties of the lithosphere, *J. Geophys. Res.*, 88, 4183- 4214.

Cloeting, S., M.H. McQueen and K. Lambeck, (1985), On a tectonic mechanism for regional sea level variations, *Earth Planet. Sci Lett.*, 75, 157-166.

Comer, R., (1983), Thick plate flexure, *Geophys. J.R. Astron.Soc.*, 72, 101-113.

Coney, P.J., (1969), Gravitational tensional faulting and tectonic denudation: *Am. Assoc. Petr. Geol. Bull.*, 52, 433-435.

Cox, S.J.D., and C.H. Scholz, (1988), Rupture initiation in shear fracture of rocks, *J. Geophys. Res.*, 93, 3307-3320.

Cox, S.J.D, and C.H. Scholz, (1988), On the formation and growth of faults: an experimental study, *J. Struct. Geol.*, 10, 413-430.

Coulomb, C.A., (1773), Sur une application des regles de maximis et minimus a quelques problems de statique relatifs al Architecture, *Acad. Roy. des Sciences Memoires de math et de physique par ivers savans*, 7, 343-382.

Das, S., and C. H. Scholz, (1983), Why large earthquakes do not nucleate at shallow depths, *Nature*, 305, 621-623.

Desai, C., (1979), Elementary Finite Element Method, Prentice-Hall Inc., 434 pp.

Eberhart-Phillips, D., (1989), Active Faulting of the Coalinga Anticline as interpreted from three dimensional velocity structure and seismicity, *J. Geophys. Res.*, 94, 15565-15586.

Furlong, K.P., W.D. Hugo, and G. Zandt, (1989), Geometry and evolution of the San Andreas Fault Zone in Northern California, *J. Geophys. Res.*, 94, 3100-3110.

Gordon, F.R., and J.D. Lewis, (1980), The Meckering and Calingiri earthquakes October 1968 and Marech 1970, *Bull. Geol.Surv. West. Aust.*, 126, 229 pp.

Hall, M.K., and C.G. Chase, (1989), Uplift, unbuckling and collapse: Flexural history and isostasy of the Wind River Range and Granite Mountains, Wyoming, *J. Geophys. Res.*, 94, 17581-17594.

Hanks, T.C., (1971), The Kuril Trench Hokkaido rise system: large shallow earthquakes and simple models of deformation, *Geophys. J. R. Astro. Soc.*, 23, 173-189.

Hetenyi, M., (1946), Beams on elastic foundation, University of Michigan Press, pp. 204.

Hill, M. L., and J.W. Dibblee, Jr., (1953), San Andreas, Garlock, and the Big Pine Faults, California - a study of the character, history, and tectonic significance of their displacements: *Geol. Soc. Am. Bull.*, 64, 443-458.

Hubbert, M.K., and W.W. Rubey, (1959), Role of fluid pressure in mechanics of overthrust faulting: I mechanics of fluid-filled porous solids and its applications to overthrust faulting, *Geol. Soc. Am. Bull.*, 70, 115-166.

Jordan, T.E., (1981), Thrust loads and foreland basin evolution, Cretaceous Western United States, *Am. Assoc. Petr. Geol.*, 65, 2506-2521.

Kanamori, H., (1980), The state of stress in the Earth's lithosphere, in Physics of the Earth's Interior, edited by A. Dziewonski and E. Boshi, Amsterdam, North-Holland, 531-554.

Lambeck, K., (1983), The role of compressive forces in cratonic basin formation and mid-plate orogenesis, *Geophys. Res. Lett.*, 10, 848-849.

Langston, C.A., (1987), Depth of Faulting during the 1968 Meckering, Australia, Earthquake sequence determined from waveform analysis of local seismograms, *J. Geophys. Res.*, 92, 11561-11574.

Lawn, B.R. and T.R. Wilshaw, (1975), Fracture of Brittle Solids, Cambridge Univ. Press, pp.203.

Li, V, (1987), Mechanics of Shear rupture applied to earthquake zones, in Fracture Mechanics of Rock, ed., B. Atkinson, Academic Press, 351-428.

Li, V. and J.R. Rice, (1983), Preseismic rupture progression and great earthquake instabilities at plate boundaries, *J. Geophys. Res.*, 88, 4231-4246.

Li, V. and J.R. Rice, (1987), Crustal deformation in great California earthquake cycles, *J. Geophys. Res.*, 92, 11533-11551.

Marone, C. and C.H. Scholz, (1988), The depth of seismic faulting and the upper transition from stable to unstable slip regimes, *Geophys. Res. Lett.*, 15, 621-624.

Marshall, G.A., R.S. Stein, and W. Thatcher, (1991), Faulting geometry and slip from co-seismic elevation changes: the 18 October 1989, Loma Prieta, California earthquake, *Bull. Seis. Soc. Am.*, 81, 1660-1683.

McGarr, A. , (1988), On the state of lithospheric stress in the absence of applied tectonic forces, *J. Geophys. Res.*, 93, 13609-13617,.

McGarr, A., S.M. Spottiswoode, N.C. Gay, and W.D. Ortlepp, (1979), Observations relevant to seismic driving stress, stress drop, and efficiency, *J. Geophys. Res.*, 84, 2251-2261.

McNutt, M. and H.W. Menard, (1982), Constraints on yield strength in the oceanic lithosphere derived from observations of flexure, *Geophys. J. R. Astron. Soc.*, 71, 363-394.

Meissner, R. and J. Strehlau, (1982) Limits of stresses in continental crusts and their relation to the depth- frequency distribution of shallow earthquakes, *Tectonics*, 1, 73-89.

Melin, S., (1986), When does a crack grow under mode II conditions?, *Intern. J. Frac.*, 30, 103-114.

Melosh, H.J., (1978), Dynamic support of the outer rise, *Geophys. Res. Lett.*, 5, 321-324.

Melosh, H.J. and C A. Williams, (1989), Mechanics of graben formation in crustal rocks: a finite element analysis, *J.Geophys. Res.*, 94, 13961-13973.

Miller, C.K., and K.P. Furlong, (1988), Thermal-mechanical controls on seismicity depth distributions in the San Andreas Fault zone, *Geophys. Res. Lett.*, 15, 1429-1432.

Mohr, O., (1909), Welche Um Stande bedigen die Elastizitatsgrenze und den Bruch eines Materials?, *Z. Ver. dt. Ing.*, 44, 1524-1530; 1572-1577.

Mooney, W.D., and A. W.Walter, (1982), Crustal structure of the Diablo and Gabilan Ranges, Central California: A reinterpretation of existing data, *Bull. Seis. Soc. Am.*, 72, 1567.

Paris, P.C., and G.C. Sih, (1965), ASTM STP 381.

Petit, Jean-Pierre and M. Barquins, (1988), Can natural faults propagate under mode II conditions?, *Tectonics*, 7, 1243-1256.

Reches, Z., (1990), Self-organized cracking - a mechanism for brittle faulting, abstr., *EOS Trans. Am. Geophys. Union*, 71, p. 1586.

Rooke, D.P., and D.J. Cartwright, (1976), Compendium of stress intensity factors, HMSO.

Sandwell, D.T., and D.C. McAdoo, (1985), Folding of oceanic lithosphere, *J. Geophys. Res.*, 90, 8563-8569.

Scholz, C.H., C.A. Aviles, and S. G. Wesnousky, (1986), Scaling differences between large interplate and intraplate earthquakes, *Bull. Seis. Soc. Am.*, 76, 65-70.

Schwartz, S.Y., D.L. Orange, R.S. Anderson, (1990), Complex fault interactions in a restraining bend on the San Andreas Fault, Southern Santa Cruz Mountains, California, *Geophys. Res. Lett.*, 17, 1207-1210.

Segall, P. and D.D. Pollard, (1983), Nucleation and growth of strike slip faults in granite, *J. Geophys. Res.*, 88, 555-568.

Sibson, R.H., (1982), Fault zone models, heat flow, and the depth distribution of earthquakes in the continental crust of the United States, *Bull. Seis. Soc. Am.*, 72, 151-163.

Sibson, R.H., (1984), Roughness at the base of the seismogenic zone: contributing factors, *J. Geophys. Res.*, 89, 5791-5799.

Sibson, R.H., (1985), A note on fault reactivation, *J. Struc. Geol.*, 7, 751-754.

Smoluchowski, M., (1909a), Uber ein gewisses stabilitatsproblem der elastizitatslehre und dessen beziehung zur entstehung von faltengebirgen. *Bull. Int. Acad. Sci. de Cracovie*, 3-20.

Smoluchowski, M., (1909b), Versuche uber faltungserscheinungen schwimmender elasticher platten, *Bull. Int. Acad. Sci. de Cracovie*, 727-734.

Smoluchowski, M., (1909c), Kilka Uwag o Fizyczuych podstawach teoryi gorotworczych, *Kosmos*, 34, 547-579.

Sneddon, I.N., and N. Lowengrub, (1969), Crack Problems in the classical theory of elasticity, Wiley and Sons.

Steidl, J.H., R. J. Archuleta, and S. Hartzell, (1991), Rupture history of the 1989 Loma Prieta, California, earthquake, *Bull. Seis. Soc. Am.*, 81, 1573-1602.

Stein, R.S., and R.S. Yeats, (1989), Hidden Earthquakes, *Scientific Am.*, 260, 48-59.

Stuart, W.D., and G.M. Mavko, (1979), Earthquake instability on a strike-slip fault, *J. Geophys. Res.*, 84, 2153-2160.

Tada, H., P.C. Paris, and G.C. Irwin, (1973), Stress analysis of cracks handbook, Del.

Tse, S.T., and J.R. Rice, (1986), Crustal earthquake instability in relation to the depth variation of frictional slip properties, *J. Geophys. Res.*, 91, 9452-9472.

Turcotte, D., and G. Schubert, (1982), Geodynamics: Applications of continuum physics to geological problems, John Wiley and Sons, 450 pp.

Vening Meinesz, (1950), Les graben africains, resultat de compression ou de tension dan la croute terrestre?, *Inst. R. Colon. Belge Bull. Seances*, 2,539-552.

Vogfjord, K.S., and C. A. Langston, (1987), The Meckering earthquake of October 14, 1968: A possible downward propagating rupture, *Bull Seism. Soc. Am.*, 77, 1558-1578.

Walcott, R., (1970), Flexure of the lithosphere at Hawaii, *Tectonophys.*, 9, 435-446.

Wald, D.J., D.V. Helmberger, and T.H. Heaton (1991), Rupture model of the 1989 Loma Prieta earthquake from the inversion of strong motion and broad band teleseismic data, *Bulll. Seis. Soc. Am.*, 81, 1540-1572.

Wallace, M.H. and J. Kemeny, (1990), Nucleation and Propagation of Crustal Scale Faults, abstr. *EOS, Trans. Am. Geophys. Union*, 71, p. 1635.

Wallace, M.H. and T.C. Wallace, (1991), The paradox of the October 19, 1989 Loma Prieta earthquake: Why did rupture stop at 8 km depth?, abstr., EOS Trans. Am. Geophys. Union., 72, p.310.

Wallace, M.K., C.A. Williams, C.G. Chase, and H.J. Melosh, (1990), Initiation and propagation of crustal scale thrust faults: A finite element analysis, abstr., *Geol. Soc. Am. Cordilleran Section Meeting*, p. 91.

Wallace, T.C., A. Velasco, J. Zhang, and T. Lay (1991), A broadband seismological investigation of the 1989 Loma Prieta, California, earthquake: Evidence for deep slow slip?, *Bull. Seis. Soc. Am.*, 81, 1622-1646.

Walsh, J., and J. Watterson, (1988), Analysis of the relationship between displacements and dimension of faults, *J. Struct. Geol.*, 10, 239-247.

Walsh, J., J. Watterson, and G. Yielding, (1991), The importance of small scale faulting in regional extension, *Nature*, 351, 391-393.

Williams, C.A., (1990), Numerical modeling of fault formation and the dynamics of existing faults, Ph.D Dissertation, University of Arizona.

Winkler, E., (1867), Die Lehre von der Elastizitat und Festigkeit, Prag, p. 182.

Wong, T.-F., (1982), On the normal stress dependence of the shear fracture energy, in Earthquake source mechanics, Geophysical Monograph 37, Am. Geophys. Union, Washington D.C.

Working Group on California Earthquake Probabilities (1988), Probabilities of large earthquakes occurring in California on the San Andreas Fault, *U.S. Geol. Surv. Open-File Report 88-398*, 62 pp.

Working Group on California Earthquake Probabilities (1990), Probabilities of large earthquakes in the San Francisco Bay Region, California, *U.S. Geol. Surv. Circ. 1053*, 51 pp.

Zandt, G. and T. Owens, (1980), Crustal flexure associated with normal faulting and implications for seismicity along the Wasatch Front, Utah, *Bull. Seis. Soc. Am.*, 70, 1501-1520.

Zoback, M.D., M.L. Zoback, V.S. Mount, J. Suppe, J.P. Eaton, J.H. Healy, D. Oppenheimer, P. Reasenberg, L. Jones, C.B. Rayleigh, I.G. Wong, O. Scotti, and

W. Wentworth, (1987), New evidence on the state of stress of the San Andreas fault system, *Science*, 238, 1105-1111.